PERGAMON

Progress in Particle and Nuclear Physics 51 (2003) 223–307

Progress in Particle and Nuclear Physics

http://www.elsevier.com/locate/npe

Gaussian Expansion Method for Few-Body Systems

E. HIYAMA[1], Y. KINO[2] and M. KAMIMURA[3]

[1]*High Energy Accelerator Research Organization (KEK), Tsukuba 308-0801, Japan*
[2]*Department of Chemistry, Tohoku University, Sendai 980-8578, Japan*
[3]*Department of Physics, Kyushu University, Fukuoka 812-8581, Japan*

April 8, 2003

Abstract

We review our method of calculation, Gaussian Expansion Method (GEM), for bound and scattering states of few-body systems. The method was proposed in 1988 and has been applied to a variety of few-body systems. The understanding on the structure and the mechanisms of reactions of those systems obtained from such applications is discussed together with some useful techniques for the calculations. A well-chosen set of Gaussian basis functions forms an approximate complete set in a finite coordinate space so that it can describe accurately short-range correlations and long-range asymptotic behavior as well as highly oscillatory character of wave functions in the bound and the scattering states of the systems. Examples of applications of GEM include i) the latest determination of antiproton mass by the analysis of laser spectroscopic data for antiprotonic helium atoms, ii) predictions and experimental verifications on the structure of hypernuclei and hyperon-nucleon interactions, iii) Coulomb three-body calculations of bound and resonant states of muonic molecules as well as muon transfer reactions in muon catalyzed fusion cycles, iv) a new treatment of CDCC (continuum-discretized coupled channels) method for three- and four-body breakup processes, and v) benchmark test calculations for three- and four-nucleon bound states using realistic interactions.

0146-6410/03/$ - see front matter
doi: 10.1016/S0146-6410(03)00082-6

Table of Contents

1 Introduction

There are many examples of *precision* numerical calculations which have contributed to examining fundamental laws of physics and interactions in physical systems. One recent example is the determination of the upper limit of the difference between the masses of proton and antiproton, m_p and $m_{\bar{p}}$, respectively. The first recommended upper limit of $|m_{\bar{p}} - m_p|/m_p$ by the Particle Data Group listed in Particle Listings 2000 [1] was 5×10^{-7}, which could be used for a test of CPT invariance. This number was extracted from a high-resolution laser experiment involving metastable states of antiprotonic helium atom $(\mathrm{He}^{2+} + e^- + \bar{p})$ [2] by Kino *et al.* [3] through a theoretical analysis of the Coulomb three-body system using Gaussian Expansion Method (GEM) of calculation developed for few-body systems [4, 5, 6, 7] which is the present article. The ratio was improved to $|m_{\bar{p}} - m_p|/m_p < 6 \times 10^{-8}$, as listed in the Particle Listings 2002 [8], by a later, more extensive experiment [9] and an additional calculation [10].

Many important problems in physics can be addressed by solving the Schrödinger equation with high precision for three- and four-body systems.. It is therefore of particular importance to develop methods for precision calculations for such problems. In the calculation of the three-body system mentioned above, the interaction (the Coulomb potential) is precisely known. In newly developing fields of physics, however, there are cases in which interactions are not well known. Studies of such subjects with precision (few-body) calculations are also meaningful and important. In order to extract reliable new information and constrain the ambiguity in the interaction being examined, the calculation must be sufficiently rigorous.

Examples are seen in the study of hyperon(Y)-nucleon(N) and hyperon(Y)-hyperon(Y) interactions in hypernuclear physics. The YN and YY interactions proposed so far exhibit a great deal of ambiguity, since YN scattering experiments are extremely limited, and there are no YY scattering data. One can, however, obtain useful information on the YN and YY interactions from hypernuclear structure studies by combining theory and experiment in the following way: (1) There are candidate YN and YY interactions based on the OBE model and those based on constituent quark model. (2) There are experimental data of γ-ray spectroscopy aimed at getting information on the YN and YY interactions. (3) Precision structure calculations with model YN and YY interactions are compared with the γ-ray data to test their quality. The few-body studies by Hiyama *et al.* [11, 12, 13, 14, 15, 16] using GEM are theoretical contribution to the step (3). The work of Ref.[14] tested two types of YN spin-orbit forces, based on meson theory [17, 18] and the other based on a quark model [19], predicting the spin-orbit splitting energies in ${}^{9}_{\Lambda}\mathrm{Be}$ and ${}^{13}_{\Lambda}\mathrm{C}$. Later γ spectroscopy experiments [20, 21] suggested a very weak spin-orbit splitting, which was in good agreement with the prediction using the quark-based spin-orbit force. This detailed comparison of the theory and experiment was possible because of the precise three- and four-body model calculations for the ${}^{9}_{\Lambda}\mathrm{Be}(= 2\alpha + \Lambda)$ and ${}^{13}_{\Lambda}\mathrm{C}(= 3\alpha + \Lambda)$ systems taking into proper account of the Pauli principle between nucleons [14].

Another example in hypernuclear physics is the work of Hiyama *et al.* [15]. They succeeded in performing difficult four-body calculations of ${}^{4}_{\Lambda}\mathrm{H}$ and ${}^{4}_{\Lambda}\mathrm{He}$, taking the $\Lambda - \Sigma$ conversion explicitly into account, for the first time in both $NNN\Lambda$ and $NNN\Sigma$ channels. This enabled them to analyze precisely the role of the $\Lambda - \Sigma$ conversion in those hypernuclei which had for a long time been a subject of investigations of various authors [22, 23, 24] to see the effect of the conversion on the binding energies, the charge-symmetry breaking, the role of ΛNN three-body force, etc.

The Gaussian Expansion Method was proposed by Kamimura [4, 5] some 15 years ago to carry out non-adiabatic three-body calculations of muonic molecules and muon-atomic collisions. Those systems are very good testing grounds for atomic and molecular models and few-body calculations since there are more observable quantities than those in the analogous electron systems because of large muon mass. The structure of muonic molecule $dt\mu$ and muon transfer reaction $(d\mu)_{1s} + t \rightarrow (t\mu)_{1s} + d$ are of particular interest since they are the key to muon catalized fusion (μCF) (for example, the review articles [25, 26, 27, 28]). An accuracy of up to seven significant figures in the calculated binding energy and the accurate wave function in the tail region was required for the very weakly bound excited $J = 1$

state in order to derive the asymptotic normalization constant to be used for the calculation of the molecular formation probability. The calculation using GEM satisfied this. Since the muon mass is 207 times the electron mass, non-adiabatic treatment of the three charged particles is necessary. This difficulty, as well as the practical interest in the energy production by μCF has been stimulating studies of the problems by means of various methods in nuclear physics, atomic/molecular physics and quantum chemistry. Among the methods, GEM has made one of the best contributed to a variety of three-body scattering and bound-state problems appearing in μCF.

In a usual variational method for three-body bound states, Hamiltonian is diagonalized in a space spanned by a finite number of L^2 basis functions. Characteristics of GEM are as follows:

(i) The basis set consists of functions of Jacobian coordinates, $(\mathbf{r}_c, \mathbf{R}_c)$, of *all* the three rearrangement channels ($c = 1 - 3$) shown in Fig. 1, each base being in the form $\phi_{n_c l_c}(r_c)\psi_{N_c L_c}(R_c)[Y_{l_c}(\hat{\mathbf{r}}_c)\, Y_{L_c}(\widehat{\mathbf{R}}_c)]_{JM}$ with obvious notations for angular momenta, n_c and N_c specifying the radial dependence.

(ii) The radial dependence is Gaussian, $\phi_{nl}(r) = r^l e^{-\nu_n r^2}$ and similarly for $\psi_{NL}(R)$, with the range parameters forming a geometric progression, $\{\nu_n = \nu_1 a^{n-1};\ n = 1 - n_{\max}\}$.

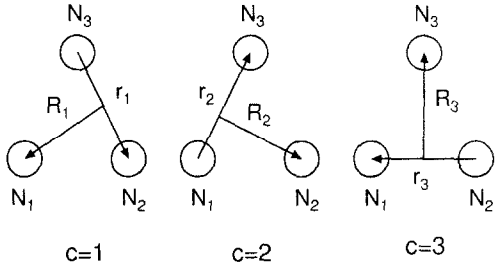

Figure 1: Three Jacobian coordinates of three-body system.

Prescription (i) for preparing the basis functions in three channels makes the function space significantly larger (even if l and L are strongly restricted) than the case using the basis functions of a single channel alone but makes the non-orthogonality between the basis functions much less troublesome than in the latter case. These types of three-channel basis functions are particularly suitable for describing a weakly bound system along any of the R_c as well as for describing strong short-range correlations along any of the r_c ($c = 1 - 3$). Prescription (ii) for the Gaussian ranges has been found to be very suitable for accurately describing both the short-range correlations and the long-range tail behavior in the asymptotic region of few-body wave functions. The Gaussian shape of basis functions makes the calculation of matrix elements easy even between basis functions of different channels. Thus, prescriptions (i) and (ii) are the main reasons for the success of GEM in various types of three-body bound and quasi-bound states such as muonic molecules [4, 25], three-nucleon bound states (^{3}H, ^{3}He) [6, 7], unstable nuclei, [29, 30] antiprotonic helium atoms [3, 10, 31, 32].

As mentioned before, precision three-body calculations with GEM contributed to the determination of the first recommended value of antiproton mass from the spectroscopic study of the antiprotonic helium atom ($\mathrm{He}^{2+} + e^- + \bar{p}$). The study of this system is one of the most difficult three-body problems because of the following reasons: (i) It is a Coulomb three-body problem of heavy-heavy-light system. (ii) The total angular momenta concerned are as high as $J \sim 30 - 40\hbar$. (iii) The excited states to be studied are not true bound states but so-called Feshbach resonances. (iv) The inter-nuclear motion between the helium nucleus ($Z = +2$) and the antiproton ($Z = -1$) is not adiabatic when they are close to each other. (v) Correlation between the electron and antiproton should be precisely taken into account. (vi) Accuracy of eight significant figures in the transition energy (ten digits in eigenenergy) is required to compare with the laser experiment of the transition frequency. There have been only two groups that succeeded in overcoming these difficulties; Kino *et al.* [3, 10, 31, 32] using GEM and Korobov

[33, ?, ?, 35, 36] who employed the expansion of the atomic coordinates. Physics with the antiprotonic helium atoms will be discussed.

When we proceed to four-body systems, calculation of the Hamiltonian matrix elements becomes much laborious. In order to make the calculation tractable even for complicated interactions, we replace the Gaussian basis function, $r^l e^{-\nu_n r^2} Y_{lm}(\hat{\mathbf{r}})$, by a superposition of infinitesimally-shifted Gaussians, $\lim_{\varepsilon\to 0} \frac{1}{\varepsilon^l} \sum_{k=1}^{k_{\max}} C_{lm,k}\, e^{-\nu(\mathbf{r}-\varepsilon \mathbf{D}_{lm,k})^2}$, whose parameters $\{C_{lm,k}, \mathbf{D}_{lm,k};\ k = 1 - k_{\max}\}$ are so determined that the latter is equivalent to the former. We make similar replacement of the basis functions in all the other Jacobian coordinates. Thanks to the absence of the spherical harmonics, use of the latter functional forms makes the matrix element calculation extremely easy in practice with no tedious angular-momentum algebra. The technique of infinitesimally-shifted Gaussians [37, 38] have been applied to various three- and four-body calculations in hypernuclear physics [11, 12, 13, 14, 15, 16] as well as four-nucleon bound states [39] and double-muonic molecules [99].

A stringent test of accuracy of GEM was made in Ref. [6] in the calculation of three-nucleon bound states using a realistic NN interaction. The calculation of the binding energies and some properties of the wave functions, including the asymptotic normalization constants, agreed with the results of the 34-channel Faddeev calculations. Practicality of the infinitesimally-shifted Gaussian basis functions was demonstrated in a benchmark test calculation [39] of the four-nucleon bound state (^{4}He) using a realistic NN force; in this collaboration of seven groups, agreement between the results of the seven calculational schemes was essentially perfect. Recently, the same method was applied to the second 0^+ state of the ^{4}He nucleus by Hiyama *et al.* [40]; a four-body calculation of $^4\mathrm{He}(e,e')^4\mathrm{He}(0_2^+)$ using a realistic NN force was performed for the first time. The observed electron scattering form factor was reproduced well.

An advatage of GEM is as follows. Diagonalization of Hamiltonian automatically yields not only the lowest eigenstate but also many excited eigenstates having the same spin and parity, J^π. Some of the excited eigenstates are supposed to correspond to observed bound and/or resonance states, and the others are considered to be so-called *pseudo*-states representing non-resonant continuum states in discretized form. A good example is the four-nucleon GEM calculations [39, 40] mentioned above with a simultaneous calculation of the ground state, the second 0^+ state, and the distribution of monopole strengths in the discretized 0^+ continuum states. In the case of two-body systems, we tested and confirmed that such eigenstates form an approximate complete set in a sufficiently wide finite space. We consider that a large number of eigenstates obtained by GEM constitutes an approximate complete set also in three-body systems in a finite but sufficiently large space. This property makes it possible to extend GEM to three-body scattering problems.

An application of GEM to scattering problems has been performed in Coulomb three-body reactions appearing in the cycle of muon catalyzed fusion. We review the GEM calculations [41, 42] of two types of important reactions in μCF, muon transfer reactions $(d\mu)_{1s} + t \to d + (t\mu)_{1s} + 48\,\mathrm{eV}$ and decay of the muonic molecule $(d\mathrm{He}\mu)$, which have been stimulating the development of Coulomb three-body reaction theories. Essence of the method is as follows. The total wave function is divided into two parts; one is for describing open-channel amplitudes in a usual manner and the other is for amplitude of all the closed channels which vanish asymptotically. The latter is expanded by the approximate complete set of the three-body eigenstates which are obtained by diagonalzing the three-body Hamiltonian with the Gaussian basis functions.

Another application of GEM is to the study of projectile breakup processes in combination with the method of Continuum-Discretized Coupled Channels (CDCC) [43, 44]. CDCC has been successful in describing nuclear reactions involving breakup processes of weakly bound projectiles [43, 44, 45, 46, 47, 48, 49, 50, 51, 52] and of unstable nuclei [53, 54]. CDCC has been attracting a great deal of attention since the advent of experiments using radioactive beams because projectile breakup processes are in general essential to such reactions. CDCC solves the three-body dynamics by discretizing continuous intrinsic states of projectile into a finite number of discrete ones. So far, the projectile has been

assumed to consist of two particles. However, reactions induced by unstable nuclei such as ^{6}He($=\alpha+n+n$), ^{8}B($=\alpha+{}^3$He$+p$),[11] Li($=\,^9$Li$+n+n$) are typical examples of projectiles composed of three particles (clusters). In such cases, it is reasonable to discretize continuum intrinsic states of the three-body projectile in terms of the pseudo-states (eigenstates) obtained by means of GEM with diagonalization of the projectile intrinsic Hamiltonian with the Gaussian basis functions.

In spite of many successful examples of the use of the Gaussian and infinitesimally-shifted Gaussian basis functions in the few-body calculations as mentioned above, it was hard to describe accurately highly-oscillatory wave functions having more than several nodes, since the Gaussians themselves had no radial nodes. In this paper we propose an improvement to overcome this difficulty by introducing new types of functions each of which has radial oscillations, namely, Gaussians multiplied by trigonometric functions, $r^l\, e^{-\nu_n r^2}\cos\alpha\nu_n r^2$ and $r^l\, e^{-\nu_n r^2}\sin\alpha\nu_n r^2$ ($n=1-n_{\max}$). They are respectively rewritten as $r^l(e^{-\eta_n r^2}+e^{-\eta_n^* r^2})/2$ and $r^l(e^{-\eta_n r^2}-e^{-\eta_n^* r^2})/2i$ with *complex* sizes $\eta_n=(1+i\,\alpha)\,\nu_n$ and $\eta_n^*=(1-i\,\alpha)\,\nu_n$. We refer to these oscillating functions as complex-range Gaussians. To take $\alpha\sim\pi/2$ is recommendable. We shall show later that use of these basis functions makes it possible to represent oscillating functions having more than 20 radial nodes accurately. Calculations of the Hamiltonian matrix elements between the complex-range Gaussians can be performed with essentially the same computer program for the real-size Gaussians with some real variables replaced by complex ones; this is another advantage of adopting the complex-range Gaussians. Use of these new types of Gaussians makes the applicability of GEM much wider than hitherto.

Construction of this paper is as follows: In Section 2, the basis functions mentioned above are described precisely and tested for two-body systems. GEM is presented and tested for three-body systems in Section 3 and on four-body systems in Section 4. Section 5 shows an application of GEM to the three-body problems in the muon catalyzed fusion cycles. In Section 6, we present a precision three-body analysis of the laser spectroscopy of antiprotonic helium atoms and the latest determination of antiproton mass by GEM. Section 7 demonstrates successful application of GEM with infinitesimally-shifted Gaussian basis functions to the study of three- and four-body structure of light hypernuclei. In Section 8, Coulomb three-body reactions are studied. An extension of the CDCC method with GEM to four-body breakup processes is discussed in Section 9. Summary is given in Section 10. In Appendix, we present some details of calculational method for Gaussian and infinitesimally-shifted Gaussian basis functions.

2 Gaussian Basis Functions: Test for Two-body Systems

We consider how to solve the Schrödinger equation for bound states of a few-body system with the total angular momentum J and the z-component M

$$(H-E)\Psi_{JM}=0 \tag{1}$$

using the variational method. In what follows, the other quantum numbers such as parity and isospin are omitted for simplicity. We expand the total wave function in terms of a set of L^2-integrable basis functions $\{\Phi_{JM,n}; n=1-n_{\max}\}$ as

$$\Psi_{JM}=\sum_{n=1}^{n_{\max}} C_n^{(J)}\,\Phi_{JM,n}. \tag{2}$$

The Rayleigh-Ritz variational principle leads to a generalized matrix eigenvalue problem

$$\sum_{n'=1}^{n_{\max}}(H_{nn'}^{(J)}-EN_{nn'}^{(J)})\,C_{n'}^{(J)}=0\,, \tag{3}$$

where the energy and overlap matrix elements are given by

$$\begin{aligned} H_{nn'}^{(J)} &= \langle\,\Phi_{JM,n}\,|\,H\,|\,\Phi_{JM,n'}\,\rangle, \\ N_{nn'}^{(J)} &= \langle\,\Phi_{JM,n}\,|\,1\,|\,\Phi_{JM,n'}\,\rangle. \end{aligned} \tag{4}$$

By solving the eigenvalue problem, we can obtain not only the lowest state but also the excited state eigenfunctions with the same J and parity (and some other quantum numbers); this is an advantage of the Rayleigh-Ritz variational principle.

An important issue of the variational method is how to select a good set of basis functions $\{\Phi_{JM,n}; n = 1 - n_{\max}\}$. There are many candidates for two-body systems. However, for systems with more than two bodies, construction of a good set of basis functions is not easy, and calculation of the matrix elements becomes much laborious. From this point of view, the (complex-range) Gaussian functions written in the Jacobian coordinates of all the rearrangement channels are particularly suitable not only for the calculation of the matrix elements but also for describing, for example, short-range correlations, long-range tail behavior and highly oscillatory character of few-body wave functions, etc.

We shall show that resulting eigenfunctions $\{\Psi^{(i)}_{JM}; i = 1 - n_{\max}\}$ obtained by diagonalizing the Hamiltonian with (complex-range) Gaussian basis functions form an approximate orthonormal complete set in a finite but sufficiently large space so that they can well reproduce both bound and continuum states within that region. In this section, usefulness of the (complex-range) Gaussian basis functions will be examined in the two-body cases.

2.1 A set of Gaussians with ranges in geometric progression

Let us consider the two-body Schrödinger equation

$$\left[-\frac{\hbar^2}{2\mu}\nabla^2 + V(r) - E \right] \psi_{lm}(\mathbf{r}) = 0 \tag{5}$$

where μ is the reduced mass and $V(r)$ is a central potential. We expand $\psi_{lm}(\mathbf{r})$ in terms of a set of Gaussian basis functions, $\phi^{\mathrm{G}}_{nlm}(\mathbf{r}) = \phi^{\mathrm{G}}_{nl}(r)Y_{lm}(\hat{\mathbf{r}})$, with given range parameters:

$$\psi_{lm}(\mathbf{r}) = \sum_{n=1}^{n_{\max}} c_{nl}\, \phi^{\mathrm{G}}_{nlm}(\mathbf{r}) \,, \tag{6}$$

$$\phi^{\mathrm{G}}_{nlm}(\mathbf{r}) = \phi^{\mathrm{G}}_{nl}(r)Y_{lm}(\hat{\mathbf{r}}) \,, \tag{7}$$

$$\phi^{\mathrm{G}}_{nl}(r) = N_{nl}\, r^l\, e^{-\nu_n r^2} \,, \tag{8}$$

$$N_{nl} = \left(\frac{2^{l+2}(2\nu_n)^{l+\frac{3}{2}}}{\sqrt{\pi}\,(2l+1)!!} \right)^{\frac{1}{2}} \qquad (n = 1 - n_{\max}), \tag{9}$$

The constant N_{nl} is for normalization $\langle\, \phi^{\mathrm{G}}_{nlm} \mid \phi^{\mathrm{G}}_{nlm} \,\rangle = 1$. Note that the set $\{\phi^{\mathrm{G}}_{nlm}; n = 1 - n_{\max}\}$ is a non-orthogonal set.

Such an expansion with high accuracy is in fact possible with little effort in the optimization of the parameters. For our many successful experiences, it seems that the best set of Gaussian size parameters are those in geometric progression

$$\begin{aligned} \nu_n &= \frac{1}{r_n^2} \,, \\ r_n &= r_1\, a^{n-1} \quad (n = 1 - n_{\max}) \,. \end{aligned} \tag{10}$$

There are three parameters, $\{n_{\max}, r_1, r_{n_{\max}}\}$ or $\{n_{\max}, r_1, a\}$ of which we use the former type throughout this paper. Because of Eq. (10), the non-orthogonal basis functions $\phi^{\mathrm{G}}_{nl}(r)$ satisfy the condition that the overlap between the nearest neighbors, $\langle\, \phi^{\mathrm{G}}_{nl} \mid \phi^{\mathrm{G}}_{n-1l} \,\rangle$, is a constant independent of n, which is considered to be one of the reasons why the expansion works well.

The expansion coefficients $\{c_{nl}\}$ and the eigenenergy E are determined by the Rayleigh-Ritz variational principle, which leads to a generalized matrix eigenvalue problem:

$$\sum_{n'=1}^{n_{\max}} \left[\, (T_{nn'} + V_{nn'}) - E\, N_{nn'} \,\right] c_{n'l} = 0 \,, \qquad (n = 1 - n_{\max}). \tag{11}$$

The matrix elements are given by

$$N_{n,n'} = \langle \phi^{\rm G}_{nlm} \mid \phi^{\rm G}_{n'lm} \rangle = \left(\frac{2\sqrt{\nu_n \nu_{n'}}}{\nu_n + \nu_{n'}} \right)^{l+\frac{3}{2}} , \tag{12}$$

$$T_{n,n'} = \langle \phi^{\rm G}_{nlm} \mid -\frac{\hbar^2}{2\mu}\nabla^2 \mid \phi^{\rm G}_{n'lm} \rangle = \frac{\hbar^2}{\mu} \frac{(2l+3)\nu_n \nu_{n'}}{\nu_n + \nu_{n'}} \left(\frac{2\sqrt{\nu_n \nu_{n'}}}{\nu_n + \nu_{n'}} \right)^{l+\frac{3}{2}} , \tag{13}$$

$$V_{n,n'} = \langle \phi^{\rm G}_{nlm} \mid V(r) \mid \phi^{\rm G}_{n'lm} \rangle = N_{nl} N_{n'l} \int_0^\infty r^{2l} e^{-(\nu_n + \nu_{n'})r^2} V(r) r^2 dr . \tag{14}$$

For three explicit forms of $V(r)$, we have

$$\langle \phi^{\rm G}_{nlm} \mid r^2 \mid \phi^{\rm G}_{n'lm} \rangle = \frac{l+\frac{3}{2}}{\nu_n + \nu_{n'}} \left(\frac{2\sqrt{\nu_n \nu_{n'}}}{\nu_n + \nu_{n'}} \right)^{l+\frac{3}{2}} , \tag{15}$$

$$\langle \phi^{\rm G}_{nlm} \mid \frac{1}{r} \mid \phi^{\rm G}_{n'lm} \rangle = \frac{2}{\sqrt{\pi}} \frac{2^l\, l!}{(2l+1)!!} \sqrt{\nu_n + \nu_{n'}} \left(\frac{2\sqrt{\nu_n \nu_{n'}}}{\nu_n + \nu_{n'}} \right)^{l+\frac{3}{2}} , \tag{16}$$

$$\langle \phi^{\rm G}_{nlm} \mid e^{-\mu r^2} \mid \phi^{\rm G}_{n'lm} \rangle = \left(\frac{2\sqrt{\nu_n \nu_{n'}}}{\nu_n + \nu_{n'} + \mu} \right)^{l+\frac{3}{2}} . \tag{17}$$

(18)

2.2 Short-range correlation and long-range asymptotic behavior

A property which is required for a good set of variational basis functions for few-body systems is the ability to describe accurately any rapid change of the wave function in the short-range region (short-range correlations) and the long-range tail behavior in the asymptotic region. In this subsection, we give two examples for two-body systems. We emphasise that the same is also true for three-body systems as will be shown in Section 3.

Test for ^{4}He atomic dimer

One of the very difficult two-body potential problems is to solve the Schrödinger equation for the very shallow bound state of the ^{4}He atomic dimer in the HFDHE2 potential [55] (Fig. 2) :

$$V(r) = \epsilon \left[A e^{-\alpha x} - \left(\frac{C_6}{x^6} + \frac{C_8}{x^8} + \frac{C_{10}}{x^{10}} \right) F(x) \right], \quad (x = \frac{r}{r_m})$$
$$F(x) = \begin{cases} e^{-(D/x-1)^2} & (x < D) \\ 1 & (x \geq D) , \end{cases} \tag{19}$$

with $r_m = 2.9673$ Å, $\epsilon = 10.6$ K, $A = 0.5448504 \times 10^6$, $\alpha = 13.353384$, $C_6 = 1.3732412$, $C_8 = 0.4253785$, $C_{10} = 0.178100$ and $D = 1.241314$. We adopted a value of $\hbar^2/M = 12.12$ K Å[56].

A direct numerical calculation by the step-by-step method gives $E = -0.0008297$ K and the wave function illustrated in Fig. 3. Since this potential has a strong repulsive core accompanied by a shallow attractive tail which results in the weak binding, one might think that it would be almost impossible for any variational approach to accurately reproduce this result, particularly the wave function. But, diagonalization of the Hamiltonian using our basis functions with the set $\{n_{\max} = 60, r_1 = 0.14$ Å, $r_{n_{\max}} = 700$ Å$\}$ gives the same energy and wave function as those with direct numerical method as shown in Fig. 3. The difference between the two wave functions is less than 0.01 % for $r \sim 150$ Å and 0.1 % out to $r \sim 750$ Å beyond which Gaussian-damped behavior appears gradually. The r.m.s. radius is so large as 88.20 Å.

It is striking that both the short-range correlations and the exponentially-damped tail are simultaneously reproduced extremely accurately. This owes to the geometric-progression Gaussian ranges which have

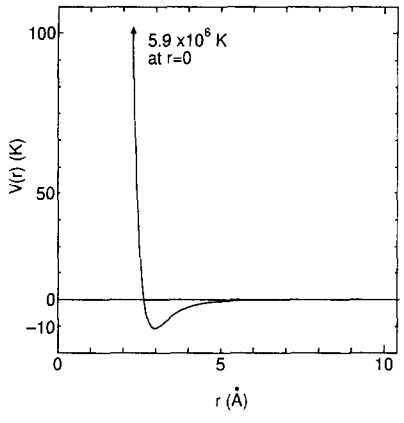

Figure 2: Potential $V(r)$ between ^{4}He atoms defined by Eq. (19) in units of K, r being in units of Å.

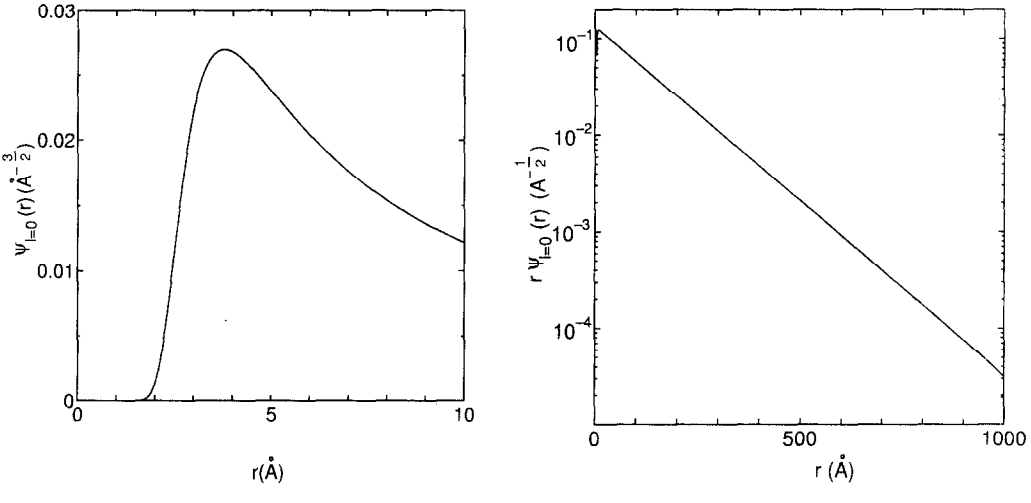

Figure 3: Wave function of the ^{4}He dimer with the potential in Eq. (19): (a) the short-range region ($\psi_{l=0}(r)$); (b) the asymptotic region ($r\,\psi_{l=0}(r)$). The solid line is calculated using the direct numerical method and the present variational method with the Gaussian expansion, Eq. (6), with the set $\{n_{\max} = 60,\ r_1 = 0.14\,\text{Å},\ r_{n_{\max}} = 700\ \text{Å}\}$. $\sqrt{< r^2 >} = 88.20$ Å. Difference between the two results is not visible since it is less than 0.01 % up to $r \sim 150$ Å and 0.1 % out to $r \sim 750$ Å beyond which Gaussian-damped behavior appears gradually.

a dense distribution in the short-range region and a coherent superposition of long-range Gaussians in the asymptotic region. It would be difficult to reach this degree of agreement if one were to choose the Gaussian ranges stochastically.

Test for deuteron

Next, let us examine a nuclear two-body potential problem, the deuteron ground state for the NN potential:

$$V(r) = (-626.885\,e^{-1.55r} + 1438.72\,e^{-3.11r})/r, \qquad \hbar/m = 41.47\text{MeV} \quad (E = -2.2307\text{MeV}) \tag{20}$$

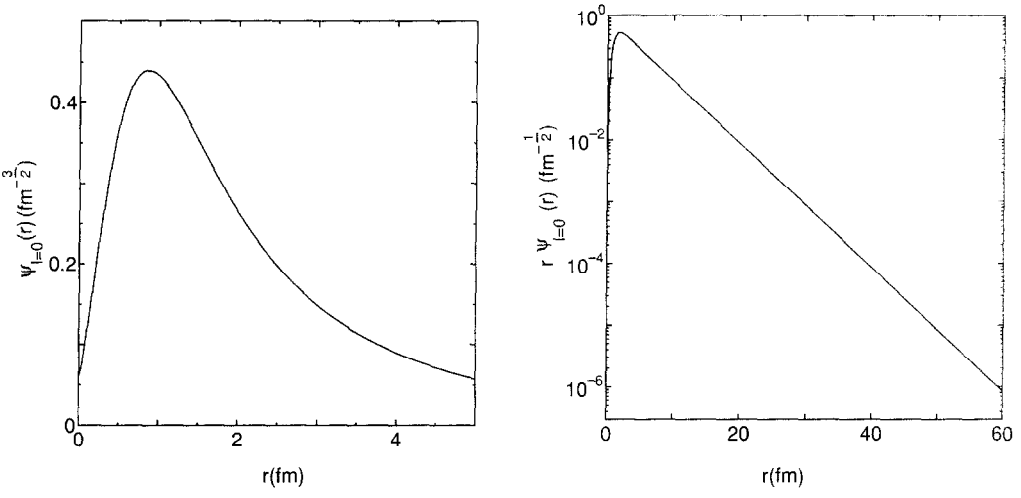

Figure 4: Wave function of the deuteron with the potential in Eq.(20): (a)the short-range region ($\psi_{l=0}(r)$); (b) the asymptotic region ($r\,\psi_{l=0}(r)$). The solid line is calculated using the direct numerical method and the present variational method with the Gaussian expansion, Eq.(6), with the set $\{n_{\max} = 30,\ r_1 = 0.02\,\mathrm{fm},\ r_{n_{\max}} = 30\,\mathrm{fm}\ \}$. The difference between the two results is not visible since it is relatively less than 0.01% up to $r \sim 30\,\mathrm{fm}$ and 0.1 % out to ~ 50 fm beyond which Gaussian-damped behavior appears gradually.

which is a slightly modified Malfliet-Tjon I-III model and was used for a benchmark test paper for the three-nucleon scattering problem [57].

Diagonarization of the Hamiltonian using Gaussian basis functions with $\{n_{\max} = 30, r_1 = 0.02\,\mathrm{fm}, r_{n_{\max}} = 30\,\mathrm{fm}\ \}$ gives the same energy and wave function as those with direct numerical method as shown in Fig. 4. The difference in the wave function between the variational method and the direct numerical method is less than 0.01 % up to $r \sim 30$ fm and 0.1 % out to ~ 50 fm beyond which Gaussian-damped behavior appears gradually.

Again, the exponential-damping of the wave function in the asymptotic region is well reproduced by the resultant superposition of the Gaussians with ranges in a geometric progression. It is straightforward to extend the accurate asymptotic region further using additional Gaussians as needed.

2.3 Approximate complete set in a finite region

By solving the eigenvalue problem of Eq. (11), we obtain an orthonormal set of eigenstates (6), namely $\{\psi^{(i)}_{lm}(\mathbf{r}); i = 1 - n_{\max}\}$. Some of them are bound states and the others are 'pseudo-states' representing discretized continuum states. We consider that the set of discrete states $\{\psi^{(i)}_{lm}(\mathbf{r}); i = 1 - n_{\max}\}$ form a complete set with good accuracy in a finite region of r up to some upper bound and that exact continuum states are well expanded by the set in the finite region. This is examined below for the continuum states of deuteron and ^{6}Li$(= \alpha + d)$ [58].

Deuteron continuum states

We consider a quadrupole transition from the deuteron ground state to the $l = 2$ continuum states. A central $n - p$ potential is employed; $V_{np}(r) = v_0\, e^{-(r/r_0)^2}$ with $v_0 = -72.15$ MeV and $r_0 = 1.484$ fm which reproduces the radius and the binding energy of deuteron. We first solved Eq. (5), using the direct numerical method, for the $l = 0$ ground state, $\psi_{\mathrm{g.s.}}$, and $l = 2$ continuum states with momentum

k, $\psi_{2m}(k,\mathbf{r})$, and calculated the quadrupole transition strength to the k-continuum which is defined as

$$B^{(2)}(k) = |\,\langle\,\psi_{2m}(k)\,|r^2\,Y_{2m}\,|\,\psi_{\rm g.s.}\rangle\,|^2. \tag{21}$$

$B^{(2)}(k)$ is illustrated in Fig. 5 for $k \leq 1.3$ fm^{-1} ($E_{\rm cm} \leq 70$ MeV).

Next, taking the Gaussian basis set $\{\phi^{\rm G}_{n,2m}(\mathbf{r});\ n = 1 - n_{\rm max}\}$ with $\{n_{\rm max} = 20,\ r_1 = 0.5\,{\rm fm},\ r_{n_{\rm max}} = 20.0\,{\rm fm}\ \}$, we solved Eq. (3) for $l = 2$ and obtained an orthonolmal set of discrete states $\{\psi^{(i)}_{2m}(\mathbf{r}); i = 1 - n_{\rm max}\}$. We then calculated the quadrupole transition strength to each pseudostates by

$$B^{(2)}_i = |\langle\psi^{(i)}_{2m}\,|r^2 Y_{2m}|\,\psi_{g.s.}\rangle|^2 \qquad (i = 1 - n_{\rm max}). \tag{22}$$

As shown in Fig. 6, the discrete distribution of $B^{(2)}_i$ simulates qualitatively the continuous k-distribution of $B^{(2)}(k)$ in Fig. 5. Assuming completeness of the pseudostate set $\{\psi^{(i)}_{2m}(\mathbf{r}); i = 1 - n_{\rm max}\}$, we derive the smooth distribution $B^{(2)}(k)$ approximately by

$$B^{(2)}_{\rm ps}(k) = |\sum_{i=1}^{n_{\rm max}} \langle\,\phi_{2m}(k)\,|\,\psi^{(i)}_{2m}\,\rangle\langle\psi^{(i)}_{2m}\,|\,r^2\,Y_{2m}\,|\,\psi_{g.s.}\rangle\,|^2. \tag{23}$$

Both the exact form (21) and the approximate one (23) yield the same continuous distribution as shown in Fig. 5. This means that, at least within the region where $r^2\,\psi_{\rm g.s.}(r)$ is appreciable, the discrete states $\{\psi^{(i)}_2(r); i = 1 - n_{\rm max}\}$ form a complete set with good accuracy.

^{6}Li continuum states

The same test is repeated in the case where a resonance state exists in the continuum. We investigate $l = 2$ continuum of ^{6}Li using the $\alpha + d$ model but neglecting the deuteron spin. An $\alpha - d$ potential of $V(r) = V_0\,e^{-(r/b)^2}$ with $V_0 = -74.19$ MeV and $b = 2.236$ fm generates an $l = 2$ resonace at $E_{\rm cm} = 3.0$ MeV with a width 0.6 MeV.

Exact continuous distribution of the quadrupole transition strength, $B^{(2)}(k)$, is illustrated in Fig. 7 in the region $k \leq 1.3\,{\rm fm}^{-1}(E_{\rm cm} \leq 50\,{\rm MeV})$. We see a resonance and a non-resonant continuum. Figure 8 shows the discrete distribution, $B^{(2)}_i$, to the pseudostates $\{\psi^{(i)}_{2m}(\mathbf{r}); i = 1 - n_{\rm max}\}$ which were obtained using the Gaussian bases with $\{n_{\rm max} = 20,\ r_1 = 1.0\,{\rm fm},\ r_{n_{\rm max}} = 20.0\,{\rm fm}\ \}$. $B^{(2)}_i$ simulates qualitatively the continuous distribution of $B^{(2)}(k)$ in Fig. 7.

Using (23) we calculated the approximate smooth distribution $B^{(2)}_{\rm ps}(k)$. As shown in Fig. 7, both the exact form (21) and the approximate one (23) yield the same continuous distribution, not only the non-resonant continuum but also the resonance. This means again that the discrete states $\{\psi^{(i)}_{2m}(\mathbf{r}); i = 1 - n_{\rm max}\}$ form a complete set with good accuracy at least within the region where $r^2\,\psi_{\rm g.s.}(\mathbf{r})$ significant.

2.4 Complex-range Gaussian basis functions

As seen in the previous section, the expansion in terms of Gaussian basis functions, Eqs.(6) – (9), is suitable for representing short-range correlations and the long-range tail behavior. However, it is difficult to reproduce highly oscillatory functions having more than ~ 5 nodes with good accuracy.

Such oscillating functions can appear in highly excited vibrational states of few-body systems. Also, such functions are necessary to describe the amplitude of a scattering state if one utilizes the Kohn-type variational method for scattering of composite particles [59]. The same is true in discretizing the breakup continuum states in the framework of the CDCC method [43, 44] for projectile breakup reactions.

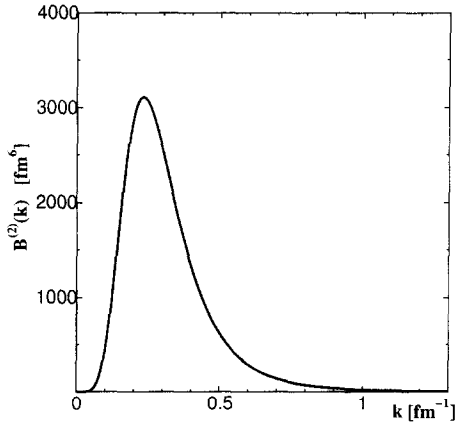

Figure 5: Continuous distribution of the quadrupole transition strengths $B^{(2)}(k)$ and $B^{(2)}_{\rm ps}(k)$ in deuteron as a function of $n-p$ relative momentum k. Difference between the two results is invisible since it is less than 0.1 %.

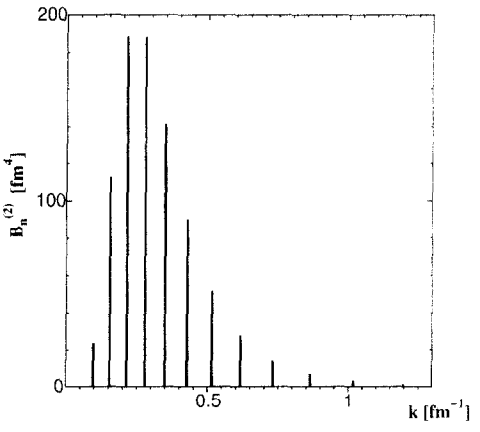

Figure 6: Distribution of the quadrupole transition strength $B^{(2)}_i$ to the discretized $l=2$ continuum states of deuteron.

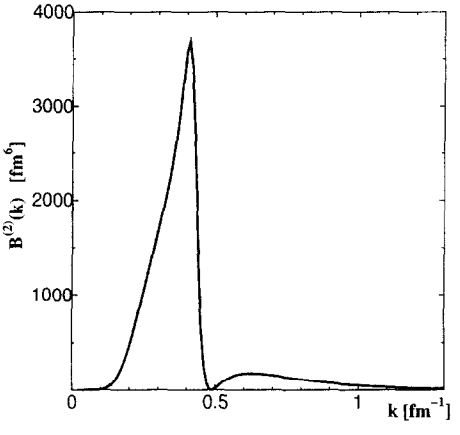

Figure 7: Continuous distribution of the quadrupole transition strengths $B^{(2)}(k)$ and $B^{(2)}_{\rm pse}(k)$ in ^{6}Li as a function of $\alpha-d$ relative momentum k. Difference between the two results is indistinguishable since it is less than 0.1 %.

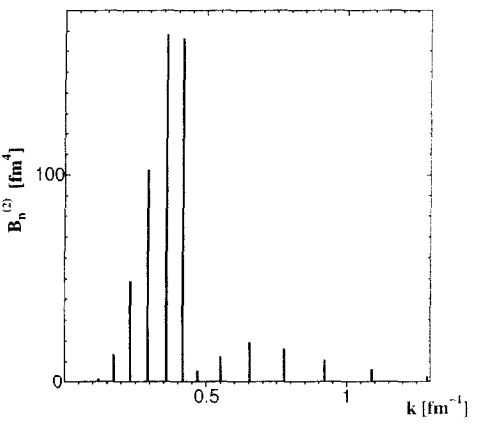

Figure 8: Distribution of the quadrupole transition strength $B^{(2)}_i$ to the discretized $l=2$ continuum states of ^{6}Li.

Although the eigenfunctions of a harmonic oscillator Hamiltonian potential have highly oscillatory members, they are not useful for three- and more-body systems because the calculation of the matrix elements with them is very hard when the coordinate transformations are needed in the integration. One needs good basis functions with highly oscillatory members which are easy to be used for calculations of few-body systems.

Here we propose useful basis functions which satisfy the above requirement in good accuracy. They are Gaussian functions multiplied by *cosine* and *sine* functions :

$$\phi^{\rm GC}_{nl}(r) \;=\; N^{\rm GC}_{nl}\, r^l\, e^{-\nu_n r^2} \cos \alpha\nu_n r^2 \,, \qquad (n=1-n_{\rm max}) \tag{24}$$

$$\phi_{nl}^{\rm GS}(r) = N_{nl}^{\rm GS}\, r^l\, e^{-\nu_n r^2} \sin \alpha\nu_n r^2 . \qquad (n = 1 - n_{\rm max}) \tag{25}$$

The Gaussian sizes ν_n are taken to form a geometric progression in the same manner as in Eq. (10). The parameter α is a free parameter in principle, but numerical tests suggest to take $\alpha \sim \frac{\pi}{2}$ (note that $\cos \alpha\nu_n r^2 = 0$ at $e^{-\nu_n r^2} = e^{-1}$ when $\alpha = \frac{\pi}{2}$).

The reason why the functions $\phi_{nl}^{\rm GC}(r)$ and $\phi_{nl}^{\rm GS}(r)$ are easy to be used in numerical calculations is as follows: They can be rewritten as

$$\phi_{nl}^{\rm GC}(r) = N_{nl}^{\rm GC}\, r^l\, \frac{e^{-\eta_n r^2} + e^{-\eta_n^* r^2}}{2} , \qquad (n = 1 - n_{\rm max}) \tag{26}$$

$$\phi_{nl}^{\rm GS}(r) = N_{nl}^{\rm GC}\, r^l\, \frac{e^{-\eta_n r^2} - e^{-\eta_n^* r^2}}{2i} \qquad (n = 1 - n_{\rm max}) \tag{27}$$

with *complex* size parameters

$$\eta_n = (1 + i\,\alpha)\,\nu_n, \qquad \eta_n^* = (1 - i\,\alpha)\,\nu_n. \tag{28}$$

Calculation of the matrix elements (13)−(14) with the expressions in Eqs.(26) and (27). In this case, the calculation can be done using essentially the same computer program as for real-range Gaussians with some real variables replaced by complex ones. this is an advantage of adopting the complex-range Gaussians. Note that with complex-range Gaussian basis functions, the total number of basis functions is $2n_{\rm max}$.

We have ascertained that the complex-range Gaussian basis functions can expand the deuteron and ^{6}Li continuum states in the same (even better) quality as the Gaussian basis functions do in Figs. 5 and 7. More stringent tests are described below and in Section 2.5. From these tests, we consider that the eigenstates obtained by diagonalizing the Hamiltonian form a complete set in a finite but sufficiently large space where we are interested in.

Test for highly excited states in a harmonic oscillator potential

A good test of the use of complex-range Gaussian basis functions is to calculate the wave functions of highly excited states in a harmonic oscillator potential. We take the case of a nucleon with angular momentum $l = 0$ in a potential having $\hbar\omega = 15.0$ MeV. Parameters of the complex-range Gaussian basis functions are $\{\, 2n_{\rm max} = 28, r_1 = 1.4\,{\rm fm},\ r_{n_{\rm max}} = 5.8\,{\rm fm},\ \alpha = \frac{\pi}{2}\frac{1}{1.2^2} = 1.09 \,\}$. For the sake of comparison, we also tested the Gaussian basis functions with the paramters $\{n_{\rm max} = 28,\ r_1 = 0.5\,{\rm fm},\ r_{n_{\rm max}} = 11.3\,{\rm fm}$ $\}$. Optimized r_1 and $r_{n_{\rm max}}$ are quite different between the two types of bases though the total numbers of basis functions are the same. In Table 1, we compare the calculated energy eigenvalues with the exact ones. It is evident that the complex-range Gaussians can reproduce up to much more highly excited states than the Gausssians do. For the Gaussian basis, even if the number of basis functions is increased, the result is not significantly improved, because the number of oscillation does not increase. On the other hands, for the complex-range Gaussian functions, as the number is increased, the result becomes better so long as the number of oscillation is not too large.

Figure 9 demonstrates good accuracy of the wave function of the 19-th excited state having 38 quanta. Error is within a few %, much smaller than the thickness of the line. The figure suggests that the basis functions is also suitable for describing scattering wave functions in a finite space. This is examined in Section 2.5 for Kohn-type variational method for scattering states and in Section 9 for a new treatment of projectile breakup states in the method of CDCC.

Test for highly excited states of the hydrogen atom

Table 1: Test of accuracy of Gaussian and complex-range Gaussian basis functions for highly excited states ($l = 0$, $n \leq 23$) of a harmonic oscillator potential. The number of basis functions is 28 for both cases. Energies are listed in terms of the number of quanta, $E/\hbar\omega - \frac{3}{2}$.

Exact	Gaussian	complex-range	Exact	Gaussian	complex-range
0.0	0.0000	0.0000	24.0	24.1	24.0001
2.0	2.0000	2.0000	26.0	26.4	26.0001
4.0	4.0000	4.0000	28.0	29.5	28.0003
6.0	6.0000	6.0000	30.0	32.9	30.0003
8.0	8.0000	8.0000	32.0	37.3	32.002
10.0	10.0000	10.0000	34.0	41.8	34.002
12.0	12.0000	12.0000	36.0	47.9	36.002
14.0	14.0000	14.0000	38.0	53.8	38.003
16.0	16.002	16.0000	40.0	62.3	40.1
18.0	17.998	18.0000	42.0	69.9	42.1
20.0	20.01	20.0000	44.0	82.2	44.2
22.0	21.9	22.0000	46.0	91.6	46.3

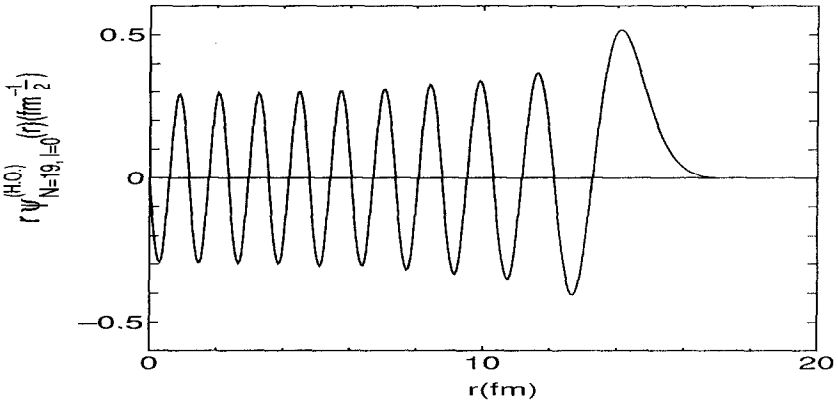

Figure 9: Wave function of the $l = 0$, N=19 state obtained by diagonalizing the harmonic-oscillator-potential Hamiltonian using 28 complex-range Gaussian basis functions. It is compared with the exact wave function but the difference is invisible since the error is less than a few % everywhere. See text for the Gaussian parameters.

We explore another typical example in which the complex-range Gaussian basis functions reproduce highly oscillatory functions with high accuracy. Table 2 lists the calculated energy eigenvalues of the hydrogen atom with $l = 0, n = 1 - 40$ compared with the exact values. Parameters of the complex-range Gaussian basis functions are $\{2n_{\max} = 160, r_1 = 0.015\,\text{a.u.}, r_{n_{\max}} = 2000\,\text{a.u.}, \alpha = 1.5\}$. The energy is reproduced within a relative error of 5×10^{-8} up to the state with $n = 30$. The wave function of the state with $n = 26$ is illustrated in Fig. 10, both for the exact solution and the calculated one. The relative error of the calculated wave function is $10^{-7} - 10^{-5}$ up to $r = 1500$ a.u.. If one does not need such a high precision in the energies and wave functions, the number of basis functions can be significantly reduced.

As an example of using atomic wave functions with such large n, a full four-body GEM calculation is

Table 2: Calculated energy eigenvalues of the hydrogen atom with $l = 0, n = 1 - 40$ compared with the exact values. Parameters of the complex-range Gaussian basis functions are taken to be $\{ n_{\max} = 80,\ r_1 = 0.015\,\text{a.u.},\ r_{n_{\max}} = 2000\,\text{a.u.},\ \alpha = 1.5 \}$.

n	E_{cal} (a.u.)	E_{exact} (a.u.)	relative error
1	$-4.999999845\times10^{-1}$	$-5.000000000\times10^{-1}$	3.1×10^{-8}
2	$-1.249999980\times10^{-1}$	$-1.250000000\times10^{-1}$	1.6×10^{-8}
3	$-5.555555494\times10^{-2}$	$-5.555555556\times10^{-2}$	1.1×10^{-8}
4	$-3.124999974\times10^{-2}$	$-3.125000000\times10^{-2}$	8.4×10^{-9}
5	$-1.999999986\times10^{-2}$	$-2.000000000\times10^{-2}$	6.8×10^{-9}
10	$-4.999999983\times10^{-3}$	$-5.000000000\times10^{-3}$	3.5×10^{-9}
14	$-2.551020402\times10^{-3}$	$-2.551020408\times10^{-3}$	2.5×10^{-9}
18	$-1.543209873\times10^{-3}$	$-1.543209877\times10^{-3}$	2.0×10^{-9}
22	$-1.033057849\times10^{-3}$	$-1.033057851\times10^{-3}$	2.2×10^{-9}
26	$-7.396449686\times10^{-4}$	$-7.396449704\times10^{-4}$	2.4×10^{-9}
30	$-5.555555323\times10^{-4}$	$-5.555555556\times10^{-4}$	4.2×10^{-8}
32	$-4.882807341\times10^{-4}$	$-4.882812500\times10^{-4}$	1.1×10^{-6}
34	$-4.325109595\times10^{-4}$	$-4.325259516\times10^{-4}$	3.5×10^{-5}
36	$-3.856834714\times10^{-4}$	$-3.858024691\times10^{-4}$	3.1×10^{-4}
38	$-3.461488509\times10^{-4}$	$-3.462603878\times10^{-4}$	3.2×10^{-4}
40	$-3.106429115\times10^{-4}$	$-3.125000000\times10^{-4}$	5.9×10^{-3}

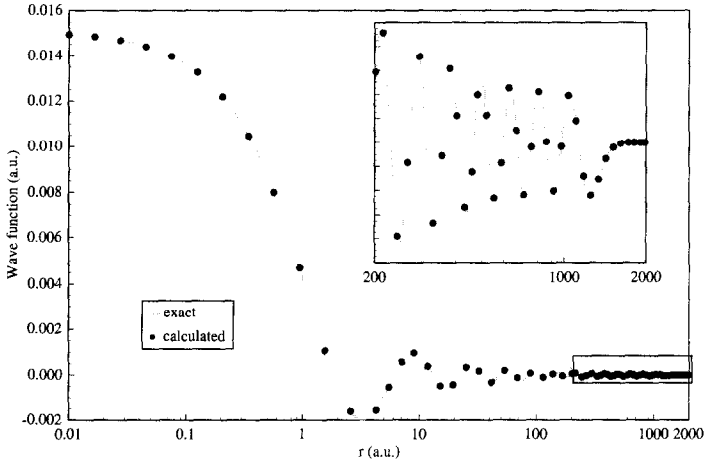

Figure 10: Wave function of the $l = 0$, $n = 26$ state of the hydrogen atom. The solid line is the exact one, and the dots are given by the complex-range Gaussian basis functions with the same parameters as in Table 2. Relative error of the latter is $10^{-7} - 10^{-5}$ up to $r = 1500$ a.u. at which absolute value of the wave function is four-order of magnitude smaller than that at $r = 0$.

underway by the authors on hydrogen-antihydrogen collisions at very low energies (< 1 K) taking into account the coupling between $(pe^-)_{1s} + (\bar{p}e^+)_{1s}$ and $(p\bar{p})_{nl} + (e^-e^+)_{n'l'}$ channels; transition to the latter channels leads to loss of antihydrogen. Here, it is necessary to prepare wave functions of $(p\bar{p})_{nl}$ with $n \sim 24$ in terms of complex-range Gaussians in order to calculate Coulomb matrix elements accurately. As was mentioned in a recent paper on this subject [60], theoretical studies of the collisions can give

an important suggestions for experiments intending to trap and cool antihydrogen for investigating matter-antimatter interaction [61, 62].

2.5 Gaussian expansion of scattering state wave functions

As was examined in Section 2.3, the Gaussian basis functions, $\phi^{\rm G}_{lm}(\mathbf{r})$, form a complete set in a finite space in good accuracy. We have seen that the complex-range Gaussians, $\phi^{\rm GC}_{lm}(\mathbf{r})$ and $\phi^{\rm GS}_{lm}(\mathbf{r})$, are more suitable for describing highly oscillatory states than the Gaussians are. Therefore, the former basis must form a complete set in good accuracy in much larger space than in the case of the latter basis.

In this subsection, we try to expand scattering states in the interaction region in terms of the complex-range Gaussian bases and calculate the S-matrix using the Kohn-type variational method for reactions between composite particles [59]. This method has been employed by many authors in the RGM (resonating group method) and GCM (generator coordinate method) studies of nucleus-nucleus scattering as well as nucleon-nucleon scattering based on the constituent quark model.

We recapitulate the variational method of Ref. [59] for scattering by a simple potential. More complicated cases including the applications in the framework of RGM and GCM are given in [59].

Variational method for scattering states

We solve the Schrödinger equation

$$\left[-\frac{\hbar^2}{2\mu}\frac{d^2}{dr^2}+\frac{\hbar^2 L(L+1)}{2\mu r^2}+U(r)-E\right]u_L(r)=-\int_0^\infty W_L(r,r')\,u_L(r')\,dr \tag{29}$$

under the boundary condition $u_L(0)=0$ and

$$u_L(r)=u_L^{(-)}(\eta,kr)-S_L\,u_L^{(+)}(\eta,kr),\qquad r\geq r_{\rm m}. \tag{30}$$

Here $r_{\rm m}$ is the matching radius, and $u_L^{(-)}(u_L^{(+)})$ is the incoming (outgoing) Coulomb function given by

$$u_L^{(\pm)}(\eta,kr)=G_L(\eta,kr)\pm iF_L(\eta,kr)\,. \tag{31}$$

F_L and G_L are the regular and irregular Coulomb functions, and k is the wave number and η the Sommerfeld parameter.

We define an operator $\mathcal{L}_L$ by

$$\mathcal{L}_L(r,r')\equiv\left[-\frac{\hbar^2}{2\mu}\frac{d^2}{dr^2}+\frac{\hbar^2 L(L+1)}{2\mu r^2}+U(r)-E\right]\delta(r-r')+W_L(r,r') \tag{32}$$

and a symbol $(f\,\mathcal{L}_L\,g)$ by

$$(f\,\mathcal{L}_L\,g)\equiv\int_0^\infty\int_0^\infty f(r)\,\mathcal{L}_L(r,r')\,g(r')\,dr\,dr'\,, \tag{33}$$

where not f^* but f is used in the integrand. Schrödinger equation (29) is written by $\mathcal{L}_L\,u_L=0$.

We introduce a trial function $u_{\rm t}(r)$ for the exact solution $u_L(r)$ and expand $u_{\rm t}(r)$ as

$$u_{\rm t}(r)=\sum_{n=1}^{n_{\rm max}}c_n u_n(r)\,, \tag{34}$$

$$u_n(r)=\begin{cases}a_n\,u_n^{(in)}(r), & r<r_{\rm m}\\ u_L^{(-)}(\eta,kr)-s_n\,u_L^{(+)}(\eta,kr), & r>r_{\rm m}\end{cases} \tag{35}$$

where $\{u_n^{(in)}(r); n = 1 - n_{\max}\}$ are L^2-type basis functions to expand $u_L(r)$ for $r < r_{\rm m}$. Coefficients a_n and s_n are determined by coonecting $u_n(r)$ smoothly at $r_{\rm m}$. From (30) we have

$$\sum_{n=1}^{N} c_n = 1 \,, \tag{36}$$

$$\sum_{i=1}^{N} c_n \, s_n = S_t \,. \tag{37}$$

Equation (36) enables us to eliminate any of the c_n, say c_1, and to rewrite $u_{\rm t}$ as

$$u_{\rm t}(r) = u_1(r) + \sum_{n=2}^{n_{\max}} c_n [\, u_n(r) - u_1(r) \,] \,. \tag{38}$$

Variational partameters are now $\{c_n \,; n = 2 - n_{\max}\}$; S_t itself is not a variational parameter. Kohn's variational principle for S-matrix leads to linear equations

$$(\, [\, u_n - u_1 \,] \, \mathcal{L}_L \, u_{\rm t}) = 0 \,, \qquad (n = 2 - n_{\max}). \tag{39}$$

to determine $\{c_n \,; n = 2 - n_{\max}\}$ and hence the S-matrix S_L by

$$S_L = S_{\rm t} + \frac{i\mu}{\hbar^2 k} \, (u_{\rm t} \, \mathcal{L}_L \, u_{\rm t}) \,. \tag{40}$$

In order to calculate the fundamental matrix elements $(u_n \, \mathcal{L}_L \, u_{n'})$ as analytically as possible, the definition (35) for $u_L(r)$ is not convenient. It may be rewritten with a trivial alternative form as

$$u_n(r) = a_n [\, u_n^{(\rm in)}(r) + u_n^{(\rm ex)}(r) \,] \,, \qquad 0 \le r < \infty \;\; (n = 1 - n_{\max}) \tag{41}$$

$$a_n u_n^{(\rm ex)}(r) = \begin{cases} 0 \,, & r < r_{\rm m} \\ u_L^{(-)}(\eta, kr) - s_n \, u_L^{(+)}(\eta, kr) - a_n u_n^{(\rm in)}(r) \,, & r > r_{\rm m} \,, \end{cases} \tag{42}$$

where $u_n^{(\rm in)}(r)$ is extended to the region $r > r_{\rm m}$ with the same functional form as in $r < r_{\rm m}$. Using integration by parts, we can rewrite $(u_n \, \mathcal{L}_L \, u_{n'})$ as

$$(u_n \, \mathcal{L}_L \, u_{n'}) = a_n a_{n'} (\, [\, u_n^{(\rm in)} + u_n^{(\rm ex)} \,] \, \mathcal{L}_L [\, u_{n'}^{(\rm in)} + u_{n'}^{(\rm ex)} \,] \,) = a_n a_{n'} \{ \, (u_n^{(\rm in)} \, \mathcal{L}_L \, u_{n'}^{(\rm in)}) - (\!(u_n^{(\rm in)} \, \mathcal{L}_L^{(0)} \, u_{n'}^{(\rm in)})\!) \, \} \,. \tag{43}$$

where

$$(\!(f \, \mathcal{L}_L^{(0)} \, g)\!) \equiv \int_{r_{\rm m}}^{\infty} f(r) \, \mathcal{L}_L^{(0)}(r) \, g(r) \, dr \,, \tag{44}$$

with

$$\mathcal{L}_L^{(0)}(r) \equiv -\frac{\hbar^2}{2\mu} \frac{d^2}{dr^2} + \frac{\hbar^2 L(L+1)}{2\mu r^2} + \frac{Z_A Z_B e^2}{r} - E \,. \tag{45}$$

The matrix elements $(u_n^{(\rm in)} \, \mathcal{L}_L \, u_m^{(\rm in)})$ in (43) is the same as those appearing in bound-state calculations, and the additional matrix elements $(\!(u_n^{(\rm in)} \, \mathcal{L}_L^{(0)} \, u_m^{(\rm in)})\!)$ are quite easy to calculate numerically. This is an advantage of the present variational method; scattering problem can be solved almost in the same manner as in the bound-state problem.

In Ref. [59], many techniques for calculating the matrix elements $(u_n^{(\rm in)} \, \mathcal{L}_L \, u_m^{(\rm in)})$ which appear in RGM and GCM calculations for scattering between composite particles such as nucleus-nucleus scattering and nucleon(3q)-nucleon(3q) scattering.

complex-range Gaussians as trial functions

In the work of [59], three types of trial functions $u_n^{(\rm in)}(r)$ were proposed with special attention to how to calculate the matrix elements $(u_n^{(\rm in)} \, W \, u_m^{(\rm in)})$ of the non-local potential $W(r, r')$ which appears in the RGM and GCM calculations of scattering between complex nuclei. Among the basis functions, the

Gaussian basis functions, $r^L e^{-\nu_n r^2}$, were utilized as one of the most tractable basis in many examples, including three-body systems. But, it was hard for the basis functions to reproduce wave functions with more than ~ 5 nodes in the region $r < r_{\rm m}$. There are some L^2-integrable basis functions which are suitable for highly oscillatory wave functions, such as the eigenfunctions of the harmonic oscillator potential, but they are not always convenient for systems having three- or four-body degrees of freedom.

As shown in Section 2.4, the complex-range Gaussian basis functions (24)–(27) are just suitable for such purposes. We propose here to use the basis functions $u_n^{(\rm in)}(r)$ defined below to describe the scattering wave functions $u_L(r)$ in the interaction region ($r \le r_{\rm m}$):

$$\frac{u_n^{(\rm in)}(r)}{r} = \phi_{nL}^{\rm GC}(r)\ , \quad (n = 1 \sim n_{\rm max}) \tag{46}$$

$$\frac{u_n^{(\rm in)}(r)}{r} = \phi_{nL}^{\rm GS}(r)\ , \quad (n = n_{\rm max}+1 \sim 2n_{\rm max})\ . \tag{47}$$

We calculate the wave function and the S-matrix of the α–^{12}C scattering in a test optical potential whose parameters are $V_0 = -100.0$ MeV, $W_0 = -10.0$ MeV, $R_{\rm R} = R_{\rm I} = R_{\rm C} = 4.0$ fm and $a_{\rm R} = a_{\rm I} = 0.5$ fm for $E_{\rm cm} = 25 - 450$ MeV. The matching radius is set at $r_{\rm m} = 8.0$ fm; the wave function should have as many as 20 nodes for $r < r_{\rm m}$ when $E_{\rm cm} = 400$ MeV. Parameters of the trial functions are $\{2n_{\rm max} = 40,\ r_1 = 1.0\,{\rm fm}, r_{20} = 3.6\,{\rm fm},\ \alpha = \pi/2\}$.

The calculated S-matrix elements, $S = |S|e^{2i\delta}$, are listed in Table 3 (upper line for each $E_{\rm cm}$) in comparison with those obtained by the direct numerical method (lower line). The agreement is very good for $E_{\rm cm} \lesssim 400$ MeV. The wave function ($r \le r_{\rm m} = 8.0$ fm) at $E_{\rm cm} = 400$ MeV is illustrated in Fig. 11 togeter with that given by the direct numerical method. Difference between the two results is invisible in the figure since it is within 0.005 in the units of the vertical axis.

The complex-range Gaussian basis functions are extremely good at reproducing the scattering wave function which has some 20 radial nodes in the interaction region. Therefore, the basis functions can be used as accurate and tractable trial functions in RGM and GCM studies of reactions between composite particles up to rather high energies.

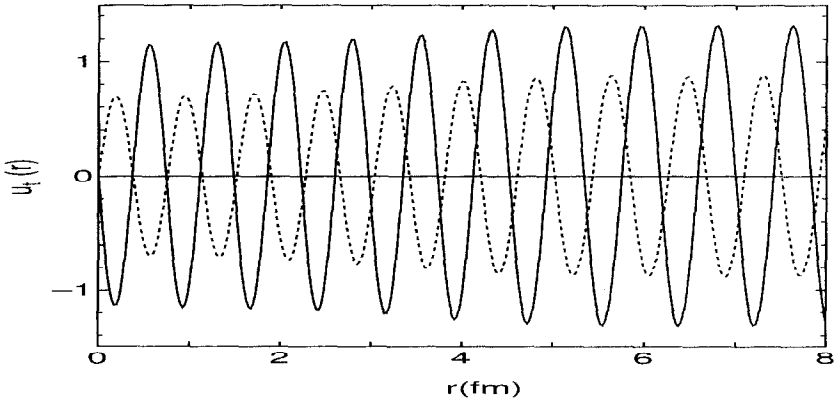

Figure 11: Wave function $u_{\rm t}(r)$ ($r \le r_m = 8.0$ fm) of the α–^{12}C scattering state with $l = 0$ at $E_{\rm cm} = 400$ MeV calculated by the variational method with 40 complex-range Gaussian bases and by the direct numerical method. Difference between both results is indistinguishable since it is within 0.005 in the units of the vertical axis both for the real part (solid line) and the imaginary part (dashed line).

Table 3: Accuracy of the S-matrix calculated by the variational method with the complex-range Gaussian basis functions for the $\alpha - {}^{12}$C elastic scattering at $E_{\rm cm} = 25 - 450$ MeV. The calculated values (upper) are compared with those by the direct numerical method (lower) at each energies. The number of the basis functions is 40. $S = |S|\, e^{2i\delta}$. k is the wave number.

$E_{\rm cm}$ (MeV)	k (fm^{-1})	$\lvert S\rvert$	δ (deg)	$E_{\rm cm}$ (MeV)	k (fm^{-1})	$\lvert S\rvert$	δ (deg)
25.0	1.89	0.2245	120.53	250.0	5.99	0.4341	113.59
		0.2244	120.53			0.4346	113.45
50.0	2.68	0.2624	179.41	275.0	6.28	0.4472	101.71
		0.2624	179.36			0.4478	101.71
75.0	3.28	0.2950	110.70	300.0	6.56	0.4608	91.38
		0.2950	110.68			0.4600	91.31
100.0	3.79	0.3226	64.05	325.0	6.83	0.4718	82.34
		0.3228	64.03			0.4713	82.01
125.0	4.24	0.3467	29.51	350.0	7.09	0.4784	73.71
		0.3469	29.48			0.4819	73.63
150.0	4.64	0.3680	2.50	375.0	7.34	0.4957	66.16
		0.3683	2.48			0.4918	66.03
175.0	5.01	0.3873	160.61	400.0	7.58	0.4989	59.33
		0.3874	160.59			0.5011	59.09
200.0	5.36	0.4050	142.39	425.0	7.81	0.5109	52.24
		0.4047	142.36			0.5098	52.72
225.0	5.68	0.4210	126.97	450.0	8.04	0.5125	47.28
		0.4203	126.86			0.5181	46.85

2.6 Infinitesimally-shifted Gaussian basis functions

In the calculations of the matrix elements of the Hamiltonian of three-body systems, particularly when complicated interactions are employed, integrations over all of the radial and angular coordinates become laborious even with Gaussian basis functions. The difficulty increases when we proceed to four-body problems. But, an important development [30, 37, 38] of our method was made by introducing the infinitesimally-shifted Gaussian basis functions by

$$\phi^{\rm G}_{nlm}(\mathbf{r}) = N_{nl}\, r^l e^{-\nu r^2} Y_{lm}(\hat{\mathbf{r}}) = N_{nl} \lim_{\varepsilon\to 0} \frac{1}{\varepsilon^l} \sum_{k=1}^{k_{\rm max}} C_{lm,k}\, e^{-\nu(\mathbf{r} - \varepsilon \mathbf{D}_{lm,k})^2}. \tag{48}$$

How to determine the parameters, $\{C_{lm,k}, \mathbf{D}_{lm,k};\ k = 1 - k_{\rm max}\}$, is described in Appendix A.2. Taking the limit $\varepsilon \to 0$ is to be carried out after the matrix elements have been calculated analytically. This new set of basis functions makes the calculation of three- and four-body matrix elements very easy. All the advantages of using the usual Gaussian basis functions remain with the new basis functions. With the use of these basis functions a variety of four-body calculations have been performed [12, 14, 15, 16, 39, 99], which will be reviewed in Sections 4, 5 and 7.

Two-body matrix elements

Although the infinitesimally-shifted Gaussian basis functions are particularly useful in three- and four-body problems, it is instructive to show an example of calculating the matrix elements of a Gaussian

potential $v_0\, e^{-\mu r^2}$ in the two-body case. Integration over $\mathbf{r}$ is easily performed as

$$\begin{aligned}&\langle\ \phi^{\rm G}_{nlm}(\mathbf{r})\ |\ v_0\ e^{-\mu r^2}\ |\ \phi^{\rm G}_{n'lm}(\mathbf{r})\ \rangle \\ &=\ v_0\, N_{nl}\, N_{n'l}\ \lim_{\varepsilon,\varepsilon'\to 0}(\varepsilon\varepsilon')^{-l}\ \sum_k\sum_{k'} C_{lm,k}C_{lm,k'}\ \exp\left[-\frac{\nu_n\nu_{n'}}{\nu_n+\nu_{n'}+\mu}(\varepsilon\mathbf{D}^*_{lm,k}-\varepsilon'\mathbf{D}_{lm,k'})^2\right]. \qquad (49)\end{aligned}$$

If we take very small ε and ε' and compute Eq. (49) using the function subprogram for the $\exp[\cdots]$ part, we suffer from a serious round-off error in the summation over k and k' since terms lower-order than $(\varepsilon\varepsilon')^l$ survive. If, instead, we expand the individual $\exp[\cdots]$ with respect to ε and ε', the terms with powers lower than $(\varepsilon\varepsilon')^l$ cancel out by the summation over k and k' due to the definition of our $C_{lm,k}$ and $C_{lm,k'}$. At the end of the calculation of Eq. (49) one is left only with a term proportional to $(\varepsilon\varepsilon')^l$ when ε and $\varepsilon' \to 0$. Therefore, the $\exp[\cdots]$ part of Eq. (49) is replaced by

$$\frac{1}{l!}\left(-\frac{\nu_n\nu_{n'}}{\nu_n+\nu_{n'}+\mu}\right)^l (2\varepsilon\varepsilon'\mathbf{D}^*_{lm,k}\cdot\mathbf{D}_{lm,k'})^l. \qquad (50)$$

Since the $(\varepsilon\varepsilon')^l$ factor cancels with the $(\varepsilon\varepsilon')^{-l}$ in Eq. (49) , the two-body matrix element becomes independent of ε and ε' as

$$\begin{aligned}&\langle\ \phi^{\rm G}_{nlm}(\mathbf{r})\ |\ v_0\ e^{-\mu r^2}\ |\ \phi^{\rm G}_{nlm}(\mathbf{r})\ \rangle \\ &=\ v_0\, N_{nl}\, N_{n'l}\,\frac{1}{l!}\left(-\frac{\nu_n\nu_{n'}}{\nu_n+\nu_{n'}+\mu}\right)^l\ \sum_k\sum_{k'} C_{lm,k}C_{lm,k'}\ (\mathbf{D}^*_{lm,k}\cdot\mathbf{D}_{lm,k'})^l\,. \qquad (51)\end{aligned}$$

Each term on the RHS of Eq. (51) is a product of a term which depends only on the Gaussian size parameters and a term which is only a function of the shift coefficients. The latter can be calculated and stored prior to the matrix element calculation. Because this separation is also possible for three- and four-body matrix elements, the computation is very simple and efficient as shown in Appendix A.3 and A.4.

3 Gaussian Expansion method for Three-Body Systems: Test for ^{4}He-Trimer and $A = 3$ Nuclei

The Gaussian Expansion Method (GEM) for three-body systems is described in the following in the case of central forces alone. We consider Schrödinger equation

$$[\,T + V^{(1)}(r_1) + V^{(2)}(r_2) + V^{(2)}(r_2) - E\,]\,\Psi_{JM} = 0 \qquad (52)$$

where T is the kinetic-energy operator. The three-body total wave function Ψ_{JM} is described as a sum of amplitudes of three rearrangement channels $c = 1-3$ (Fig. 12).

$$\Psi_{JM} = \Phi^{(c=1)}_{JM}(\mathbf{r}_1,\mathbf{R}_1) + \Phi^{(c=2)}_{JM}(\mathbf{r}_2,\mathbf{R}_2) + \Phi^{(c=3)}_{JM}(\mathbf{r}_3,\mathbf{R}_3)\,. \qquad (53)$$

Each amplitude is expanded in terms of the Gaussian basis functions written in Jacobian coordinates $\mathbf{r}_c$ and $\mathbf{R}_c$:

$$\Phi^{(c)}_{JM}(\mathbf{r}_c,\mathbf{R}_c) = \sum_{n_cl_c,N_cL_c} A^{(c)}_{n_cl_c,N_cL_c}\left[\phi^{\rm G}_{n_cl_c}(\mathbf{r}_c)\,\psi^{\rm G}_{N_cL_c}(\mathbf{R}_c)\right]_{JM} \qquad (c=1-3)\,, \qquad (54)$$

where

$$\phi^{\rm G}_{nlm}(\mathbf{r}) = \phi^{\rm G}_{nl}(r)\,Y_{lm}(\hat{\mathbf{r}}), \qquad \phi^{\rm G}_{nl}(r) = N_{nl}\,r^l\,e^{-\nu_n r^2} \qquad (n=1-n_{\max})\,, \qquad (55)$$

$$\psi^{\rm G}_{NLM}(\mathbf{R}) = \psi^{\rm G}_{NL}(R)\,Y_{LM}(\widehat{\mathbf{R}}), \qquad \psi^{\rm G}_{NL}(R) = N_{NL}\,R^L\,e^{-\lambda_N R^2} \qquad (N=1-N_{\max}). \qquad (56)$$

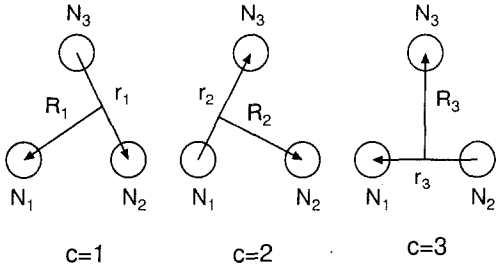

Figure 12: Three Jacobian coordinates of three-body system.

The normalization constants N_{nl} and N_{NL} are shown in Eq.(9), and the Gaussian ranges are given by

$$\nu_n = 1/r_n^2\,, \qquad r_n = r_1\, a^{n-1} \qquad (n = 1 - n_{\max})\,, \tag{57}$$

$$\lambda_N = 1/R_N^2\,, \qquad R_N = R_1\, A^{N-1} \qquad (N = 1 - N_{\max})\,, \tag{58}$$

The numbers and range parameters depend on l_c and L_c but the dependence is omitted for simplicity of notation. l_c and L_c are restricted to $0 \le l_c \le l_{max}$ and $|J - l_c| \le L_c \le J + l_c$. Eigenenergy E and coeffients $A^{(c)}_{n_c l_c, N_c L_c}$ are determined by the Rayleigh-Ritz variational principle. The method of calculation of the interaction matrix element

$$\left\langle \left[\phi^{\rm G}_{n_a l_a}(\mathbf{r}_a)\, \psi^{\rm G}_{N_a L_a}(\mathbf{R}_a) \right]_{JM} \middle| \, V^{(c)}(r_c) \, \middle| \left[\phi^{\rm G}_{n_b l_b}(\mathbf{r}_b)\, \psi^{\rm G}_{N_b L_b}(\mathbf{R}_b) \right]_{JM} \right\rangle \tag{59}$$

for arbitrary functional form of $V^{(c)}(r_c)$ is described in Appendix A.3.

If one employs the infinitesimally-shifted Gaussian functions instead of the Gaussian bases (71) and (56) as

$$\phi^{\rm G}_{nlm}(\mathbf{r}) = N_{nl} \lim_{\varepsilon \to 0} \frac{1}{(\nu\varepsilon)^l} \sum_{k=1}^{k_{\max}} C_{lm,k}\, e^{-\nu_n (\mathbf{r} - \varepsilon \mathbf{D}_{lm,k})^2}\,, \tag{60}$$

$$\phi^{\rm G}_{NLM}(\mathbf{R}) = N_{NL} \lim_{\varepsilon \to 0} \frac{1}{(\lambda\varepsilon)^L} \sum_{K=1}^{K_{\max}} C_{LM,K}\, e^{-\lambda_N (\mathbf{R} - \varepsilon \mathbf{D}_{LM,K})^2}\,, \tag{61}$$

the matrix elements (137) are much more easily calculated without the laborious Racah algebra as described in Appendix A.3.

3.1 Test for ^{4}He-trimer

As seen in Section 2.2, the interaction between two ^{4}He atoms has a very strong repulsive core with weak attractive tail which supports a quite loosely bound state. It is a stringent test of calculational

Table 4: Three-body angular-momentum space (l, L, J) and the Gaussian range parameters for the $J = 0$ states of ^{4}He trimer. Lengths are in units of Å.

l	L	$n_{\max}$	$r_{\min}$	$r_{\max}$	$N_{\max}$	$R_{\min}$	$R_{\max}$
0	0	30	0.14	150.0	22	0.8	650.0
2	2	15	0.30	150.0	15	1.5	250.0

Table 5: Calculated energies of the 0^+ ground and the 0^+ excited states of ^{4}He trimer by the present method and the Faddeev method [56]. No other excited states exist.

^{4}He trimer	$E(0_1^+)$ (K)	$E(0_2^+)$ (K)
present method	-0.114	-0.155×10^{-2}
Faddeev method [56]	-0.11	-0.16×10^{-2}

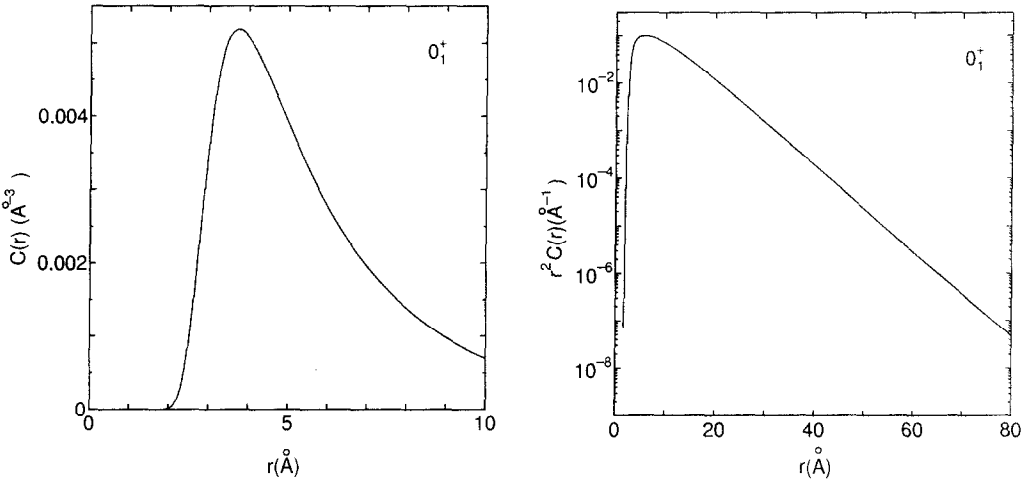

Figure 13: Two-body correlation function $C(r)$ of (63) for the ground state (0_1^+) of ^{4}He trimer obtained by the GEM. Left pannel for the short-range correlations. Right one for the tail which deviates from the exponentially damped behavior for $r > 80$ fm.

methods to solve the bound state of three ^{4}He systems (^{4}He trimer); successful methods should describe properly both the very strong short-range correlations and the long-range tail behavior. This system has also attracted the attention of few-body theoreticians because of Efimov states, but we do not discuss this problem in this paper (for example see [56]).

The ^{4}He-^{4}He potential used here is the same as in Section 2.2. So far, this three-body problem has been solved most accurately by Cornelius and Gloeckle [56] using the Faddeev method with s- and d-wave pair interactions for total $J = 0$ (no bound state for $J > 0$) as shown in Table 5.

In our method, the three-body wave function is described as in (53)–(58). However, since the three particles are identical bosons, $\Phi_{JM}^{(c)}$ in (53) has the same form for $c = 1 - 3$, and therefore Ψ_{JM} is to be expanded as

$$\Psi_{JM} = \sum_{nl,NL} A_{nl,NL} \left\{ \left[\phi_{nl}^{\rm G}(\mathbf{r}_1)\, \psi_{NL}^{\rm G}(\mathbf{R}_1) \right]_{JM} + \left[\phi_{nl}^{\rm G}(\mathbf{r}_2)\, \psi_{NL}^{\rm G}(\mathbf{R}_2) \right]_{JM} + \left[\phi_{nl}^{\rm G}(\mathbf{r}_3)\, \psi_{NL}^{\rm G}(\mathbf{R}_3) \right]_{JM} \right\} . \quad (62)$$

Basis parameters employed in the converged calculation are listed in Table 4; the total number of basis functions is 885. Although the wave function space is truncated, all angular momentum components of the interaction are fully taken into account in our variational method. Converged energies are given in Table 5. The result of the present calculation agrees well with that of the Faddeev-method calculation.

In order to compare the two-body correlations in the trimer with those in the dimer, we calculated the

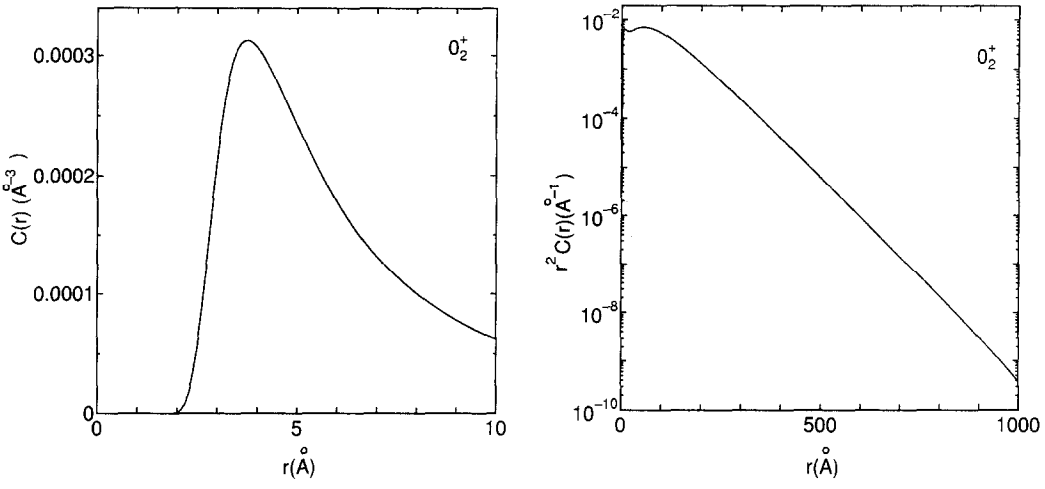

Figure 14: Two-body correlation function $C(r)$ of (63) for the excited state (0_2^+) of ^{4}He trimer obtained by GEM, left pannel for the short-range correlations and right pannel for the tail which deviates from the exponential for $r > 800$ fm.

two-body correlation function (two-body density)

$$C(r) = < \Psi_{J=0} | \delta(\mathbf{r} - \mathbf{r}_{12}) | \Psi_{J=0} > \tag{63}$$

for the ground state (0_1^+) and the excited state (0_2^+). Here $\mathbf{r}_{12}$ is the distance between particle 1 and 2. The r.m.s. distance between the pair is calculated to be 11.3 Å and 116.5 Å for the ground and excited states, respectively. $C(r)$ is shown in Figs. 13 and 14 for the ground and excited states, respectively. It is reasonable that almost the same shape of the strong short-range correlations is seen in the ground and excited states as in the case of the dimer (Fig. 3 for the *wave function*). Size of the excited state is similar to that of the dimer, but the ground state shrinks by one order in size compared with the dimer. Superposition of the Gaussian basis functions through the diagonalization of the Hamiltonian results in reasonable shape of the tail out to $\sim$ 80 fm in the ground state and $\sim$ 800 fm in the excited state. This behavior is not unexpected from our experiences in three-body calculations.

In conclusion, this tough three-body problem in the presence of a very strong repulsive core has been solved very accurately by GEM for both the compactly bound ground state and the loosely bound excited state without assuming any *ad hoc* two-body correlation function.

3.2 Test for the three-nucleon bound states (^{3}H and ^{3}He)

One of the best tests of three-body calculational method is to solve three-nucleon bound states (^{3}H and ^{3}He) using a realistic NN force. This test was done for GEM in Ref. [6] using the AV14 force [63] and in Ref.[7] using the AV14 force plus the Tucson-Melborne (TM) three-body force [64]. We shortly review them here.

The total wave function may be written as the sum of three component functions, one for each rearrangement channel of Fig. 12

$$\Psi_{JM,TT_z} = \Phi_{JM,TT_z}(\mathbf{r}_1, \mathbf{R}_1) + \Phi_{JM,TT_z}(\mathbf{r}_2, \mathbf{R}_2) + \Phi_{JM,TT_z}(\mathbf{r}_3, \mathbf{R}_3) \,, \tag{64}$$

where the $\Phi_{JM,TT_z}(\mathbf{r}_i, \mathbf{R}_i)$ have the same functional form for $i = 1 - 3$. We expand each of them in the Gaussian basis functions in the three-body angular-momentum channel which is specified by

Table 6: LS coupling three-body angular-momentum space for the $1/2^+$ ground state of ^{3}H and ^{3}He. Lengths are given in units of fm.

No.	l	L	Λ	s	Σ	$n_{\max}$	$r_{\min}$	$r_{\max}$	$N_{\max}$	$R_{\min}$	$R_{\max}$
1	0	0	0	0	1/2	15	0.05	15.0	15	0.3	9.0
2	0	0	0	1	1/2	15	0.05	15.0	15	0.3	9.0
3	2	0	2	1	3/2	15	0.1	15.0	15	0.3	9.0
4	0	2	2	1	3/2	15	0.1	15.0	15	0.3	9.0
5	2	2	0	1	1/2	15	0.1	15.0	15	0.3	9.0
6	2	2	1	1	1/2	15	0.1	15.0	15	0.3	9.0
7	2	2	1	1	3/2	15	0.1	15.0	15	0.3	9.0
8	2	2	2	1	3/2	15	0.1	15.0	15	0.3	9.0
9	1	1	0	1	1/2	10	0.1	10.0	10	0.3	6.0
10	1	1	1	1	1/2	10	0.1	10.0	10	0.3	6.0
11	1	1	1	1	3/2	10	0.1	10.0	10	0.3	6.0
12	1	1	2	1	3/2	10	0.1	10.0	10	0.3	6.0
13	1	1	0	0	1/2	10	0.1	10.0	10	0.3	6.0
14	1	1	1	0	1/2	10	0.1	10.0	10	0.3	6.0
15	2	2	0	0	1/2	10	0.1	10.0	10	0.3	6.0
16	2	2	1	0	1/2	10	0.1	10.0	10	0.3	6.0
17	1	3	2	1	3/2	10	0.1	10.0	10	0.3	6.0
18	3	1	2	1	3/2	10	0.1	10.0	10	0.3	6.0
19	3	3	0	1	1/2	10	0.1	10.0	10	0.3	6.0
20	3	3	1	1	1/2	10	0.1	10.0	10	0.3	6.0
21	3	3	1	1	3/2	10	0.1	10.0	10	0.3	6.0
22	3	3	2	1	3/2	10	0.1	10.0	10	0.3	6.0
23	3	3	0	0	1/2	10	0.1	10.0	10	0.3	6.0
24	3	3	1	0	1/2	10	0.1	10.0	10	0.3	6.0
25	2	4	2	1	3/2	10	0.1	10.0	10	0.3	6.0
26	4	2	2	1	3/2	10	0.1	10.0	10	0.3	6.0

Table 7: Calculated binding energy and the asymptotic normalization constants C_S and C_D of ^{3}H by the present method and the Faddeev method. This table is taken from [6]

(a) Present method

number of channels	$B(^3\mathrm{H})$ (MeV)	C_S	C_D
5	7.643	1.825	0.0733
8	7.660	1.825	0.0735
10	7.674	1.826	0.0737
12	7.678	1.827	0.0739
14	7.6818	1.828	0.0741
16	7.6820	1.827	0.0741
18	7.6836	1.827	0.0741
20	7.6840	1.827	0.0741
22	7.6843	1.827	0.0740
24	7.6843	1.827	0.0740
26	7.6844	1.827	0.0740

(b) Faddeev method

number of channels	$B(^3\mathrm{H})$ (MeV)	C_S	C_D
Ref. [66]			
5	7.45	1.81	0.0705
18	7.58	1.82	0.0717
26	7.67	1.82	0.0730
34	7.68	1.82	0.0732
Ref. [67]			
5	7.440	1.81	0.0704
18	7.576	1.81	0.0717
26	7.658	1.81	0.0729
34	7.673	1.82	0.0731

$\alpha \equiv \{nl, NL, \Lambda, s, \Sigma, t, JM, TT_z\}$:

$$\Phi_\alpha(\mathbf{r}_i, \mathbf{R}_i) = \left[[\phi^{\mathrm{G}}_{nl}(\widehat{\mathbf{r}}_i)\psi^{\mathrm{G}}_{NL}(\widehat{\mathbf{R}}_i)]_\Lambda [\chi_s(jk)\chi_{\frac{1}{2}}(i)]_\Sigma\right]_{JM} [\eta_t(jk)\eta_{\frac{1}{2}}(i)]_{TT_z}, \tag{65}$$

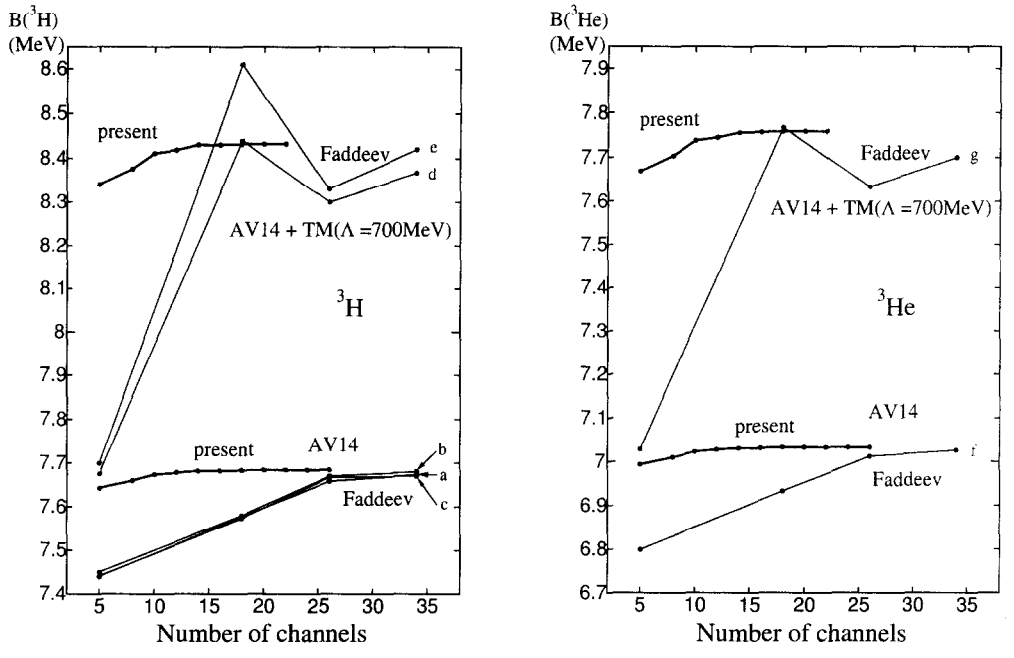

Figure 15: Convergence of the binding energies of ^{3}H and ^{3}He calculated by the present method [6, 7] and the Faddeev method with respect to the number of the three-body channels. Interactions used are AV14 (lower lines) and AV14+TM (upper lines). Ref.[65] for line c, Ref.[66] for b and e, and Ref.[67] for a, d, f, g. This figure is taken from [6, 7].

where χ and η are the spin and isospin functions, respectively. We consider here the case of $J = T = 1/2$. The particle numbers (i, j, k) are taken in cyclic permutation. The Pauli principle between particle j and k requires $l + s + t = odd$; it is easily to see that, under this condition, Ψ_{JM,TT_z} is totally antisymmetric for the exchange of any pair of particles among i, j and k. We take the LS coupling representation for the sake of simplicity in the space-coordinate transformation; the jj coupling scheme is not necessary since angular momentum truncation of the interaction is not made.
the partial-wave expansion (truncation) of the interaction is not taken in the present method. We employ the full-wave interaction.

The total wave function is then expressed in the form

$$\Psi_{JM,TT_z} = \sum_{\alpha} A_\alpha \left[\Phi_\alpha(\mathbf{r}_1, \mathbf{R}_1) + \Phi_\alpha(\mathbf{r}_2, \mathbf{R}_2) + \Phi_\alpha(\mathbf{r}_3, \mathbf{R}_3) \right]. \tag{66}$$

The coefficient A_α and the eigenenergy E are determined by the following equations derived from the Rayleigh-Ritz variational principle:

$$\langle \Phi_{\alpha'}(\mathbf{r}_1, \mathbf{R}_1) \mid H - E \mid \Psi_{JM,TT_z} \rangle = 0, \quad \text{for all} \quad \alpha'. \tag{67}$$

They lead to an eigenvalue problem of the type of Eqs.(3) and (4).

In practical calculations, we have to truncate the angular-momentum space of trial functions. In the calculation described below we restrict the orbital angular momentua to $l + L \leq 6$, which results in 26 types of the LS-coupling configurations. We refer to such configurations as channels (more precisely, three-body angular-momentum channels) similarly to the terminology the Faddeev calculations. The 26 channels employed in our calculation are listed in Table 6 together with the Gaussian parameters.

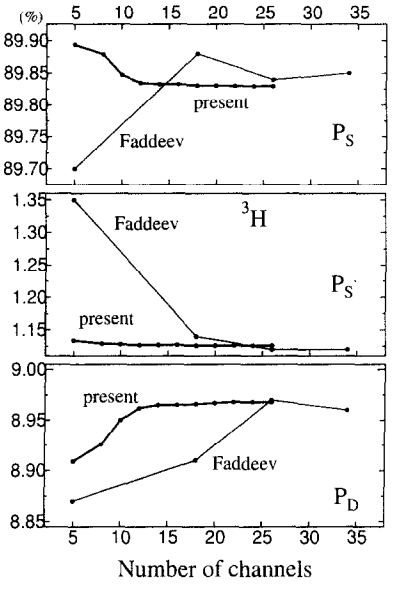

Figure 16: Convergence of the probabilities of the S, S' and D states of ^{3}H with respect to the number of the three-body channels. The AV14 potential is used. The Faddeev result is taken from Ref.[66]. This figure is taken from Ref.[6].

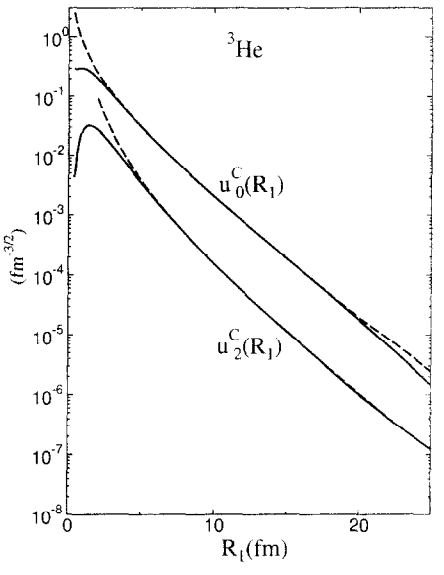

Figure 17: Deuteron–^{3}He overlap functions, $u_0^C(R_1)$ for S-state and $u_2^C(R_1)$ for D-state. The solid curves are by the 26-channel calculation. The dashed curves are the exact asymptotic functions normalized at $R_1 = 10$ fm. This figure is taken from Ref.[6].

Convergence of the binding energies and the probabilities of the S, S' and D states with respect to the number of the three-body angular-momentum channels is illustrated in Figs.15 and 16, respectively. The results were those given by GEM in Refs. [6, 7] two decades ago together with those given by the Faddeev calculations at that time. The convergence is very rapid in the GEM. Accuracy of our wave function in the asymptotic region is examined by checking the deuteron-^{3}He overlap functions, $u_0^C(R_1)$ for S-wave and $u_2^C(R_1)$ for D-wave. They are shown in the solid lines in Fig. 17, reproducing accurately the exact asymptotic functions (dashed lines) up to $\approx$ 17 fm. This wide-range agreement is enough to determine reliably the asymptotic normarization constants, C_S^C and C_D^C, which agree well with the result of the Faddeev calculation [6]. Table 7 summarizes the convergence of the binding energy and the asymptotic normarization constants with respect to the three-body angular momentum channels.

At first sight, the minimum and the maximum ranges of the Gaussians in Table 6, all round and similar numbers, might not seem a result of serious optimization. However, since the number of the basis functions is enough to give the accurate solution, slight change of parameters does not change the result in any significant way. In other words, since the computation time needed is very short we take more than enough number of basis functions and avoid serious effort to optimize the parameters. This is our rule in our variational calculations of three- and four-body problems. Stochastic treatment of the parameters might be necessary for problems involving more than four bodies as shown by the stochastic variational method in [72, 73, 74, 75].

4 Gaussian Expansion Method for Four-Body Systems: Test for $A = 4$ Nucleus

In this Section, we test the Gaussian Expansion Method (GEM) for the four-nucleon bound state. Calculation of the matrix elements between the four-body basis functions is quite analogous to the three-body case. The Four-body total wave function Ψ_{JM} is described as a sum of the components of 18 rearrangement channels (Fig. 18):

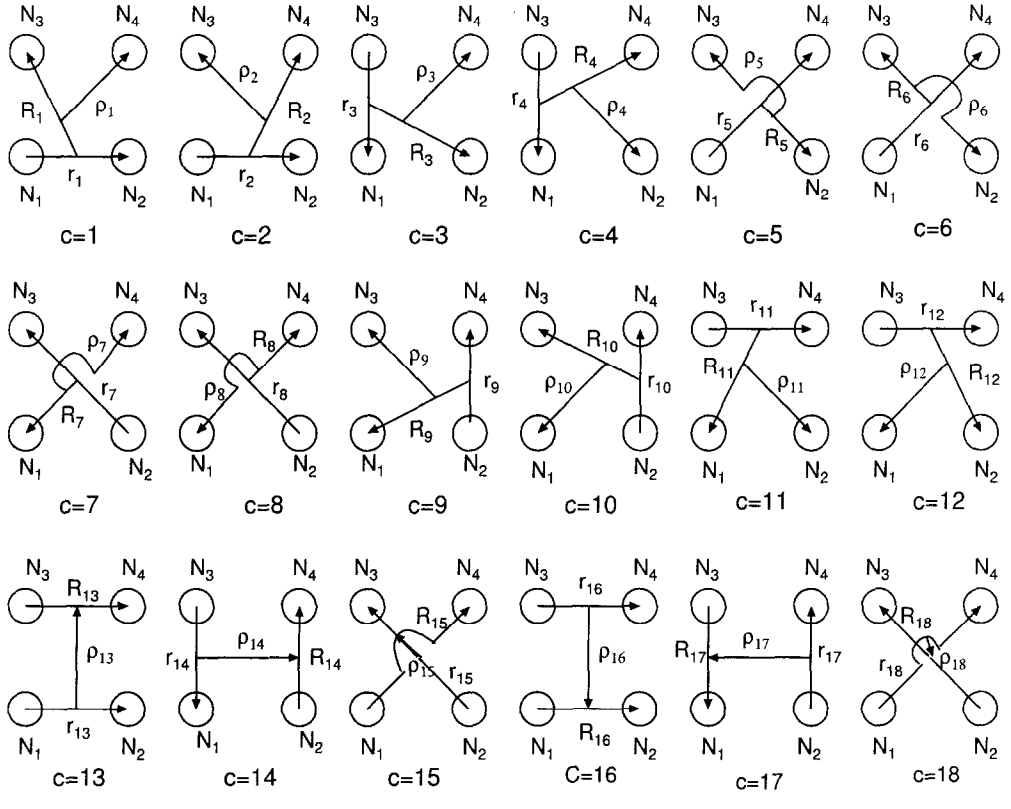

Figure 18: Jacobian coordinates for the rearrangement channel of four-body system.

$$\Psi_{JM} = \sum_{c=1}^{18} \Phi^{(c)}_{JM}(\mathbf{r}_c, \mathbf{R}_c, \boldsymbol{\rho}_c)\,. \tag{68}$$

If we omit the spin and isospin part for simplicity, each component function is expanded in terms of the Gaussian basis functions of the Jacobian coordinates $\mathbf{r}_c$, $\mathbf{R}_c$ and $\boldsymbol{\rho}_c$:

$$\Phi^{(c)}_{JM}(\mathbf{r}_c, \mathbf{R}_c, \boldsymbol{\rho}_c) = \sum_{n_c l_c, N_c L_c, I_c, \nu_c \lambda_c} A^{(c)}_{n_c l_c, N_c L_c, I_c, \nu_c \lambda_c} \left[\left[\phi^{\mathrm{G}}_{n_c l_c}(\mathbf{r}_c)\, \psi^{\mathrm{G}}_{N_c L_c}(\mathbf{R}_c) \right]_{I_c} \chi^{\mathrm{G}}_{\nu_c \lambda_c}(\boldsymbol{\rho}_c) \right]_{JM} \qquad (c = 1\text{–}18)\,, \tag{69}$$

where we take Gaussian basis functions

$$\phi^{\mathrm{G}}_{nlm}(\mathbf{r}) = \phi^{\mathrm{G}}_{nl}(r)\, Y_{lm}(\hat{\mathbf{r}}), \qquad \phi^{\mathrm{G}}_{nl}(r) = N_{nl}\, r^l\, e^{-\nu_n r^2} \qquad (n = 1 - n_{\max})\,, \tag{70}$$

$$\psi^{\mathrm{G}}_{NLM}(\mathbf{R}) = \psi^{\mathrm{G}}_{NL}(R)\, Y_{LM}(\widehat{\mathbf{R}}), \qquad \psi^{\mathrm{G}}_{NL}(R) = N_{NL}\, R^L\, e^{-\lambda_N R^2} \qquad (N = 1 - N_{\max})\,. \tag{71}$$

$$\chi^{\mathrm{G}}_{\nu\lambda\mu}(\boldsymbol{\rho}) = \chi^{\mathrm{G}}_{\nu\lambda}(\rho)\, Y_{\lambda\mu}(\hat{\boldsymbol{\rho}}), \qquad \chi^{\mathrm{G}}_{\nu\lambda}(\rho) = N_{\nu\lambda}\, \rho^{\lambda}\, e^{-\omega_\nu \rho^2} \qquad (\nu = 1 - \nu_{\max})\,. \tag{72}$$

The number and the range parameters of the Gaussians depend on l_c, L_c, λ_c and I_c but the dependence is omitted here for simplicity of notation. If some particles are identical, some channels are equivalent to each other under the antisymmetrization (symmetrization) between the particles, and therefore should have the same coefficients $A^{(c)}_{n_c l_c, N_c L_c, I_c, \nu_c \lambda_c}$ as seen in the previous section for the case of three-body systems.

In the GEM calculation of four-body matrix elements, Gaussian basis functions are replaced by the infinitesimally-shifted Gaussian basis functions:

$$\phi^{\rm G}_{nlm}(\mathbf{r}) = N_{nl} \lim_{\varepsilon\to 0} \frac{1}{(\nu\varepsilon)^l} \sum_{k=1}^{k_{\max}} C_{lm,k}\, e^{-\nu_n(\mathbf{r}-\varepsilon \mathbf{D}_{lm,k})^2}, \tag{73}$$

$$\phi^{\rm G}_{NLM}(\mathbf{R}) = N_{NL} \lim_{\varepsilon\to 0} \frac{1}{(\lambda\varepsilon)^L} \sum_{K=1}^{K_{\max}} C_{LM,K}\, e^{-\lambda_N(\mathbf{R}-\varepsilon \mathbf{D}_{LM,K})^2}, \tag{74}$$

$$\chi^{\rm G}_{\nu\lambda\mu}(\boldsymbol{\rho}) = N_{\nu\lambda} \lim_{\varepsilon\to 0} \frac{1}{(\omega_\nu\varepsilon)^\lambda} \sum_{\kappa=1}^{\kappa_{\max}} C_{\lambda\mu,\kappa}\, e^{-\omega_\nu(\boldsymbol{\rho}-\varepsilon \mathbf{D}_{\lambda\mu,\kappa})^2} \tag{75}$$

A technique for calculating the Hamiltonian matrix elements is presented in Appendix A4.

4.1 Benchmark test calculation of the ^{4}He ground state

Calculation of the four-nucleon bound state (^{4}He) using realistic NN force is useful for testing the method and the scheme of the calculation. So far, this four-nucleon problem has been solved accurately by several efficient methods, the Gaussian expansion method (GEM) [4, 6, 7, 13, 14, 15], Faddeev-Yakubovsky method (FV) [68, 69, 70, 71], the stochastic variational method (SVM) [72, 73, 74, 75], the hypersperical harmonic variational method (HH) [76, 77, 78, 79, 80], the Green's function Monte Carlo (GFMC) method [81, 82, 83, 84], the no-core shell model (NCSM) [85, 86, 87], and the effective interaction hypersperical harmonic method (EIHH) [88].

The eighteen authors of Ref. [39], including the two of the present authors (E.H. and M.K.), performed benchmark test calculations of the four-nucleon bound state of ^{4}He with the methods mentioned above using the same NN realistic force, AV8′ interaction, and compared the calculated energy eigenvalues and some wave function properties. AV′ is derived from the realistic AV18 interaction [89] by neglecting the charge dependence and the terms proportional to L^2 and $(L\cdot S)^2$. In this subsection, we briefly review the result of the benchmark test of Ref. [39].

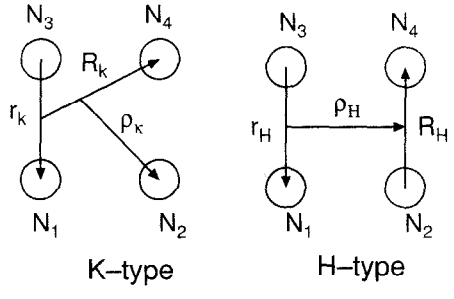

Figure 19: Jacobian coordinates for the rearrangement channel of ^{4}He. The four nucleons are antisymmetrized.

In GEM, the total four-body wavefunction is given as sum of the component functions of all the Jacobian-coordinate rearrangement channels within the LS coupling scheme (Fig. 19):

$$\Psi_{J=0} = \sum_\alpha C^{(K)}_\alpha \Phi^{(K)}_\alpha + \sum_\alpha C^{(H)}_\alpha \Phi^{(H)}_\alpha, \tag{76}$$

where the anti-symmetrized basis functions are described by

$$\Phi_\alpha^{(K)} = \mathcal{A}\left\{\left[[\phi_{nl}(\mathbf{r})\psi_{NL}(\mathbf{R})]_\Lambda\, \varphi_{\nu\lambda}(\boldsymbol{\rho})\right]_I \left[[\chi_s(12)\chi_{\frac{1}{2}}(3)]_{s'}\chi_{\frac{1}{2}}(4)\right]_S\right]_{JM} \left[[\eta_t(12)\eta_{\frac{1}{2}}(3)]_{\frac{1}{2}}\eta_{\frac{1}{2}}(4)\right]_0\Big\}\,, \quad (77)$$

$$\Phi_\alpha^{(H)} = \mathcal{A}\left\{\left[[\phi_{nl}(\mathbf{r}')\psi_{NL}(\mathbf{R}')]_\Lambda\, \varphi_{\nu\lambda}(\boldsymbol{\rho}')\right]_I \left[\chi_s(12)\chi_{s'}(34)\right]_S\right]_{JM} \left[\eta_t(12)\eta_t(34)\right]_0\Big\}\,, \quad (78)$$

with $\alpha \equiv \{nl, NL, \Lambda, \nu\lambda, I, ss'S, t\}$. We employ the K-type and H-type configurations (Fig. 19). Due to the four-nucleon antisymmetrizer $\mathcal{A}$, K-type includes $c = 1$ to 12 channels and H-type $c = 13$ to 18 channels of Fig. 18. The χ's and the η's are the spin and isospin functions, respectively. The functions $\phi_{nl}(\mathbf{r})$, $\psi_{NL}(\mathbf{R})$ and $\varphi_{\nu\lambda}(\boldsymbol{\rho})$ are taken to be the Gaussian basis functions but they are replaced by the infinitesimally-shifted ones when calculating four-body matrix elements. Gaussian ranges are taken to lie in geometrical progressions. Eigenenergies and wavefunction coefficients C_α's are determined by solving the Schrödinger equation with the Rayleigh-Ritz variational principle.

In the GEM, truncation is made not to the NN interaction but is only to the angular momentum of basis functions; this makes it possible to accomplish a quick convergence of the solution within $l, L, \lambda \leq 2$, just as in the case of three nucleon bound states discussed in Section 3.

In Table 8, we compare the calculated value of the binding energy E and the radius with those obtained by the other six methods. The good agreement for E is within 3 digits or within 0.5 %. This is quite remarkable in view of the very different techniques of calculation and the complexity of the nuclear force chosen. Also the radius is in good agreement among seven methods. Table 8 also shws the probabilities of finding three different total orbital angular momentum components in the $4N$ system. The agreement among different groups is good.

Table 8: Calculated results for ^{4}He properties by seven methods of calculation. GEM is the present method. Taken from [39](note that the GEM was referred to as CRC-GV in [39]).

Method	E (MeV)	$\sqrt{\langle r^2\rangle}$ (fm)	S (%)	P (%)	D (%)
FY	−25.94(5)	1.485(3)	85.71	0.38	13.91
GEM	−25.90	1.482	85.73	0.37	13.90
SVM	−25.92	1.486	85.72	0.368	13.91
HH	−25.90(1)	1.483	85.72	0.369	13.91
GFMC	−25.93(2)	1.490(5)			
NCSM	−25.80(20)	1.485	86.73	0.29	12.98
EIHH	−25.944(10)	1.486	85.73	0.370(1)	13.89

As a more detailed test of the calculated wavefunctions, we show the NN correlation function (two-body density)

$$C(r) = < \Psi_{J=0}|\delta(\mathbf{r} - \mathbf{r}_{12})|\Psi_{J=0} > \quad (79)$$

where $\mathbf{r}_{12}$ is the distance between particle 1 and 2. It is normalized as $4\pi \int C(r)r^2dr = 1$. The results obtained by the various calculational schemes, except GFMC, are shown in Fig. 20. The agreement among the FY, GEM, SVM, HH, and NCSM is essentially perfect.

In conclusion, the results of all schemes agree very well, showing the high accuracy of the existing methods of calculation of the four-nucleon bound state.

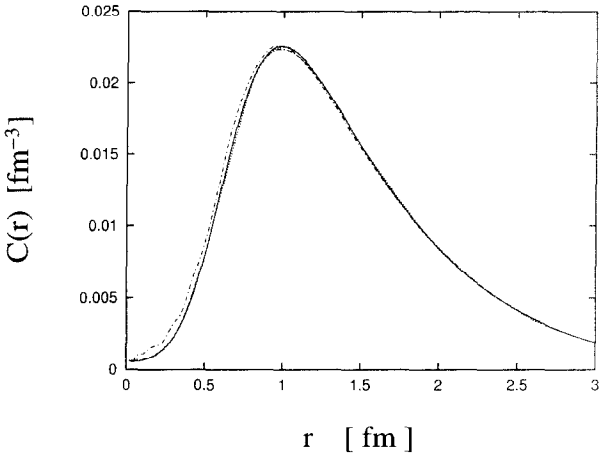

Figure 20: Correlation functions of ^{4}He in the different calculational schemes: EIHH(dashed-dotted curves), FY, GEM, SVM, HH, and NCSM(overlapping curves). Taken from [39].

4.2 The second 0^+ state of ^{4}He

^{4}He is the smallest nucleus that has discrete excited states. The second 0^+ state at $E_x = 20.2$ MeV has the same spin, isospin and parity as the ground state, and therefore must have quite different spatial structure orthogonal to that of the ground state. The can then be the smallest system to study nuclear spatial excitation using realistic interactions. Hiyama, Gibson and Kamimura [40] performed a full four-body calculation of the 0_1^+ and 0_2^+ states and the inelastic electron scattering form factor between them using GEM. Both the ground and excited 0^+ states were obtained simultaneously by the diagonalization of the Hamiltonian. The interaction employed was the AV8′ force plus the Coulomb force and a phenomenological $3N$ force which was adjusted to reproduce the binding energies of $3N$ and ^{4}He(0_1^+). We took the isospin formalism for total isospin=0 states. There were no other adjustable parameters.

The calculated energy of the second 0^+ state is $E_x(0_2^+) = 20.3$ MeV in good agreement with the observed value. One-body densities of the ground and second 0^+ states are illustrated in Fig. 21 (left). The dominant structures in the 0^+ excited-state wave function are $3N + N$ components. The size of the excited state is significantly larger than that of the compact ground state. Transition density between the two 0^+ states is shown in Fig. 21(right). Its Fourier transform with the proton size correction gives the form factor of inelastic electron scattering which agree satisfactorily well with the experimental data (see [40] for details). This is the first four-body calculation of the form factor using a realistic NN interaction.

5 Three- and Four-body study of Muonic Molecules in Muon Catalyzed Fusion Cycles

It was in the study of muonic molecules that the present coupled-rearrangement-channel Gaussian expansion method (GEM) was first proposed in 1988 by one of the authors (M.K.). The study of muonic molecules in the context of muon catalyzed fusion (μCF) (for example, see [25, 26, 28, 7, 27]) stimulated very much three-body calculational methods in nuclear and atomic/molecular physics and quantum chemistry in the 1980s. In this Section, we briefly review μCF and the application of the

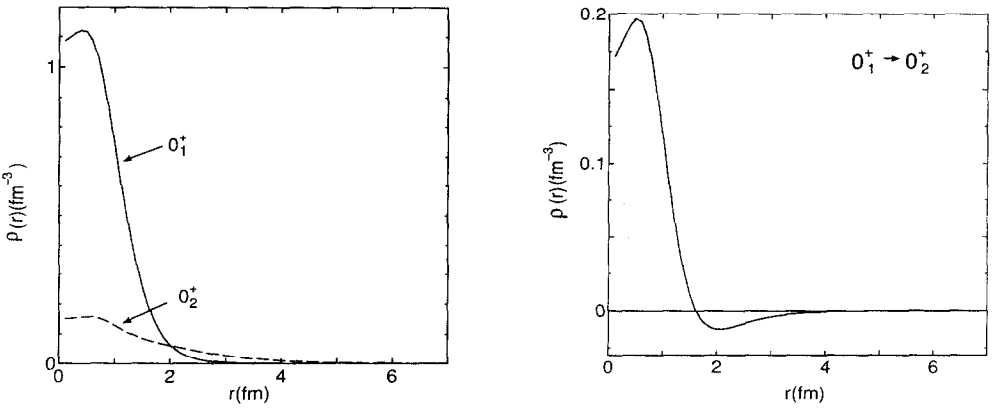

Figure 21: One-body densities of the 0_1^+ and 0_2^+ states of ^{4}He (left) and transition desity between the states (right).

present method to it.

Muon catalyzed fusion

In the last three decades, increasing attention has been paid to μCF from the viewpoints of i) the possibility of energy production at low temperature ($< 10^3$ K) and ii) interest in physics of the processes involved in the fusion cycle. The $d+t+\mu$ system is known to be a possible source of energy production by μCF. Main cycle of the μCF in the D_2/T_2 mixture is as follows (Fig. 22): Muons are first produced by the decay of pions which are generated in collision of intermediate-energy protons and target nuclei. The muon injected into the D_2/T_2 liquid or gas is immediately ($\sim 10^{-11}$ s) captured by the deuteron or triton nucleus to form $(d\mu)$ or $(t\mu)$ atom. Due to the difference of the binding energies, the muon in the $(d\mu)$ atom is soon transferred to a triton. The $(t\mu)$ atom, which is electrically neutral, enters a D_2 molecule and is captured by a deuteron to form a $(dt\mu)$ molecule. In the molecule, fusion reaction $d+t \rightarrow ^4$ He$+n$ takes place immediately($\sim 10^{-12}$ s). Muon is shaken off and becomes free again. Muon continues to catalyze the fusion reaction until its life time is exhausted.

Unfortunately, with a small probability ($< 1\%$), muon is captured by the α particle to form a $(^4\text{He}\mu)$ atom (called initial muon sticking to ^{4}He) and exhausts its lifetime in the atom, although there is a probability of reactivation of the muon during the travel of the $(^4\text{He}\mu)$ atom in the D_2/T_2 mixture.

The input energy of the cycle is estimated to be ~5 GeV which is necessary to produce one muon. If N_f is the number of fusions catalyzed by one muon, since one $d-t$ fusion generates 17.6 MeV, we see that N_f ~280 is necessary to reach the scientific break-even. Experiments performed so far show that N_f increases almost linearly with the density of the D_2/T_2 mixture, reaching N_f ~150 at the density of liquid hydrogen. More extended research and development are highly desirable to increase N_f and to decrease the cost of generating muons as well as to get deeper understanding of the mechanism of the fusion cycle (see Ref.[25] for the recent status of experiments).

Theoretically, there are many interesting and important problems in the $dt\mu$ fusion cycle from the viewpoints the physics of few-body systems. For example (see Ref.[25] for details):

1) Energy levels of the $(dt\mu)$ molecule.
2) Mechanism of the formation of the $(dt\mu)$ molecule.
3) Fusion rate of the $(dt\mu)$ molecule.
4) Probability of the muon sticking to α particle in the fusion reaction.
5) Muon transfer reaction $(d\mu)+t \rightarrow (t\mu)+d$.

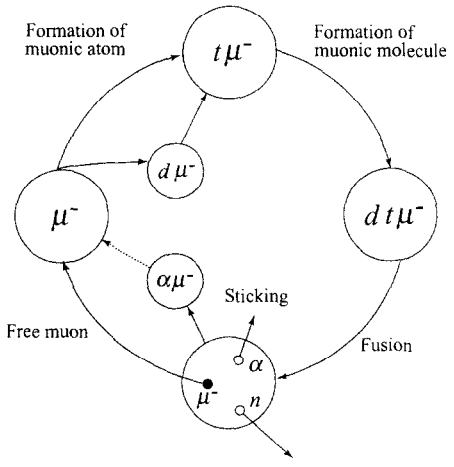

Figure 22: Main cycle of muon catalyzed $d-t$ fusion.

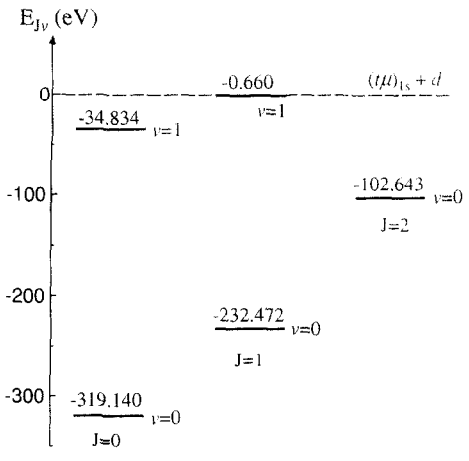

Figure 23: Theoretically predicted energy level of $dt\mu$ molecule (for example, [4]).

Various theoretical methods have been applied to the problems. The present GEM has been applied to all the five problems; the method has so wide applicability as well as high accuracy. In this Section, however, we concentrate on the problem 1) that the most strongly stimulated few-body theoreticians in 1980s. A Coulomb three-body reaction, 5), is discussed in Section 8.

Precision calculation of the energy of $J = v = 1$ level of $(dt\mu)$ molecule

In the D_2/T_2 mixture with injected muons, muonic molecules $dt\mu$ (exactly speaking, molecular ions) are resonantly formed in its $J = v = 1$ state which is very loosely bound below the $(t\mu)_{1s} + d$ threshold (Fig. 23) and is the key to the muon catalyzed fusion. In order to analyze the observed data of the molecular formation rate, accuracy of 0.001 eV is necessary in the calculated energy of the $J = v = 1$ state. Since the $(t\mu)_{1s}+d$ threshold energy is -2711 eV from the $d+t+\mu$ three-body breakup threshold, the accuracy of seven significant figures is required for the energy of the $J = v = 1$ states in the non-relativistic Coulomb three-body calculation. Note that precision calculation of the energies of other states is not difficult since they are deeply bound; many calculational methods were successful.

This difficult problem on the energy of the $J = v = 1$ state was challenged by many theoreticians in nuclear and atomic/molecular physics and chemistry. The energy below the $(t\mu)_{1s}+d$ threshold, ε_{11}, was obtained as -0.64 eV by Vinitsky *et al.* [90] (1980) and -0.656 eV by Gocheba *et al.* [91] (1985) with the adiabatic representation. Using variational method with elliptic basis, Vinitsky *et al.* [92] (1986) and Korobov *et al.* [93] (1987) gave -0.6589 eV and -0.65968 eV, respectively. Finally, -0.66001 eV was obtained by Szalewicz *et al.* [94] (1987) with Hylleraas basis, -0.66010 eV by Kamimura [4] (1988) with GEM and -0.66017 eV by Alexander *et al.* [95] (1988) with Slater geminals. Summarizing, -0.660 eV was recognized in 1988 as a reliable solution to the order of 0.001 eV.

Since the muon mass is not negligibly small compared with the nucleon mass, fully non-adiabatic calculations were necessary; this is a difference from ordinary molecules. All methods in atomic/molecular physics and in chemistry cited in the above paragraph (except GEM [4] which is from nuclear physics), suffered from the difficulty coming from this non-adiabaticity. Main trouble was the large non-orthogonality between the basis functions; the diagonalization of the energy and overlap matrices ($\sim 2000\times2000$) required quadruple-precision ($\sim$30 decimal-digit arithmetics) and the computation time of the order of 10 hours on the computers at that time.

On the other hand, GEM taken by Kamimura [4] needed only about 2 minutes for calculations of the

same size. More precisely, it took about 30 sec to calculate the $J = 1$ matrix elements of 2000×2000 and about 100 sec the eigenenergies and vectors of the 10 lowest $J = 1$ eigenstates on a FACOM VP-200 computer in 1988. This fast computation is because the use of the Gaussian basis functions which spanned over the three rearrangement channels and had the ranges in geometrical progressions sufferred little from the trouble of the linear dependence between large scale basis functions, and therefore the method works entirely in double-precision (~14 decimal-digit arithmetics) on supercomputers.

Motivation of the proposal of Gaussian expansion method (GEM)

Motivation of the proposal of the present multi-channel GEM in 1988 was as follows: The $J = v = 1$ state in the $dt\mu$ molecule is located very closely to the $(t\mu)_{1s} - d$ threshold. According to Ikeda's threshold rule [96], the state is naturally considered to be dominantly composed of a loosely coupled $(t\mu)_{1s} - d$ configuration in Channel 1. Such a configuration is difficult to describe accurately in terms of the basis functions spanned over the $(dt) - \mu$ channel ($c = 3$) only, since one would need large value of the angular momenta l_3 and L_3 associated with the coordinates $\mathbf{r}_3$ and $\mathbf{R}_3$, respectively. Therefore, for the precise description of the $J = v = 1$ state which is nearly dissociating into the $(t\mu)_{1s} - d$ two-body system, it is of particular importance to employ the Jacobian coordinate $(\mathbf{r}_1, \mathbf{R}_1)$ of the $(t\mu) - d$ channel explicitly. Furthermore, in order to conveniently describe the $d - \mu$ and $d - t$ correlations, one also needs the basis functions which span over the $(d\mu) - t$ and the $(dt) - \mu$ channels. The equal treatment of all three rearrangement channels (or three particles) is natural in the sense of nuclear physics since the muon mass is not very different from the nucleon mass. From the viewpoint of atomic/molecular physics and quantum chemistry, however, a muon is analogous to an electron and is treated separately from the nuclear motion.

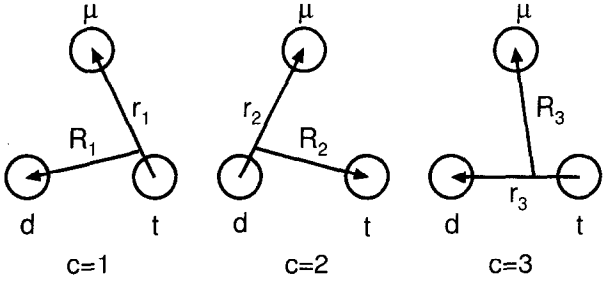

Figure 24: Three Jacobian coordinates of the $d + t + \mu$ system.

The three-body Hamiltonian is given by

$$H = -\frac{\hbar^2}{2m_c}\nabla^2_{\mathbf{r}_c} - \frac{\hbar^2}{2M_c}\nabla^2_{\mathbf{R}_c} - \frac{e^2}{r_1} - \frac{e^2}{r_2} + \frac{e^2}{r_3} \qquad (c = 1, 2 \text{ or } 3), \tag{80}$$

where m_c and M_c are the reduced masses associated with the coordinates $\mathbf{r}_c$ and $\mathbf{R}_c$, respectively. In Ref.[4], it was proposed to describe the total wave function $\Psi_{JM}(dt\mu)$ as a sum of three component functions of the coordinates of the rearrangement channels $c = 1 - 3$.

$$\Psi_{JM}(dt\mu) = \Phi^{(c=1)}_{JM}(\mathbf{r}_1, \mathbf{R}_1) + \Phi^{(c=2)}_{JM}(\mathbf{r}_2, \mathbf{R}_2) + \Phi^{(c=3)}_{JM}(\mathbf{r}_3, \mathbf{R}_3)\,. \tag{81}$$

Each component is expanded in terms of the Gaussian basis functions of the Jacobian coordinates $\mathbf{r}_c$ and $\mathbf{R}_c$:

$$\Phi^{(c)}_{JM}(\mathbf{r}_c, \mathbf{R}_c) = \sum_{n_c l_c, N_c L_c} A^{(c)}_{n_c l_c, N_c L_c} \left[\phi^{\mathrm{G}}_{n_c l_c}(\mathbf{r}_c)\, \psi^{\mathrm{G}}_{N_c L_c}(\mathbf{R}_c)\right]_{JM} \qquad (c = 1 - 3)\,. \tag{82}$$

As described in Section 6, the basis functions $\phi^{\mathrm{G}}_{nlm}(\mathbf{r})$ and $\psi^{\mathrm{G}}_{NLM}(\mathbf{R})$ are given by the Gaussian functions with the ranges in a geometrical progression. Since small values of the angular momenta l and L are

sufficient to reach a converged solution, the present method does not suffer from the over-completeness problem.

Convergence of ε_{11}, the energy of the $J = v = 1$ state, with respect to the number of the three-body basis functions is shown in Table 9. In order to discuss this sort of accuracy, the employed values of the physical constants are important; see Ref.[4] for this. Also, corrections by the relativistic effect and the finite sizes of d and t affect the energy non-negligibly; discussion of the corrections is beyond the scope of the present paper. See, for example, Ref.[25, 26] for it.

Table 9: Convergence of ε_{11}, energy of the $J = v = 1$ state of muonic molecule $dt\mu$, with respect to the number of the three-body basis functions in the GEM [4]. (Later, it was improved to -0.66017 eV with 2748 bases [97]; see Table 10).

number of basis	ε_{11} (eV) in $dt\mu$
1789	−0.660 038
1848	−0.660 048
2044	−0.660 070
2240	−0.660 084
2438	−0.660 096
2662	−0.660 104

Table 10: Three-body angular-momentum channels and Gaussian parameters for the $J = v = 1$ state of $dt\mu$ molecule. The Gaussian basis set used in the calculation of the asymptotic normalization constant C_{11} is listed. The total number of basis functions is 2748 giving $\varepsilon_{11} = -0.66017$ eV. The same parameters are taken for $c = 1$ and 2 except for the first two lines. Taken from [97].

c	l_c	L_c	$n_{\max}$	$r_{\min}$	$r_{\max}$	$N_{\max}$	$R_{\min}$	$R_{\max}$
1	0	1	21	0.006	12.0	40	0.8	550.0
2	0	1	21	0.006	12.0	18	0.8	28.0
3	0	1	10	0.4	6.0	10	0.4	6.0
1,2	1	0	15	0.2	4.0	14	1.2	18.0
3	1	0	9	0.4	6.0	8	0.4	6.0
1,2	1	2	10	0.2	4.0	9	1.2	16.0
3	1	2	8	0.4	6.0	8	0.4	6.0
1,2	2	1	9	0.2	4.0	9	1.2	12.0
3	2	1	8	0.4	6.0	7	0.4	6.0
1,2	2	3	9	0.2	4.0	9	1.2	12.0
3	2	3	7	0.4	6.0	7	0.4	6.0
1,2	3	2	9	0.4	4.0	8	1.2	12.0
3	3	2	7	0.4	6.0	7	0.4	6.0
1,2	3	4	4	0.8	4.0	4	1.6	8.0

Asymptotic behavior of the wave function of the $J = v = 1$ state of $(dt\mu)$ molecle

The important issues of the study of the $J = v = 1$ state of $(dt\mu)$ are firstly to determine the energy ε_{11} precisely, and secondly to determine the asymptotic normalization constant of the three-body wave function of the state. The latter is required to calculated the formation rate of the $J = v = 1$ state of $(dt\mu)$ in the resonant collision of a D_2 molecule with a $(t\mu)$ atom in its ground state

$$(t\mu)_{1s} + D_2 \rightarrow (dt\mu)_{11} dee, \tag{83}$$

which is one of the key reactions in the μCF cycle.

Since this is a very peripheral process, the amplitude of the $(dt\mu)$ wave function in the asymptotic region is of great importance. In the asymptotic region, a $(dt\mu)$ molecule is separated into $(t\mu)_{1s}$ and d, and therefore the $J = v = 1$ wave function, say $\Psi^{(\mathrm{As})}_{11M}$, takes the form

$$\Psi^{(\mathrm{As})}_{11M}(dt\mu) = C_{11} u^{(\mathrm{As})}_{11}(R_1)\, Y_{1M}(\widehat{\mathbf{R}}_1)\, \phi^{(t\mu)}_{1s}(\mathbf{r}_1)\,, \qquad u^{(\mathrm{As})}_{11}(R_1) = \frac{(1+\kappa R_1)}{\sqrt{2\kappa} R_1^2} e^{-\kappa R_1}\,, \tag{84}$$

where $\kappa = \sqrt{2M_1|\varepsilon_{11}|}/\hbar$ with M_1 the reduced mass of the $t\mu$ and d. C_{11} is the asymptotic normalization constant. On the other hand, the asymptotic behavior of $\Psi_{11M}(dt\mu)$ is given by the $(t\mu)_{1s} - (dt\mu)_{11}$ overlap function, $u_{11}(R_1)$, as

$$u_{11}(R_1) = \langle Y_{1M}(\widehat{\mathbf{R}}_1)\, \phi^{(t\mu)}_{1s}(\mathbf{r}_1) \,|\Psi_{11M}(dt\mu)\rangle_{\mathbf{r}_1, \widehat{\mathbf{R}}_1}\,. \tag{85}$$

In the asymptotic region, $u_{11}(R_1)$ is proportional to $u^{(\mathrm{As})}_{11}(R_1)$ as long as $\Psi_{11M}(dt\mu)$ is accurate. The asymptotic normalization constant C_{11} is then determined by the ratio

$$C_{11} = \frac{u_{11}(R_1)}{u^{(\mathrm{As})}_{11}(R_1)} \tag{86}$$

independently of R_1 in the asymptotic region. Magnitude of C_{11} is sufficient to derive the formation rate of $(dt\mu)$ and no other information on $\Psi_{11M}(dt\mu)$ is necessary.

Paying careful attention to the asymptotic behavior of $\Psi_{11M}(dt\mu)$, we calculated C_{11} in Ref. [97]. The Gaussian basis parameters used is listed in Table 10, which gave $\varepsilon = -0.66017$ eV. Figure 25 illustrates $u_{11}(R_1)$ and $C_{11}\, u^{(\mathrm{As})}_{11}(R_1)$ with $C_{11} = 0.874$. It is striking that, in the asymptotic region, they agree with each other within 0.1 % in the interval $30 < R_1 < 140$ m.a.u. (muon atomic unit) which is sufficiently wide to determine the C_{11} value reliably. The ratio, $u_{11}(R_1)/[C_{11} u^{(\mathrm{As})}_{11}(R_1)]$ with $C_{11} = 0.874$ is shown in Fig. 26.

It had been difficult to get such degree of agreement as in the figures before our wave function was applied to the problem, because the $(dt\mu)$ wave functions in the literature had been poor in the asymptotic region. For example, Aissing *et al.* [98] obtained $C_{11} = 1.006$ using the wave function obtained in [95] which gave the same value of $\varepsilon_{11} = -0.66017$ eV as in our case, but the ratio $u_{11}(R_1)/[C_{11} u^{(\mathrm{As})}_{11}(R_1)]$ with $C_{11} = 1.006$ shown in Fig. 26 had no constant region; the strong R_1 dependence suggested a large error in their C_{11} value.

Here, we again emphasize that the success of our wave function in the asymptotic region owes to the explicit use of the three rearrangement-channel component functions in the Jacobian coordinates and the long-range Gaussian basis functions in a geometrical progression: Such basis functions have no severe linear-dependence even for long-range basis.

Prediction of double muonic molecules

One can expect a possibility of observing, for the first time, double muonic hydrogen molecules, $pp\mu\mu$, $dd\mu\mu$, $tt\mu\mu$, $pd\mu\mu$, $pt\mu\mu$ and $dt\mu\mu$ since the production of an ultra-high intensity muon beam is planned at JHF facility at KEK-JAERI. Therefore, we predicted [99] the level structure of the double muonic

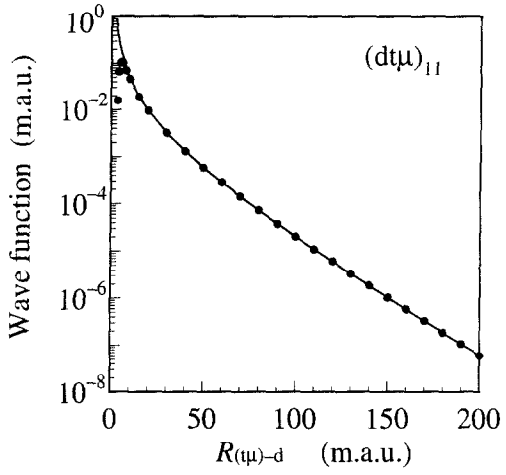

Figure 25: Asymptotic behavior of $u_{11}(R_1)$ (dotts) and $u_{11}^{(As)}(R_1)$(solid line). The latter is multiplied by $C_{11} = 0.874$. $R_1 = R_{(t\mu)-d}$ in unit of muon atomic unit. Difference is less than 0.1 % in the interval $30 < R_1 < 140$ m.a.u.. Given by [97].

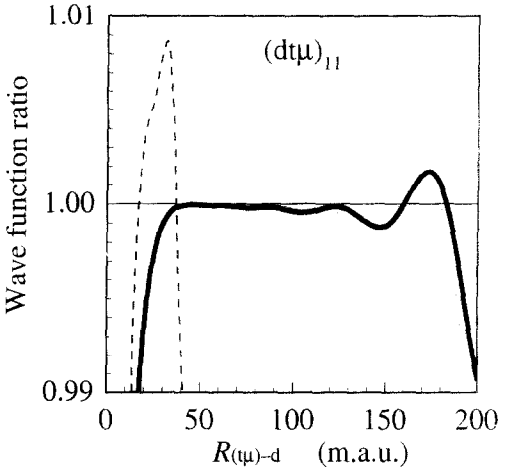

Figure 26: Asymptotic behavior of the ratio $u_{11}(R_1)/[C_{11}u_{11}^{(As)}(R_1)]$. The solid line is by [97] with $C_{11} = 0.874$ and the dashed line by [98] with $C_{11} = 1.006$. $R_1 = R_{(t\mu)-d}$ in unit of muon atomic unit.

molecules using our four-body calculational method based on infinitesimally-shifted Gaussian basis functions described in Section 2.6. The Jacobian coordinates considered are given in Fig. 27 for the $pp\mu\mu$ ($dd\mu\mu$, $tt\mu\mu$) system.

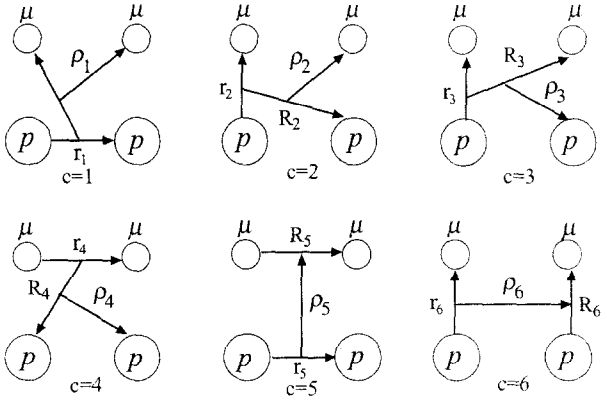

Figure 27: Jacobian coordinates of the $p+p+\mu+\mu$ system. Antisymmetrization is to be made between two protons and between two muons.

The predicted energy levels of $pp\mu\mu, dd\mu\mu$ and $tt\mu\mu$ are shown in Fig. 28. The number of the bound states are similar to the cases of single muonic hydrogen molecules, $pp\mu$, $dd\mu$ and $tt\mu$. For the same J^π, the lowest state is lower but the excited state (if exist) is higher than in the case of single muonic molecules (for example, −325.1 eV for $J = v = 0$, and −35.8 eV for $J = 0, v = 1$ in $dd\mu$). This is understandable since the adiabatic potentials between the two nuclei in the ground and the excited states are respectively lower and higher than those of the single muonic molecule due to the presence of

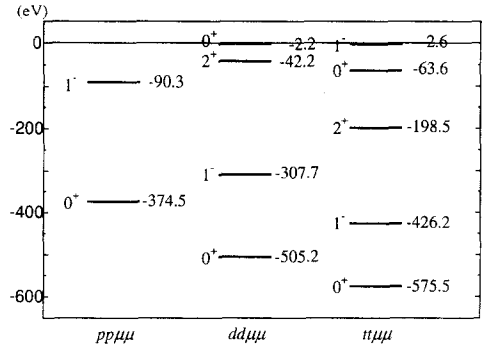

Figure 28: Predicted energy levels of double muonic molecules $pp\mu\mu, dd\mu\mu$ and $tt\mu\mu$ [99]. Energies are with respect to the threshold for $(p\mu)_{1s}+(p\mu)_{1s}$, $(d\mu)_{1s}+(d\mu)_{1s}$, $(t\mu)_{1s}+(t\mu)_{1s}$, respectively.

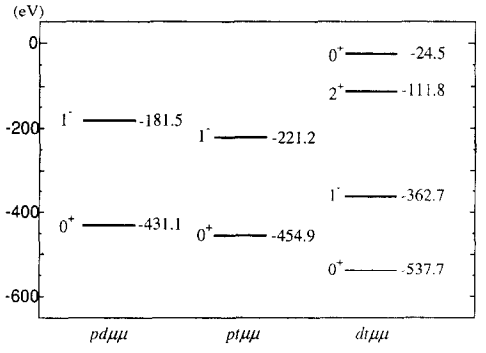

Figure 29: Predicted energy levels of double muonic molecules $pd\mu\mu, pt\mu\mu$ and $dt\mu\mu$ [99]. Energies are with respect to the threshold for $(p\mu)_{1s} + (d\mu)_{1s}$, $(p\mu)_{1s} + (t\mu)_{1s}$, $(d\mu)_{1s} + (t\mu)_{1s}$, respectively.

one more muon. Since the muon to nucleon mass ratio is not so small, non-adiabatic effect is manifest in the large isotope dependence between the three types of molecules; note that the dependence is negligible in the case of normal molecules.

In the case of $pd\mu\mu$, $pt\mu\mu$ and $dt\mu\mu$, the predicted level structure is as shown in Fig. 29. It is very similar to Fig. 28; the difference is mainly due to the nuclear mass combination. The nuclear fusion rate in the $J = v = 0$ state of $dt\mu\mu$, estimated in the same manner as in [100], and is found to be $\sim 10^{13}$ s^{-1} which is an order of magnitude larger than the rate in $dt\mu$.

6 Antiprotonic Helium Atom: Determination of Antiproton Mass

The mass of antiproton has been believed to be the same as the mass of proton, but there was no precise experimental information on it before 2000. In the 1998 edition of Particle Listings [101]. the Particle Data Group gave no recommended value of it. Instead, they only cited several scattered values obtained until that time. The reason why it is difficult to determine antiproton mass is as follows. The charge-to-mass ratio was determined very precisely, with 9×10^{-11} uncertainty [102], from the periodic motion of an antiproton in a magnetic field. Another relation between the charge and the mass is given by the energy of the X-ray from $\bar{p}$ atoms, but the experimental error is as large as 10^{-5} to 10^{-4}.

In the Particle Listings 2000 [1], a recommended value of the antiproton mass was given for the first time; the relative deviation of the antiproton mass from the proton mass was within 5×10^{-7}, which could be used for a test of CPT invariance. The 2002 edition [8] reported an order of magnitude smaller value of upper limit, 6×10^{-8}. These values were provided by a collaboration of theory and experiment on the antiprotonic helium atoms ($\bar{p}\mathrm{He}^+ \equiv \mathrm{He}^{2+} + e^- + \bar{p}$), namely the precision three-body calculation by Kino. Kamimura and Kudo [31, 3, 32, 10] and the high-resolution laser spectroscopy experiment at CERN by Torii *et al.* [2] and by Hori *et al.* [9].

In this section, we review the calculation using the Gaussian basis functions for antiprotonic helium atoms, a Coulomb three-body system. Difficult but important issues in this problem are as follows:

i) This is a Coulomb three-body problem of a heavy-heavy-light system.
ii) The total angular momentum quantum number concerned is as high as $J \sim 30 - 40$.

iii) The excited states concerned are not true bound states but so-called Feshbach resonances.
iv) The inter-nuclear motion between the helium nucleus ($Z = +2$) and the antiproton ($Z = -1$) can not be treated adiabatically when they are close to each other.
v) The correlation between the electron and the antiproton must be accurately taken into account.
vi) Accuracy of eight significant figures in the transition energy (ten digits in eigenenergy) is required to compare with the laser experiment of the transition frequency.

All of i) through vi) are difficult, but the calculation by Kino *et al.* [3, 10, 31, 32] using the Gaussian Expansion Method (GEM) has cleared all and made it possible to determine the latest value of the antiproton mass mentioned above.

6.1 Antiprotonic helium atoms

Antiprotons injected into matter annihilate within a picosecond. It was therefore surprising that much delayed annihilation was observed at KEK in 1991 [103]; about 3 % of antiprotons injected into the helium target survived as long as a few microseconds. This phenomenon was soon understood due to be production of metastable states of antiprotonic helium atom. This exotic atom can be obtained by replacing one of the electrons in a helium atom by an antiproton. The principal quantum number n of the antiproton orbit is estimated to be $n \approx 38$, highly excited states. About 3 % of the injected antiprotons are caught in one of the nearly circular orbitals ($l = n - 1$) with $n \approx 38$.

Strong absorption takes place when the antiproton is in an s-state. Generally, the deexcitation processes of an atom are the Auger decay (or auto-ionization), radioactive decay, and the Stark mixing. But, the Stark mixing is prohibited in $\bar{p}\mathrm{He}^+$ because a strong antiproton-electron correlation removes the degeneracy of angular momentum states. The radioactive lifetimes of the excited states are in the order of microsecond, because transition energies are a few eV. The lifetime of Auger decay is shorter than several nanoseconds for the lower angular momentum states of the antiproton.

In the vicinity of circular states where the angular momentum quantum number is the maximum value ($L_{\bar{p}} = n - 1$), the Auger transitions are much suppressed, because the Auger electron needs a large angular momentum gap ($\Delta l_e \geq 4$). Thus, $\bar{p}\mathrm{He}^+$ is in a metastable state which is deexcited only by a slow radiational decay. The first observation of this interesting phenomenon was made at KEK [103]. The longevity was measured over a wide range of the target density from solid to gas [104]. More than a dozen transition frequencies between metastable states of $\bar{p}\mathrm{He}^+$ were measured with fine laser spectroscopy in CERN (see Refs. [2, 9], and further references therein). Theoretical prediction by Korobov [33, 34] played a crucial role in this experiment, because the band width of the wavelength of laser was narrower than the natural width of the metastable states and the number of $\bar{p}\mathrm{He}^+$ was quite small.

The observation of long-lived antiprotonic atoms motivated spectroscopic studies from the viewpoint of the physics of antimatter: CPT(C, P, and T represent the charge conjugation, parity, and time reversal transformations, respectively) invariance, weak equivalence principle, interaction between matter and antimatter, *etc.*. In this Section, we focus on uncertainty in the determination of the antiproton mass. The symmetry of the proton and antiproton mass is related to the CPT invariance.

6.2 Method of calculation for $\bar{p}\mathrm{He}^+$

In order to solve this three-body system precisely, we employ GEM which is suitable for describing the different types of channels simultaneously and treating the electron-antiproton correlation.
The three-body total wave function Ψ_{JM} is described as a sum of three components of rearrangement channels $c = 1 - 3$ (Fig. 30).

$$\Psi_{JM} = \Phi_{JM}^{(c=1)}(\mathbf{r}_1, \mathbf{R}) + \Phi_{JM}^{(c=2)}(\mathbf{r}_2, \mathbf{R}) + \Phi_{JM}^{(c=3)}(\mathbf{r}_3, \mathbf{R}) \,. \tag{87}$$

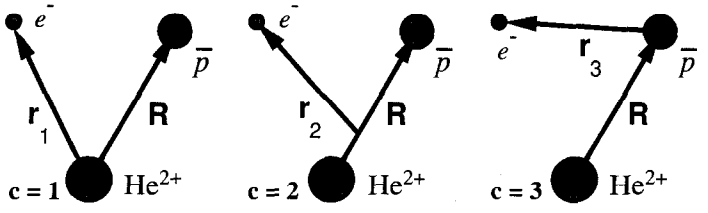

Figure 30: Three rearrangement channels (c=1, 2, and 3). Channel 1 is suitable for describing the atomic picture of the antiprotonic helium atom. Channel 2 is suitable for describing the molecular picture. Channel 3 is introduced to effectively describe the correlation between the electron and the antiproton.

Channel 1 is suitable for describing the atomic picture mentioned above. Channel 2 is for describing the molecular picture. Channel 3 is for describing the electron-antiproton correlation which plays an essential role in long lifetime of the atoms by reducing the Stark mixing.

Each amplitude $\Phi^{(c)}_{JM}(\mathbf{r}_c, \mathbf{R})$ is expanded in terms of the Gaussian basis functions of the coordinates $\mathbf{r}_c$ and $\mathbf{R}$:

$$\Phi^{(c)}_{JM}(\mathbf{r}_c, \mathbf{R}) = \sum_{n_c l_c, N_c L_c} A^{(c)}_{n_c l_c, N_c L_c} \left[\phi^{\mathrm{G}}_{n_c l_c}(\mathbf{r}_c)\, \psi^{\mathrm{G}}_{N_c L_c}(\mathbf{R})\right]_{JM} \quad (c = 1-3)\,, \tag{88}$$

$$\phi^{\mathrm{G}}_{nlm}(\mathbf{r}_c) = N_{nl}\, r^l\, e^{-\nu_n r_c^2}\, Y_{lm}(\hat{\mathbf{r}}_c) \qquad (n = 1 - n_{\max})\,, \tag{89}$$

$$\psi^{\mathrm{G}}_{NLM}(\mathbf{R}) = N_{NL}\, R^L\, e^{-\lambda_N R^2}\, Y_{LM}(\widehat{\mathbf{R}}) \qquad (N = 1 - N_{\max}). \tag{90}$$

The Gaussian ranges are chosen to lie in a geometrical progression.

$$\nu_n = 1/r_n^2\,, \qquad r_n = r_1\, a^{n-1} \qquad (n = 1 - n_{\max})\,, \tag{91}$$

$$\lambda_N = 1/R_N^2\,, \qquad R_N = R_1\, A^{N-1} \qquad (N = 1 - N_{\max}) \tag{92}$$

The number and range parameters of the Gaussians depend on l_c and L_c but the dependence is omitted here for the simplicity of notations (though given precisely in Table 12).

The Hamiltonian is written as

$$H = -\frac{\hbar^2}{2\mu_{r_c}} \nabla^2_{\mathbf{r}_c} - \frac{\hbar^2}{2\mu_R} \nabla^2_{\mathbf{R}} + T_{\mathrm{m.p.}} - \frac{2e^2}{r_1} + \frac{e^2}{r_3} - \frac{2e^2}{R} \tag{93}$$

where μ_{r_c} and μ_R are the reduced masses associated with the coordinates $\mathbf{r}_c$ and $\mathbf{R}$, respectively, and the mass-polarization term of the kinetic-energy operator, $T_{\mathrm{m.p.}}$, is given by

$$T_{\mathrm{m.p.}} = \begin{cases} \frac{-1}{m_{^4\mathrm{He}}} \nabla_{\mathbf{r}_1} \cdot \nabla_{\mathbf{R}} & (c = 1) \\ 0 & (c = 2) \\ \frac{1}{m_{\bar{p}}} \nabla_{\mathbf{r}_3} \cdot \nabla_{\mathbf{R}} & (c = 3). \end{cases} \tag{94}$$

Since the electron mass is very much smaller than the other two particles, the Jacobian coordinates were not used for Channels 1 and 3 to avoid the complexity and numerical difficulty in the rearrangement of the high-angular momentum components. But, the mass-polarization term of the kinetic-energy operator is exactly treated; this is crucial in the precision calculation.

Since the metastable states with $J \sim 30 - 40$ concerned here are the Feshbach resonances, it is desirable to treat them, for example, with the complex-coordinate-rotation (CCR) method [105] so as to take the proper boundary condition into account. The work of Ref. [10] took this method as described below, but in Refs. [3, 31, 32] the real-scaling method was employed.

The work of Refs. [3, 31, 32] examined the importance of taking the three rearrangement channels at the same time and convergence of the eigenenergy with respect to the number of basis functions. Table 11 demonstrates this; if Channels $1-3$ are employed simultaneously, the convergence of the three-body energy with respect to increasing the electron angular momentum $l_{\max}$ is much more rapid than in the case in which each channel is adopted separately.

Table 11: Convergence of the eigenenergy of $J=35, v=0$ state of $\bar{p}^4\mathrm{He}^+$ with respect to increasing $l_{\max}$ of the angular momentum of electron. The upper table is for the case in which all of Channels $1-3$ are included at the same time. The lower table is for the case in which only one of the three channels is included in the expansion. The table shows the importance of taking the three channels. Taken from [106].

$l_{\max}$	E(a.u.)	No. of Basis	Channels
0	−2.9172152652	758	$c=1$
0	− 2.9810324862	1408	$c=1+2$
0	− 2.9833722109	1976	$c=1+2+3$
1	− 2.9840208137	3810	$c=1+2+3$
2	− 2.9840209515	4962	$c=1+2+3$
3	− 2.9840209532	5929	$c=1+2+3$
4	− 2.9840209534	6279	$c=1+2+3$
5	− 2.9840209535	6851	$c=1+2+3$
6	− 2.9840209535	7175	$c=1+2+3$

$l_{\max}$	Channel 1 E(a.u.)	Channel 2 E(a.u.)	Channel 3 E(a.u.)
0	− 2.9172152652	− 2.8328020372	− 2.6704002265
1	− 2.9796718235	− 2.9802143284	− 2.8597272863
2	− 2.9828204232	− 2.9823428527	− 2.9310626650
3	− 2.9835260466	− 2.9834589475	− 2.9579340569
4	− 2.9836907910	− 2.9835786669	− 2.9656220436
5	− 2.9837150242	− 2.9836022094	− 2.9668085907
6	− 2.9837261297	− 2.9836106295	− 2.9673453010
7	− 2.9837318218	− 2.9836142809	− 2.9676155022
8	− 2.9837349872	− 2.9836160666	− 2.9677631326

In order to obtain the transition energies with the accuracy of $7-8$ significant figures, it is necessary to calculate the relativistic and QED corrections. It was precisely investigated in Refs. [3, 31, 32] using the first-order perturbation theory; the second order was found to be negligible. Here, we do not discuss the details of the calculation. We mention that although the interaction derived from the Bright-Pauli Hamiltonian includes momentum, position and spin operators and has complicated forms, the use of the Gaussian basis function enables one to calculate all of the matrix elements analytically without numerical integrals or multipole expansions.

Table 12: Three-body angular-momentum space for the $J = 35, v = 0$ state of $\bar{p}\,^4\mathrm{He}^+$ used in the calculation of Table 11. Parameters for $l \leq 2$ are listed. Lengths are given in units of Bohr radius.

c	l_c	L_c	$n_{\max}$	$r_{\min}$	$r_{\max}$	$N_{\max}$	$R_{\min}$	$R_{\max}$
1	0	35	6	0.00007	0.001	18	0.063	0.28
1	0	35	25	0.002	4.5	26	0.062	0.33
2	0	35	26	0.0003	4.5	25	0.062	0.33
3	0	35	6	0.00007	0.001	18	0.063	0.28
3	0	35	23	0.002	4.2	20	0.062	0.33
1	1	34	16	0.035	3.0	16	0.074	0.25
2	1	34	21	0.035	5.5	21	0.074	0.24
3	1	34	15	0.035	2.5	15	0.074	0.23
1	1	36	15	0.035	3.0	15	0.074	0.24
2	1	36	22	0.035	5.5	21	0.074	0.24
3	1	36	15	0.035	2.5	15	0.074	0.24
1	2	33	15	0.075	4.0	15	0.050	0.24
2	2	33	20	0.075	5.0	17	0.040	0.24
3	2	33	7	0.075	3.6	8	0.056	0.24
1	2	35	9	0.075	3.3	9	0.056	0.24
2	2	35	12	0.075	4.3	12	0.056	0.24
3	2	35	7	0.075	2.5	8	0.056	0.24
1	2	37	9	0.075	3.3	9	0.056	0.24
2	2	37	12	0.075	3.3	12	0.056	0.24
3	2	37	5	0.075	2.5	5	0.056	0.24

6.3 Calculated results

First, under the assumption that the antiproton mass $m_{\bar{p}}$ is the same as the proton mass m_p, the calculation was made of transition energies between many states. The calculated energies agreed well with those in the work by Korobov [35]. Here we pay special attention to the two transitions $(J_i, v_i) - (J_f, v_f) = (35, 3) - (34, 3)$ and $(34, 2) - (33, 2)$ since experimental data on those transitions are the most accurate, with the helium density correction taken into account. The results are summarized in Table 13 together with the experimental results. The relativistic and QED corrections reduce the discrepancy between the calculated and the observed values by about 40 ppm. The experimental data are well reproduced within the experimental error. The results show high-accuracy of the coupled-rearrangement-channel Gaussian expansion method for the Coulomb three-body systems with large angular momenta.

The wavelength was recalculated using the antiproton mass scaled with $1 + x$ against the proton mass, $m_{\bar{p}} = (1+x)m_p$. Here, the antiproton charge was scaled simultaneously to keep the charge-to-mass ratio, $e_{\bar{p}} = (1 + x)e_p$. The uncertainty of antiproton mass (charge) Δx was estimated using an uncertainty of the experimental wavelengths $\Delta\lambda_{\mathrm{exp}}$.

$$\Delta x = \frac{\Delta m_{\bar{p}}}{m_p} = \Delta\lambda_{\mathrm{exp}} \left(\frac{d\lambda}{dx}\right)^{-1}_{\mathrm{cal}} \tag{95}$$

where $(d\lambda/dx)_{\mathrm{cal}}$ was obtained from the slopes of the lines in Fig. 31. The estimated Δx in Ref. [3, 32] are listed in Table 13. In the experimental paper by Torii *et al.* [2], using discrepancies between theoretical and experimental values as $\Delta\lambda_{\mathrm{exp}}$ instead of the uncertainty of experimental values mentioned

Table 13: Calculated [3] and observed [2] transition wavelengths which are given in unit of nm. $\lambda_{\rm Coul}$ stands for pure Coulomb calculation, $\lambda_{\rm Rel}$ that with relativistic and QED corrections, $\lambda_{\rm Exp}$ experimental value. Δx is the derived uncertainty of antiproton mass.

(J_i,v_i)-(J_f,v_f)	$\lambda_{\rm Coul}$ (nm)	$\lambda_{\rm Rel}$ (nm)	$\lambda_{\rm Exp}$ (nm)	Δx
(35,3)-(34,3)	597.2290	597.2573	597.2570(3)	1×10^{-7}
(34,2)-(33,2)	470.7048	470.7220	470.7220(6)	3×10^{-7}

above, $\Delta m_{\bar{p}}/m_p < 6\times10^{-8}$ was reported and this value was cited in Particle Listings 2000 [1]. This value of $\Delta m_{\bar{p}}/m_p$ can be used for a test of the CPT invariance.

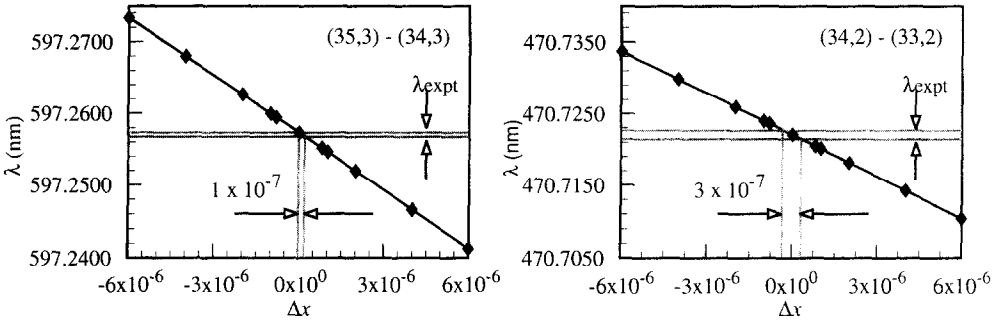

Figure 31: Calculated transition wavelengths as a function of Δx. Closed diamonds show the calculated values and the solid line is the guide for eyes. Taken from [32].

Analysis with complex-coordinate-rotation (CCR) method

The metastable states of $\bar{p}\mathrm{He}^+$ are Feshbach resonances which emit Auger electrons to decay into the bare $\bar{p}\mathrm{He}^{2+}$ atom. Therefore, in Ref. [10] the states were studies using the CCR method which is useful for calculating resonance parameters. The complex rotated Hamiltonian, wave function, and Schödinger equation are given by

$$H(\alpha,\theta) = U(\alpha,\theta)HU^{-1}(\alpha,\theta), \qquad \Psi_{vJM}(\alpha,\theta) = U(\alpha,\theta)\Psi_{vJM}, \tag{96}$$

$$H(\alpha,\theta)\Psi_{vJM}(\alpha,\theta) = E\Psi_{vJM}(\alpha,\theta). \tag{97}$$

Here, $U(\alpha,\theta)$ is a transformation operator, $\mathbf{r} \to \alpha e^{i\theta}\mathbf{r}$, α and θ being real and positive numbers.

It is known that after the complex rotation, the resonance wave function $\Psi_{vJM}(\alpha,\theta)$ becomes L^2 integrable so that the expansion in terms of the Gaussian functions can be made in the same manner as in Eqs.(87)–(92). By diagonalizing $H(\alpha,\theta)$, the eigen energy E and the expansion coefficients $A^{(c)}_{n_c l_c N_c L_c}$ are obtained as complex numbers. The resonant energy E_r and the width Γ are obtained as the real and the imaginary parts of E respectively, namely $E = E_r - \mathrm{i}\Gamma/2$. In order to obtain a converged energy, one calculates complex eigenenergy trajectories as functions of θ for different values of α. Examples of the trajectories of E on the complex E-plane are shown in Fig. 32. The position of the resonance can be determined at the converged point where $\partial E/\partial\theta$ is minimum. The numerical uncertainty of the position is estimated from the standard deviation for different values of α. It is marvelous that the present method can determine E_r and Γ so precisely.

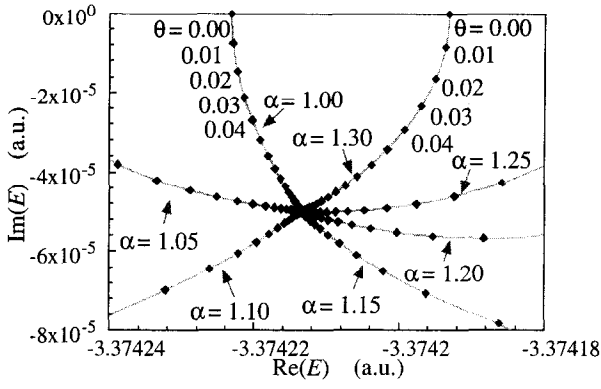

Figure 32: Complex eigenenergy trajectories for J=30, v=2 state of $\bar{p}^4\mathrm{He}^+$. The resonance is located at E_r=−3.37421343(4) a.u. and $\Gamma/2$=4.988(3)×10^{-5} a.u., where numbers in the parentheses indicate the numerical uncertainty of the last digit. Taken from [10].

In a new experiment by Hori *et al.* [9], six transition frequencies were reported as shown in the third column of Table 14. Kino *et al.* [10] calculated the frequencies of the six transitions using the CCR method assuming $m_{\bar{p}} = m_p$ and taking the relativistic and QED corrections. The results are shown in the second column of Table 14. The best agreement with the data is seen in the first two transitions which are transitions between low vibrational states. The worst agreement is for the transition (34,1)-(33,3); the discrepancy is due to a unique character of the daughter state and the helium medium effect, but we do not discuss here about it (see Ref.[10]). Observed and calculated Auger transition life time, namely $\hbar/\Gamma$, are compared with the data in Table 15. In accordance with the good agreement in the transition frequency, the decay of the state $(J, v) = (32, 1)$ is well reproduced by the calculation. The discrepancy seen in the other two lifetimes might be due to the helium medium effect (see [10]).

Table 14: Transition frequencies between metastable states of $\bar{p}\mathrm{He}^+$. The notations are theoretical values (ν_{th}) [10], experimental values (ν_{exp}) [9], discrepancies between ν_{th} and ν_{exp}, transition frequency shifts due to the scaling of antiproton mass and charge ($\nu_{\mathrm{th}}/\frac{d\nu_{\mathrm{th}}}{dx}$) and uncertainty of antiproton mass ($\frac{\Delta m_{\bar{p}}}{m_p} = (\nu_{\mathrm{th}} - \nu_{\mathrm{exp}})/\frac{d\nu_{\mathrm{th}}}{dx}$).

$(J_i, v_i) - (J_f, v_f)$	ν_{th} (GHz)	ν_{exp} (GHz)	$\frac{\nu_{\mathrm{th}}-\nu_{\mathrm{exp}}}{\nu_{\mathrm{th}}}$ (10^{-6})	$\nu_{\mathrm{th}}/\frac{d\nu_{\mathrm{th}}}{dx}$	$\frac{\Delta m_{\bar{p}}}{m_p}$ (10^{-6})
(33,1)−(32,1)	804 633.127(5)	804 633.11(11)	0.021	2.56	0.054
(32,0)−(31,0)	1 012 445.559	1 012 445.52(17)	0.039	2.45	0.094
(35,3)−(34,3)	501 948.828(8)	501 949.01(13)	−0.36	4.44	−1.6
(35,1)−(34,3)	412 885.131(8)	412 885.18(12)	−0.12	6.05	−0.72
(34,2)−(33,4)	420 121.53(1)	420 121.9(10)	−0.88	2.73	−2.4
(34,1)−(33,3)	486 104.43(7)	486 102.6(7)	3.8	3.40	13

Next, we examine the uncertainty in the determined antiproton mass by changing the antiproton mass within a range in which the calculated values are in good agreement with the experimental values. We scale the antiproton mass as well as the charge by a small fraction x, $m_{\bar{p}} = (1 + x)m_p$ and $e_{\bar{p}} = (1 + x)e_p$, which keeps the measured charge-to-mass ratio of antiproton unchanged. We recalculate transition frequencies as a function of the scaling parameter x. An example of the transition (33,1)-

Table 15: Auger decay lifetimes τ (s). Theoretical values $\tau_{\rm th}$ are given by [10].

(J,v)	$\tau_{\rm th}$ (s)	$\tau_{\rm exp}$ (s)	
(32,1)	5.45×10^{-9}	$(5 \pm 1) \times 10^{-9}$	Ref. [9]
(33,3)	2.26×10^{-11}	$(1.1 \pm 0.3) \times 10^{-11}$	Ref. [9]
(33,4)	3.25×10^{-12}	$(4.1 \pm 0.2) \times 10^{-12}$	Ref. [107]

(32,1) is shown in Fig. 33. The uncertainty of antiproton mass (or equivalently charge) is given by $\Delta m_{\bar{p}}/m_p = \Delta e_{\bar{p}}/e_p = \Delta x = (\nu_{\rm th} - \nu_{\rm exp})/\frac{d\nu_{\rm th}}{dx}$ where $\frac{d\nu_{\rm th}}{dx}$ is given by the slope of the line in Fig. 33.

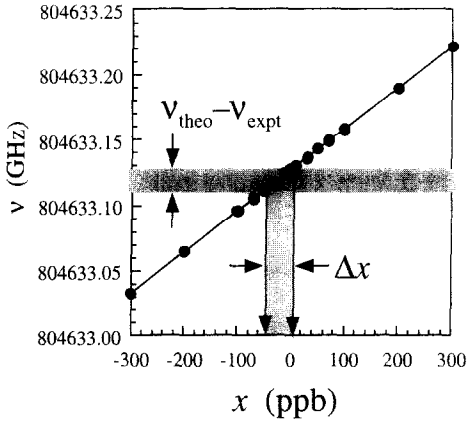

Figure 33: The calculated frequencies of the transition (33,1)-(32,1) as a function of the $\bar{p}$ mass shift parameter x. Closed circles show the calculated values and the solid line is a guide for eyes. Notations are $\Delta m_{\bar{p}}/m_p = \Delta e_{\bar{p}}/e_p = \Delta x = (\nu_{\rm th} - \nu_{\rm exp})/\frac{d\nu_{\rm th}}{dx}$

In conclusion, we obtained 5.4×10^{-8} as the best upper limit of the relative difference of the antiproton mass from the proton mass. In the experimental paper [9], based on this value but taking some more statistics, $\Delta m_{\bar{p}}/m_p < 6 \times 10^{-8}$ was reported which was cited in Particle Listings 2002 [8]. The uncertainty is by a factor of ten smaller than the previously estimated value cited in Particle Listings 2000 [1], based on the calculation in Ref. [3, 31, 32] and the experimental data [2]. This demonstrates the power of GEM.

7 Three- and Four-Body Structure of Hypernuclei

In this section, we show examples of the application of GEM to the study of the structure of hypernuclei. In the study of hypernuclear structure, there are many interesting and important subjects that can be addressed by solving the Shrödinger equations for three- and four-body systems. The present authors have investigated the structure of light Λ hypernuclei with $A = 4, 6, 7, 9$ and 13 and double Λ hypernuclei with $A = 6 \sim 10$.

One of the primary goals of hypernuclear physics is to extract information on baryon-baryon interactions. By making use of the YN scattering data and the complementary NN data, several types of YN

one-boson-exchange (OBE) potential models have been proposed within the $SU(3)$ and the $SU(6)$ framework. However, such YN and YY OBE models exhibit a great deal of ambiguity at present, since the YN scattering experiments are extremely limited and there is no YY scattering data. Therefore, it is important to obtain information on YN and YY interactions from hypernuclear structure studies.

As already mentioned in Section 1, we obtain information on YN and YY interactions by combing theory and experiment in the following way: (1) We take as candidate YN and YY interactions, the ones based on the OBE model and constituent quark model. (2) We have hypernuclear γ-ray spectroscopic data giving information on the YN and YY interactions. (3) Precision structure calculations using models of YN and YY interactions are compared with the γ-ray data to test the quality of the assumed YN and YY interactions. Such calculations allow us to improve the models so that agreement of theory and experiment may be achieved. Our calculations of few-body systems play essential roles in this procedure. As a typical example, we discuss γ-ray spectroscopy experiments and theoretical structure calculations related to the YN spin-orbit force.

Once the Hamiltonian is determined, we can calculate precisely the structure of many-body systems consisting of neutrons, protons and hyperons. Another goal of hypernuclear physics is to study the new dynamical features induced by the Λ particle. It is highly desirable to predict new phenomena and guide experiments to find them.

In this section, we review our studies performed from the above viewpoints. All the three- and four-body calculations were performed using the infinitesimally-shifted Gaussian basis functions described in Section 2.6 and Appendix.

7.1 Spin-orbit force and ${}^{9}_{\Lambda}$Be and ${}^{13}_{\Lambda}$C

In this subsection, we review our $2\alpha+\Lambda$ three-body calculation and $3\alpha+\Lambda$ four-body calculation which contributed to discriminating the OBE-model based YN spin-orbit force and the quark-model based one by predicting the spin-orbit splitting energies in hypernuclei with those forces to which experimental results were compared later. This calculation was reported in Ref. [14] and details are therein.

The reason why it is important to obtain information on YN spin-orbit force is that the antisymmetric spin-orbit (ALS) forces are qualitatively different between one-boson-exchange (OBE) models [17, 18] and quark models [19]. As a typical difference, the quark model [108] predicts that the ALS component of the ΛN interaction is so strong as to substantially cancel the LS one, while the OBE models [17, 18] propose much smaller ALS and various strength of LS. However, since there is no YN spin polarized scattering data, we have no direct experimental information on the strength of YN spin-orbit force. Therefore, careful calculations of hypernuclear structure should be of great help because Λ spin-orbit splitting in hypernuclei are directly related to the spin-orbit component of the ΛN interactions.

For this purpose, the structure study of ${}^{9}_{\Lambda}$Be and ${}^{13}_{\Lambda}$C is useful. γ-ray experiments of ${}^{9}_{\Lambda}$Be and ${}^{13}_{\Lambda}$C have been performed. In ${}^{9}_{\Lambda}$Be, one γ ray of $E_\gamma = 3.079 \pm 0.040$ MeV has been observed so far [109], but the resolution was not good enough to separate the spin-orbit doublet, suggesting only the limit $\Delta E(5/2^+_1 - 3/2^+) < 0.1$ MeV. In ${}^{13}_{\Lambda}$C, only the $1/2^+_1$ state has been observed with $E1(1/2^-_1 \to 1/2^+_1)$ transition energy $E_\gamma = 10.95 \pm 0.30$ MeV [110]. From analysis of ${}^{13}\mathrm{C}(K^-, \pi^-){}^{13}_{\Lambda}\mathrm{C}$ reaction, the p state Λ spin-orbit splitting has been suggested to be 0.36 ± 0.30 MeV [111].

Recently, two experiments with good energy resolution were performed for ${}^{9}_{\Lambda}$Be and ${}^{13}_{\Lambda}$C at BNL. One (E930 [21]) was to measure γ-rays from the decay of the $5/2^+_1$ and the $3/2^+_1$ states in ${}^{9}_{\Lambda}$Be, and the other (E929 [20]) was to measure those from the $3/2^-_1$ and $1/2^+_1$ states in ${}^{13}_{\Lambda}$C.

Before the high resolution measurements were made, it was requested to perform reliable and accurate calculations of energy splitting of the $5/2^+_1$-$3/2^+_1$ doublet in ${}^{9}_{\Lambda}$Be and the $3/2^-_1$-$1/2^-_1$ doublet in ${}^{13}_{\Lambda}$C. It was well known that the wavefunction of core nuclei, ^{8}Be and ^{12}C, are described well within the

framework of 2α and 3α microscopic models. Therefore, we performed a $2\alpha + \Lambda$ three-body calculation for ${}^{9}_{\Lambda}$Be and a $3\alpha + \Lambda$ four-body calculations for ${}^{13}_{\Lambda}$C [14].

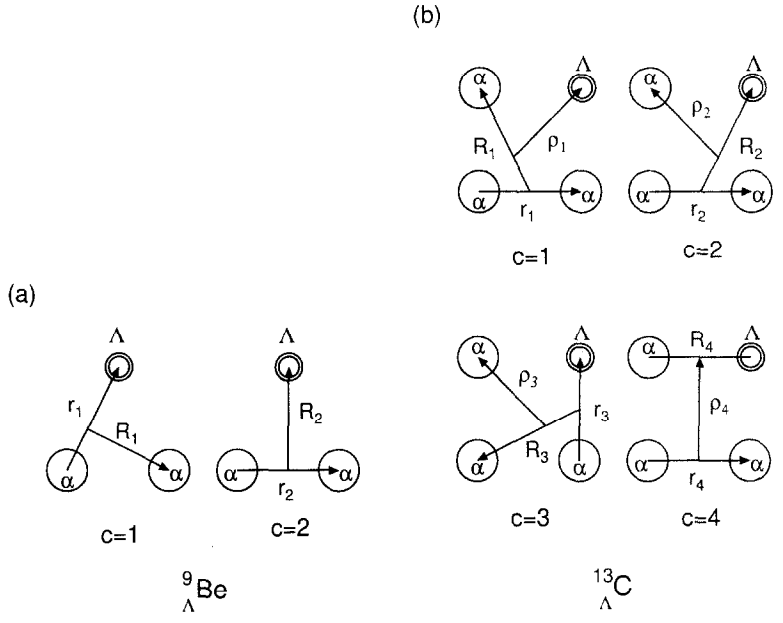

Figure 34: Jacobian coordinates of all the rearrangement channels for (a) the $2\alpha + \Lambda$ model of ${}^{9}_{\Lambda}$Be and (b) the $3\alpha + \Lambda$ model of ${}^{13}_{\Lambda}$C. The α clusters are to be symmetrized.

The employed OBE based ΛN spin-orbit force [17, 18] and the quark-model based one [19] are explained in Ref. [14]. The total wavefunction was described as a sum of components corresponding the rearrangement channels of Fig. 34 in the LS coupling scheme:

$$\Psi_{JM}({}^{9}_{\Lambda}\mathrm{Be}) = \sum_{c=1}^{2} \sum_{I} \sum_{l,L} \sum_{n,N} C^{(c)}_{nlNLI} \mathcal{S}_{\alpha} \Big[\Phi^{(\alpha_1)} \Phi^{(\alpha_2)} [\phi^{(c)}_{nl}(\mathbf{r}_c) \psi^{(c)}_{NL}(\mathbf{R}_c)]_I \chi_{\frac{1}{2}}(\Lambda) \Big]_{JM}, \tag{98}$$

$$\Psi_{JM}({}^{13}_{\Lambda}\mathrm{C}) = \sum_{c=1}^{4} \sum_{I,J_0} \sum_{l,L,\lambda} \sum_{n,N,\nu} C^{(c)}_{nlNL\nu\lambda IJ_0} \mathcal{S}_{\alpha} \Big[\Phi^{(\alpha_1)} \Phi^{(\alpha_2)} \Phi^{(\alpha_3)} [[\phi^{(c)}_{nl}(\mathbf{r}_c) \psi^{(c)}_{NL}(\mathbf{R}_c)]_I \xi^{(c)}_{\nu\lambda}(\boldsymbol{\rho}_c)]_{J_0} \chi_{\frac{1}{2}}(\Lambda) \Big]_{JM}, \tag{99}$$

where the c denote the channel shown in Fig. 34 and $\mathcal{S}_{\alpha}$ the symmetrization operator for exchange between α clusters. $\chi_{\frac{1}{2}}(\Lambda)$ is the spin function of the Λ particle. As for $\phi_{nlm}(\mathbf{r})$, $\psi_{NLM}(\mathbf{R})$ and $\xi^{(c)}_{\nu\lambda\mu}(\rho_c)$, we took the Gaussian basis functions of Section 3, but replace them with the infinitesimally-shifted Gaussian basis functions when the three- and four-body matrix elements are calculated as mentioned in Sections 3 and 4. The Gaussian ranges were taken to be in geometrical progression. Eigenenergies of the coefficients C were to be determined by the Rayleigh-Ritz variational method.

The Pauli principle between two α clusters is taken into account by the orthogonality condition model (OCM) [112]. We employed an $\alpha\alpha$ potential which reproduced the observed $\alpha\alpha$ scattering phase shifts and the resonant ground state energy of ^{8}Be within the 2α OCM. The $\alpha\alpha$ potential, $V_{\alpha\alpha}(r)$, was constructed by folding the modified Hasegawa-Nagata effective NN potential [113] and the pp Coulomb potential into the α cluster density. This $\alpha\alpha$ potential, however, gives rise to a significant over binding of the ground state of ^{12}C. We therefore introduced an effective, repulsive, 3α potential. The $\Lambda\alpha$ interaction was derived by folding the ΛN G-matrix interaction (see Ref.[14]) into the α-cluster wavefunction. Use

of the ΛN interaction and the $\alpha\alpha$ and 3α interactions reproduced the Λ binding energies of ${}^{5}_{\Lambda}$He, ${}^{9}_{\Lambda}$Be, and ${}^{13}_{\Lambda}$C ($1/2^+_1$ and $1/2^-_1$) simultaneously.

For ${}^{9}_{\Lambda}$Be, we calculated the energies of the doublet states of $5/2^+_1$ and $3/2^+_1$ whose dominant cofiguration was ${}^{8}\mathrm{Be}(2^+_1) \otimes \Lambda(s_{1/2})$. Calculated energy splitting, $\Delta E(5/2^+_1 - 3/2^+_1)$, was 80 – 200 keV depending on the Nijmegen OBE models. For ${}^{13}_{\Lambda}$C, calculated energy splitting, $\Delta E(3/2^-_1 - 1/2^-_1)$, was 390 – 960 keV depending on the Nijmegen OBE models. In these calculations, the ALS forces were more or less similar to each other, while the LS strength changed continuously over a wide range. As a consequence, the sum of LS and ALS gave rise to 20 – 40 % reduction of the splitting from that obtained with LS only.

It is interesting to note that the cancellation is known to be more drastic for the quark-model based LS and ALS forces. Use of the quark-model based ΛN spin-orbit interaction gives $\Delta E(5/2^+_1 - 3/2^+_1) = 35 - 40$ keV in ${}^{9}_{\Lambda}$Be and $\Delta E(3/2^-_1 - 1/2^-_1) = 150 - 200$ keV in ${}^{13}_{\Lambda}$C.

Table 16: Spin-orbit splitting energy in in ${}^{9}_{\Lambda}$Be and ${}^{13}_{\Lambda}$C. Calculated values are given by Hiyama *et al.* [14] using the OBE-model-based and quark-model-based ΛN spin-orbit force. Experimental values are taken from [21] for ${}^{9}_{\Lambda}$Be and from [20] for ${}^{13}_{\Lambda}$C.

	splitting	CAL(OBE model) (keV)	CAL(quark model) (keV)	EXP (keV)
${}^{9}_{\Lambda}$Be	$E(5/2^+_1 - 3/2^+_1)$	$80 - 200$	$35 - 40$	$31.4^{+2.5}_{-3.6}$
${}^{13}_{\Lambda}$C	$E(3/2^-_1 - 1/2^-_1)$	$390 - 960$	$150 - 200$	$150 \pm 54 \pm 36$

Recently, experimental data for these energy splittings of ${}^{9}_{\Lambda}$Be [21] and ${}^{13}_{\Lambda}$C [20] have been reported to be $31.4^{+2.5}_{-3.6}$ keV and $152 \pm 54 \pm 36$ keV, respectively.

The predicted values and the experimental results are summarized in Table 16. We see that the predicted energy splitting using the quark-based spin-orbit force can explain both data consistency, while any of Nijgemen models cannot. It is obvious that the analysis described above can be used to test any new YN interaction which might be proposed in the future.

7.2 The first four-body calculation of ${}^{4}_{\Lambda}$H and ${}^{4}_{\Lambda}$He, and $\Lambda - \Sigma$ conversion

Four-body calculation of ${}^{4}_{\Lambda}$H and ${}^{4}_{\Lambda}$He using NN and YN interactions are much more difficult than that of four-nucleon bound state because one has to take explicit account of the $NNN\Lambda$ and the $NNN\Sigma$ channels as well as be realistic NN and YN interactions. Historically, Gibson *et al* employed a coupled two-body model [22] of ${}^{3}\mathrm{He}({}^{3}\mathrm{H}) + \Lambda/\Sigma$ which was originally due to Dalitz and Downs [114], and later carried out four-body coupled-channel calculations with central separable potentials [23]. Carlson performed four-body calculation with the NSC89 separable potential with Monte Carlo method [115] and obtained binding energies with statical errors of 100keV. Akaishi *et al.* [24] recently analyzed the role of the $\Lambda N - \Sigma N$ coupling for the 0^+-1^+ splitting in the framework of the coupled two-body model of ${}^{3}\mathrm{He} + \Lambda/\Sigma$.

We recently succeeded in performing extensive four-body calculations without any restriction of channels. Both the $NNN\Lambda$ and $NNN\Sigma$ channels were incorporated explicitly and all the rearrangement channels of these baryons were taken into account [15]. As a results, we succeeded in analyzing the role of $\Lambda - \Sigma$ conversion in light hypernuclei which had been investigated for many years by various authors [22, 23, 24] to see its effects on the binding energies, the charge-symmetry-breaking difference, the role of ΛNN three-body force, etc.

Our main goals were, first, to solve the four-body ${}^{4}_{\Lambda}$H and ${}^{4}_{\Lambda}$He problem by taking into account explicitly the $NNN\Lambda(\Sigma)$ channels using realistic NN and YN interactions and, second, to clarify the role of the $\Lambda N - \Sigma N$ coupling in the $A = 4$ hypernuclei. As a first step, before going to sophisticated OBE models, we employed the $\Lambda N - \Sigma N$ coupled YN potential of Ref.[116] with central, spin-orbit, and tensor terms which simulates the scattering phase shifts given by NSC97f. The main reason for using the simulated version of NSC97f was its computational tractability which allowed us to focus our attention to the physical ingredients. The observed binding energy of ${}^{3}_{\Lambda}$H was reproduced reasonably well: The interaction lead to the Λ binding energy, $B_\Lambda({}^{3}_{\Lambda}\mathrm{H})$, 0.19 MeV which agreed well with the observed data $[B_\Lambda({}^{3}_{\Lambda}\mathrm{H}) = 0.13 \pm 0.05$ MeV]. For the NN interaction we employed the AV8 potential [63].

The total four-body wavefunction assumed is given as a sum of the components for all rearrangement channels ($c = 1 \sim 4$) of Fig. 35 in the LS coupling scheme:

$$\Psi_{JM}({}^{4}_{\Lambda}\mathrm{He},{}^{4}_{\Lambda}\mathrm{H}) = \sum_{Y=\Lambda,\Sigma}\sum_{c=1}^{4}\sum_{\alpha I}\sum_{ss'Stt'} C^{(c)}_{\alpha I s s' S t t'}\mathcal{A}\left\{\left[\Phi^{(Y,c)}_{\alpha I}(\mathbf{r}_c,\mathbf{R}_c,\boldsymbol{\rho}_c)\,[[\chi_{s'}(12)\chi_{\frac{1}{2}}(3)]_s\chi_{\frac{1}{2}}(Y)]_S\right]_{JM}\right.$$
$$\left.\times[[\eta_{t'}(12)\eta_{\frac{1}{2}}(3)]_t\eta_{t_Y}(Y)]_{T=\frac{1}{2}}\right\}, \tag{100}$$

where the spatial wave functions have the form, with a set of quantum numbers $\alpha = \{nl, NL, K, \nu\lambda\}$,

$$\Phi_{\alpha IM}(\mathbf{r},\mathbf{R},\boldsymbol{\rho}) = \left[[\phi_{nl}(\mathbf{r})\psi_{NL}(\mathbf{R})]_K\xi_{\nu\lambda}(\boldsymbol{\rho})\right]_{IM}. \tag{101}$$

Here, $\mathcal{A}$ is the three-nucleon antisymmetrization operator and the χ's and the η's are the spin and isospin functions, respectively, with the isospin $t_Y = 0\,(1)$ for $Y = \Lambda\,(\Sigma)$. The $\phi_{nlm}(\mathbf{r})$ were taken to be the Gaussian basis functions, but, in actual calculation of the four-body matrix elements, they were replaced by the infinitesimally-shifted Gaussian basis functions as done in Section 4 and Appendix. The Gaussian range parameters were chosen to lie in geometrical progressions as in Section 2.1. Eigenenergies of the Hamiltonian and the coefficients C were determined by the Rayleigh-Ritz variational method. The angular momentum space of $l, L, \lambda \leq 2$ was found to be sufficient to get a good convergence of the calculated results as described below.

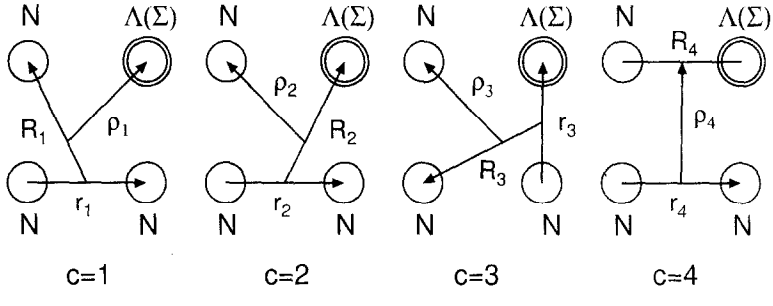

Figure 35: Jacobian coordinates for the rearrangement channels of the $NNN\Lambda(\Sigma)$ system. The three nucleons are to be antisymmetrized.

The calculations were performed for ${}^{4}_{\Lambda}$He and ${}^{4}_{\Lambda}$H. Calculated B_Λ of the 0^+ ground state and the 1^+ excited state of ${}^{4}_{\Lambda}$He and ${}^{4}_{\Lambda}$H are illustrated in Fig. 36 in comparison with the observed values. Both states are unbound. The $NNN\Sigma$ sector is divided into the $(NNN)_{1/2}\Sigma$ and $(NNN)_{3/2}\Sigma$ channels in which three nucleons are coupled to isospin $t = 1/2$ and $3/2$, respectively. When the $(NNN)_{1/2}\Sigma$ channel is included, the 0^+ state becomes bound, but the 1^+ state is still unbound. The 1^+ state becomes bound only when the $(NNN)_{3/2}\Sigma$ channel is switched on. However, the binding energy of the 0^+ state increases only slightly with the $t = 3/2$ channel.

Thus, the Σ-channel components turn out to play an essential role in the binding mechanism of the $A = 4$ hypernuclei, the $(NNN)_{3/2}\Sigma$ channel being particularly important in the 1^+ state. The calculated

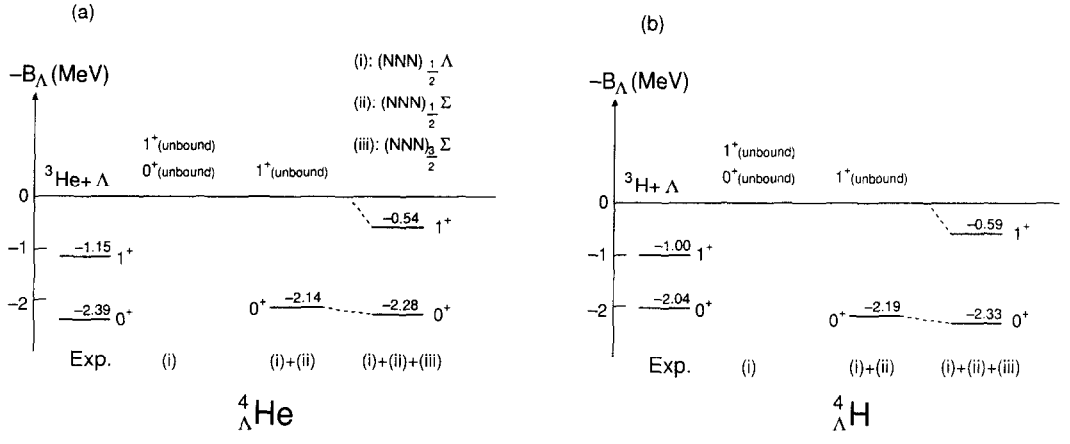

Figure 36: Calculated energy levels of (a) $^4_\Lambda$He and (b) $^4_\Lambda$H. The channels successively included are (i) $(NNN)_{1/2}\Lambda$, (ii) $(NNN)_{1/2}\Sigma$, and (iii) $(NNN)_{3/2}\Sigma$, where the isospin of the three nucleons is coupled to $t = 1/2$ or $3/2$. Energy is measured from the ^{3}He + Λ(^{3}H + Λ) threshold.

binding energy of the 0^+ state almost reproduces the observed binding energy, while the 1^+ state is less bound by 0.6 (0.4) MeV for $^4_\Lambda$H ($^4_\Lambda$H), and hence the 0^+-1^+ splitting is larger than the observed splitting. The calculated value of $B_\Lambda(^4_\Lambda\mathrm{He}(0^+)) - B_\Lambda(^4_\Lambda\mathrm{H}(0^+)) = -0.05$ MeV is different from the experimental one, +0.35 MeV, although the Coulomb potentials between charged particles ($p, \Sigma^\pm$) are included. This difference should be attributed to the charge-symmetry-breaking component which is not included in our adopted YN interaction.

As listed in Table 17, the calculated probabilities of the $NNN\Sigma$-channel admixture are 2% and 1% for the 0^+ and 1^+ states in $^4_\Lambda$He, respectively. In the 0^+ state, the probability of the $(NNN)_{\frac{1}{2}}\Sigma$ channel is much larger than that of the $(NNN)_{\frac{3}{2}}\Sigma$ channel, while in the 1^+ state they are nearly the same. We therefore confirm that the $(NNN)_{\frac{3}{2}}\Sigma$ channel is particularly important in the 1^+ state. The S-, P- and D-state probabilities of the channels are also listed in Table 17. It is remarkable that, in the $NNN\Sigma$ channel, the D-state component is dominant both in the 0^+ and 1^+ states, since the ΛN-ΣN coupling part of the present interaction is dominated by the tensor component. These properties are quite similar in the case of $^4_\Lambda$H.

Table 17: The probabilities (%) of the S-, P- and D-state and their total for each of the $(NNN)_{\frac{1}{2}}\Lambda$, $(NNN)_{\frac{1}{2}}\Sigma$ and $(NNN)_{\frac{3}{2}}\Sigma$ channels in the 0^+ and 1^+ states of $^4_\Lambda$He. $(NNN)_t$ denotes three nucleons whose isospins are coupled to t. This table is taken from [15]

$^4_\Lambda$He	0^+				1^+			
	S	P	D	Total	S	P	D	Total
$(NNN)_{\frac{1}{2}}\Lambda$	89.32	0.08	8.52	97.92	90.38	0.07	8.52	98.97
$(NNN)_{\frac{1}{2}}\Sigma$	0.84	0.04	1.16	2.04	0.10	0.01	0.40	0.51
$(NNN)_{\frac{3}{2}}\Sigma$	0.01	0.01	0.02	0.04	0.09	0.00	0.43	0.52

It is interesting to explore the spatial distributions of the N, Λ and Σ in the $A = 4$ hypernuclei. We calculated the correlation functions (two-body densities) of the NN, ΛN and ΣN pairs in Fig. 37, and

the one-body densities of single nucleons, Λ and Σ hyperons in Fig. 38. The NN correlation function in ${}^{4}_{\Lambda}$He exhibits almost the same shape as that in the ^{3}He nucleus, indicating that the dynamical change due to the presence of Λ is small. The ΛN correlation function has a long range and is flatter than the NN one, because the ΛN interaction is significantly weaker than the NN interaction. The ΣN correlation function is much shorter ranged than the ΛN one due to the large virtual excitation energy (80 MeV) of $\Lambda \to \Sigma$. It is interesting to note in Fig. 37 that, in spite of the small probability of the Σ admixture (2 %), the ΣN components is not so small at short distances in comparison with the ΛN one. This enhanced short-range distribution of the Σ is expected to be reflected in the nonmesonic decay of $\Sigma N \to NN$.

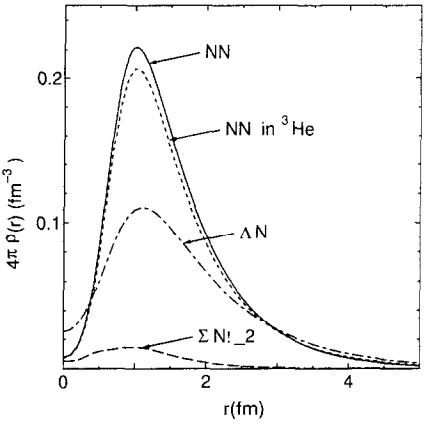

Figure 37: Correlation function (two-body densities) of $NN, \Lambda N$ and ΣN pairs in the 0^+ state of ${}^{4}_{\Lambda}$He together with that for the NN pair in ^{3}He. That of the ΣN pair has been multiplied by a factor of 2 to make the behavior of this function clear. The r.m.s. radius of each density is $\bar{r}_{NN} = 2.86$ fm, $\bar{r}_{\Lambda N} = 3.77$ fm and $\bar{r}_{\Sigma N} = 2.24$ fm. This figure is taken from [15].

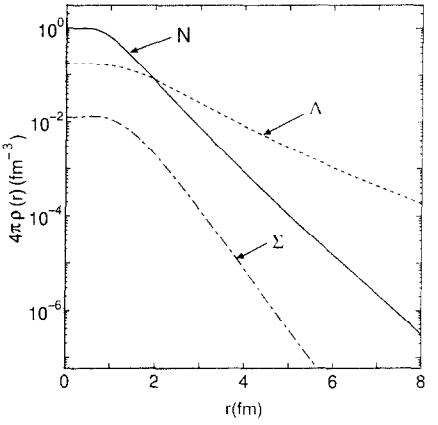

Figure 38: Calculated one-body densities of N, Λ and Σ particles in the 0^+ state of ${}^{4}_{\Lambda}$He. Volume integrals of the densities are 1.0, 0.98 and 0.02 for N, Λ and Σ particles, respectively. The r.m.s. radius of each density is $\bar{r}_N = 1.65$ fm, $\bar{r}_\Lambda = 3.39$ fm and $\bar{r}_\Sigma = 1.67$ fm. This figure is taken from [15].

In order to illustrate the effect of the Σ mixing in more detail, we separate the contribution of $\Lambda N - \Sigma N$ coupling into the two processes illustrated in Fig. 39. The first one is the process (i) which can be renormalized into the effective ΛN two-body force and the second one is the process (ii) which can be represented by the effective ΛNN three-body force acting in the $NNN\Lambda$ space. We solve the Schrödinger equation by excluding the three-body process (ii) so as to evaluate the contribution of process (i) alone and then including both (i) and (ii). As shown in Fig. 39, process (i) is large enough to make both the 0^+ and 1^+ states bound. The contribution of the three-body process (ii) is also substantial, viz. an additional attraction of 0.62(0.62) MeV in the 0^+ state and a repulsion of 0.09 (0.08) MeV in the 1^+ state of ${}^{4}_{\Lambda}$He(${}^{4}_{\Lambda}$H).

Thus, we have developed a method of calculation for bound-state problems capable of precise four-body calculations of ${}^{4}_{\Lambda}$H and ${}^{4}_{\Lambda}$He, taking both the $NNN\Lambda$ and $NNN\Sigma$ channels explicitly into account and using realistic NN and YN interactions. As a result, we have succeeded in clarifying the role of $\Lambda - \Sigma$ conversion and quantitatively estimating the size of the Σ mixing in the $A = 4$ hypernuclei. Recently, Nogga *et al.* [117] performed four-body Faddeev-Yakubovsky calculation of ${}^{4}_{\Lambda}$He and ${}^{4}_{\Lambda}$H using modern realistic NN and YN interactions. They claimed that none of the YN interactions available so far were adequate for reproducing the binding energies of 0^+ and 1^+ states, although the ground state energy of ${}^{3}_{\Lambda}$H was in good agreement with the experimental data. It is left as a future problem to explore the

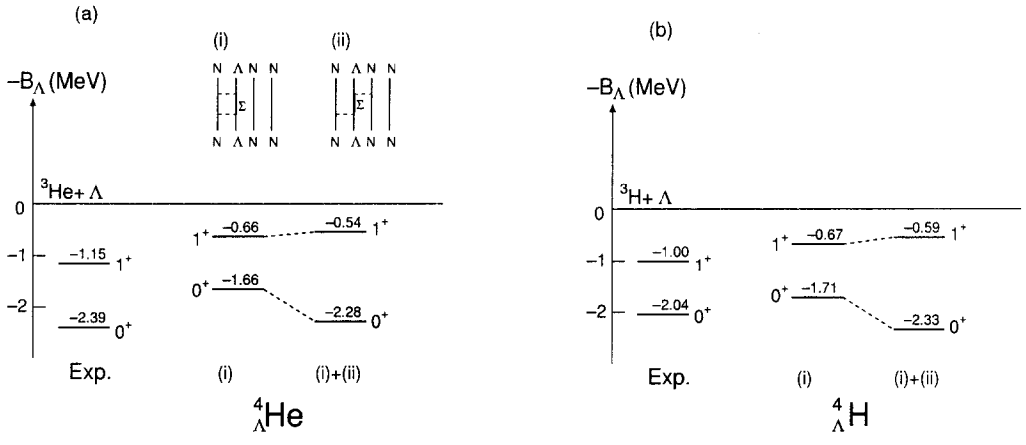

Figure 39: Calculated energy levels of (a) $^4_\Lambda$He and (b) $^4_\Lambda$H for case (i) and case (i)+(ii); here, (i) denotes the two-body process and (ii) denotes the three-body process. This figure is taken from [15].

features of $\Lambda - \Sigma$ conversion in Λ hypernuclei using more refined YN interactions and to carry out systematic studies of the structure of heavier hypernuclear systems.

7.3 Novel dynamical properties of hypernuclei

As described in the previous subsection, we can extract novel information on YN interactions by means of highly accurate structure calculations. Once the Hamiltonian is given, we can calculate precisely the structure of many-body systems consisting of neutrons, protons and hyperons. Another purpose of hypernuclear physics is to study the new dynamical features induced by the Λ particle. It is very desirable to predict new phenomena and guide experiments to find them.

Nuclear shrinkage in $^7_\Lambda$Li

It has long been thought that the nucleus cannot be significantly compressed. How is the structure of a nucleus modified when a Λ particle is injected into it? There is no Pauli Principle acting between the Λ and the nucleons in the nucleus. Therefore, the Λ particle can reach deep inside, and attract the surrounding nucleons towards the interior of the nucleus (this is called "gluelike role" of Λ particle). However, how do we observe the shrinkage of the nuclear size by the Λ participation? In the work of Ref. [118] based on the microscopic $\alpha + x + \Lambda$ three-cluster model ($x = d, t, ^3$He) for light p-shell hypernuclei together with the $\alpha + x$ two-cluster model for the nuclear core, the reduction of the nuclear size was recognized in the reduction of the $B(E2)$ strength which is proportional to the fourth power of the distance between the α and x clusters.

More precisely, in Ref.[13], we suggested the measurement of $B(E2; 5/2^+_1 \to 1/2^+_1)$ in $^7_\Lambda$Li and proposed a prescription to derive hypernuclear size for the first time with the aid of the empirical values of $B(E2; 3^+_1 \to 1^+_1)$ and the size of the ground state of ^{6}Li. Afterwards, the experiment of Ref.[119] was performed and the result was compared with our prediction on the size of $^7_\Lambda$Li.
We employed a microscopic $^5_\Lambda\text{He} + n + p$ three-body model for $^7_\Lambda$Li. It was examined in Ref. [13] that the $^5_\Lambda$He is a good cluster. The total three-body wave function is constructed on the Jacobian coordinates of Fig. 40 in the same manner as in the three-body calculations in the previous sections. Interactions employed are described in Ref.[13].

The observed energies of the $1/2^+_1$ and $5/2^+_1$ were well reproduced by the calculations, and the value $B(E2; 5/2^+_1 \to 1/2^+_1) = 2.42\, e^2\text{fm}^4$ was predicted. This is much smaller than the observed $B(E2; 3^+_1 \to$

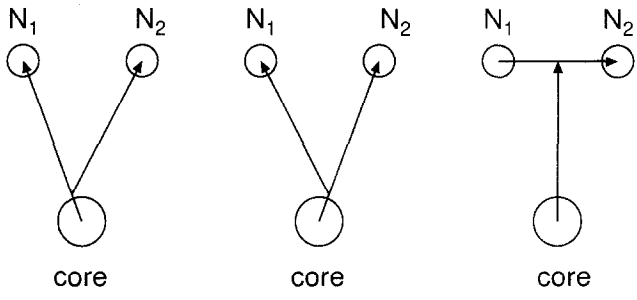

Figure 40: Jacobian coordinates of the ${}^{5}_{\Lambda}\mathrm{He} + n + p$ system.

$1^+_1) = 9.3 \pm 2.1\, e^2\mathrm{fm}^4$ for the ^{6}Li core which is well reproduced by our $^6\mathrm{Li} = {}^4\mathrm{He} + n + p$ three-body model whose prediction is $9.26\, e^2\mathrm{fm}^4$. It should be noted, however, that one cannot conclude the size-shrinkage from the reduction of the $B(E2)$ value alone since the $B(E2)$ operator $r^2 Y_{2\mu}(\theta, \phi)$ includes the angle operator. Furthermore, we should note that the shrinkage of ${}^{7}_{\Lambda}$Li can occur both along the $n-p$ relative distance and along the distance between the ^{4}He core and the c.m. of the (np) pair.

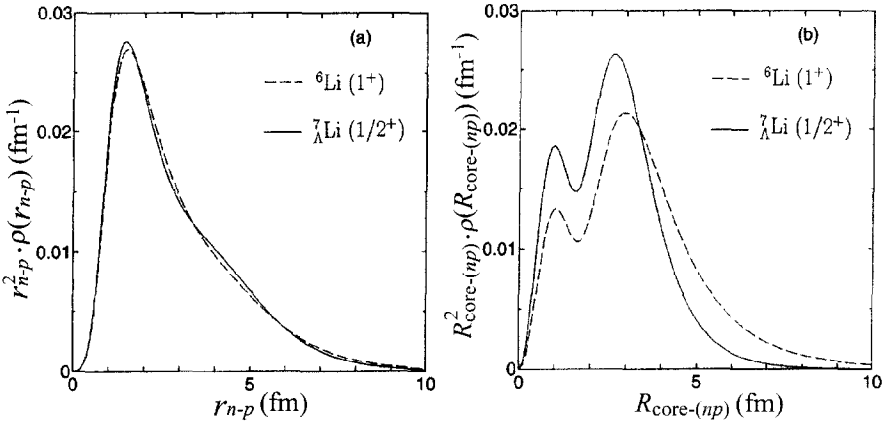

Figure 41: (a) the $n-p$ relative density of ${}^{7}_{\Lambda}$Li as a function of r_{n-p} and (b) the (np) c.m. density as a function of $R_{\mathrm{core}-(np)}$ together with the corresponding densities in ^{6}Li core. This figure is taken from [13].

We show in Fig. 41 the $n-p$ relative density $\rho(r_{n-p})$ and the np c.m. density $\rho(R_{\mathrm{core}-(np)})$ together with the corresponding densities in ^{6}Li core. The $n-p$ relative density exhibits almost the same shape for the ground state of ^{6}Li and that of ${}^{7}_{\Lambda}$Li, namely, the shrinkage of the $n-p$ distance due to the Λ participation is negligibly small. On the other hand, the $n-p$ c.m. density distribution of ${}^{7}_{\Lambda}$Li is remarkably different from that of ^{6}Li, showing a significant contraction along the $\mathbf{R}_{\mathrm{core}-(np)}$ coordinate due to the Λ addition. In fact, the r.m.s. distance $\bar{R}_{\mathrm{core}-(np)}$ is estimated to be 2.94 fm for ${}^{7}_{\Lambda}\mathrm{Li}(1/2^+)$ vs 3.85 fm for $^6\mathrm{Li}(1^+)$.

Thus, we conclude that, by the addition of the Λ particle to $^6\mathrm{Li}(1^+)$, contraction of ${}^{7}_{\Lambda}$Li occurs between the c.m. of the (np) pair and the core whereas the $n-p$ relative motion remains almost unchanged. In this type change in the wave function, the angle operator in $B(E2)$ does not significantly affect the magnitude of shrinkage. We predicted in Ref. [13] that the size of $\mathbf{R}_{\mathrm{core}-(np)}$ in ^{6}Li will shrink by 25 %

due to the participation of a Λ particle. In a later calculation [120] based on more precise ^{4}He+n+p+Λ four-body model, we predicted it to be 22 %.

The first observation of the hypernuclear $B(E2)$ strength was made in the KEK-E419 experiment for $B(E2; 5/2^+ \to 1/2^+)$ in $^7_\Lambda$Li. The observed $B(E2)$ value was $3.6 \pm 0.5^{+0.5}_{-0.4}$ e^{2}fm^4 [119]. From this, the shrinkage of $\bar{R}_{\text{core}-(np)}$ was estimated to be by 19 ± 4 %, which was consistent with our prediction. It is to be emphasized that this interesting discovery was realized with the help of our precision few-body calculations.

Nuclear shrinkage in $^{13}_\Lambda$C

One may ask the next question, "Are all nuclei compressed by the injection of a Λ particle?" Our answer is No. We shall show an example in ^{12}C and $^{13}_\Lambda$C studied in Refs. [12] and [14].

It is well known that the ground 0^+_1 state in ^{12}C has a shell model like structure while the 0^+_2 excited state at $E_x = 7.65$ MeV is a well-developed clustering state and that both states are simultaneously well described by the microscopic 3α cluster model. Using the same $3\alpha + \Lambda$ four-body model for $^{13}_\Lambda$C as in Section 7.1 we studied the shrinkage problem.

The calculated Λ separation energies of $1/2^+_1$ and $1/2^+_2$ states in $^{13}_\Lambda$C are 11.69 MeV and 8.59 MeV, respectively. The $1/2^+_1$ state is dominantly composed of the 0^+_1(^{12}C) core and a $0s$ Λ particle (99 %) and the $1/2^+_2$ is composed of the 0^+_2(^{12}C) core and a $0s$ Λ particle (77 %).

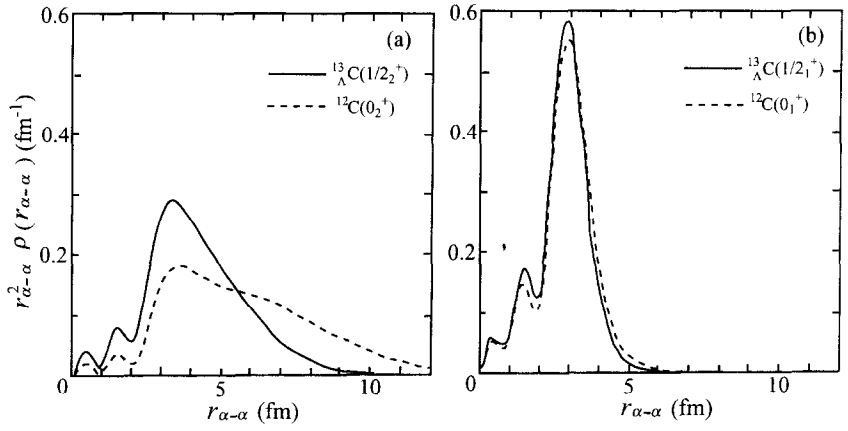

Figure 42: Probability densities of finding two α at a distance $r_{\alpha-\alpha}$ in the states (a) ^{12}C(0^+_2) and $^{13}_\Lambda$C($1/2^+_2$), and (b) ^{12}C(0^+_1) and $^{13}_\Lambda$C($1/2^+_1$). Shrinkage of the excited 0^+_2 in ^{12}C is drastic, but that in the ground state is little. This figure is taken from [12].

In the excited $1/2^+$ state in $^{13}_\Lambda$C, the r.m.s. distance between the two α clusters, $\bar{r}_{\alpha-\alpha}$, is estimated to be 4.5 fm which is much reduced from 6.3 fm (by some 30 %) in the excited 0^+ state in ^{12}C. This contraction is more vividly seen in Fig. 42a, which illustrates the probability density of finding the two αs at a distance $r_{\alpha-\alpha}$. In contrast, in the case of the ground-states pair, little change of $\alpha - \alpha$ distance is seen in Fig. 42b ; the reduction in $\bar{r}_{\alpha-\alpha}$ is from 3.0 fm in ^{12}C(0^+_1) to 2.9 fm in $^{13}_\Lambda$C($1/2^+_1$).

This results indicates that shell model like states are not easily contracted when a Λ particle joins. We then predict that the nuclear density of the ground states in the stable nuclei heavier than $A \sim 10$ will be compressed very little by the addition of a Λ particle. On the other hand, the matter radius in some excited states will shrink by as much as some a few ten % by the injection of a Λ particle. It is to be

emphasized that this interesting property has been found by the studies taking account of the three- and four-body degrees of freedom in nuclei.

Nuclear shrinkage in ${}^{4}_{\Lambda}$H and ${}^{4}_{\Lambda}$He

One may ask the question, "what is the effect of the $\Lambda-\Sigma$ conversion on the shrinkage in Λ-hypernuclei?". An answer was given in our recent work [15] on the structure of ${}^{4}_{\Lambda}$H and ${}^{4}_{\Lambda}$He already mentioned in Section 7.2. We briefly describe it here again.

We note that the Λ particle resides well outside the core and therefore the dynamical change in the core nucleus due to the Λ particle is small. In the ground state of ${}^{4}_{\Lambda}$He, the nucleon r.m.s. radius is $\bar{r}_N = 1.65$ fm which is smaller by 8 % than the corresponding $\bar{r}_N = 1.79$ fm in ^{3}He. On the other hand, the Σ hyperon lies close to the nucleons (see Figs. 37 and 38) and, therefore, generates a large dynamical contraction of the core nucleus in the $NNN\Sigma$-channel space; $\bar{r}_N = 1.49$ fm is obtained by the calculation including the Σ-channel amplitude only and the reduction amounts to 17 % in the channel. From this reduction, it is expected that $3N$ in the $NNN\Sigma$ space is strongly excited. In fact, calculated probability of finding the ground state of triton in the $NNN\Sigma$ space is only 30 %.

Neutron-rich hypernuclei and halo structure

Another interesting gluelike role of Λ particle is to give rise to more bound states. This feature of light hypernuclei has been studied mostly in systems consisting of a stable nucleus and a Λ particle. Recently, the neutron halo states have been observed in light nuclei near the neutron drip line. If a Λ particle is added to such a halo nucleus, a very weakly bound system, the resultant hypernucleus becomes substantially more stable against the neutron decay. Thanks to the gluelike role of the Λ particle, there is a new chance to produce a hypernuclear neutron (or proton) halo state even with a core nucleus in a weakly bound state or in an unbound (resonance) state with an energy above the particle decay threshold.

As a result, hypernuclei have the interesting possibility of extending the neutron (proton) drip line from that of ordinary nuclei. At J-PARC (Japan- Proton-Acceraletor-Research-Complex), BNL and TJLAB, it is planned to produce many Λ hypernuclei near the neutron and the proton drip line. Therefore, it is desirable to predict structure of these Λ hypernuclei prior to the measurements. As an example, we studied in Ref. [11] the structure of ${}^{6}_{\Lambda}$He, ${}^{6}_{\Lambda}$Li, ${}^{7}_{\Lambda}$He, ${}^{7}_{\Lambda}$Li and ${}^{7}_{\Lambda}$Be, employing $\alpha + \Lambda + N$ three-body model for ${}^{6}_{\Lambda}$He and ${}^{6}_{\Lambda}$Li, and ${}^{5}_{\Lambda}\mathrm{He} + N + N$ three-body model for ${}^{7}_{\Lambda}$He, ${}^{7}_{\Lambda}$Li and ${}^{7}_{\Lambda}$Be, and predicted some halo states in those hypernuclei (see Ref.[11] for details). We hope that many neutron- and proton-rich Λ hypernuclei will be observed in the future. That will much stimulate the study of many-body systems composed of nucleons and hyperons.

7.4 Double Λ hypernuclei

So far, we have discussed the structure of single Λ hypernuclei. What is the structure change when one or more Λs are added to a nucleus? The extreme limit is the core of a neutron star which contains many Λs,. In order to understand the structure of a neutron star core, it is essential to understand the $\Lambda\Lambda$ interaction, or in general YY interaction. However, we have little knowledge of the YY interaction because there exist no YY scattering data.

Recently two novel data from KEK-E373 experiment have offered a new basis for constraining the $\Lambda\Lambda$ interaction. One is the observation of the double Λ hypernucleus ${}^{6}_{\Lambda\Lambda}$He, which is called the NAGARA event [121]. The formation of ${}^{6}_{\Lambda\Lambda}$He was uniquely identified by the observation of sequential weak decays, and the precise experimental value of the 2Λ binding (separation) energy, $B_{\Lambda\Lambda} = 7.25 \pm 0.19^{+0.18}_{-0.11}$ MeV, was obtained. The $\Lambda\Lambda$ bond energy, estimated by $B_{\Lambda\Lambda} - 2B_{\Lambda}$ was about 1.0 MeV. Historically, there were some more observations of double Λ hypernuclei, but no unique identification had been made. In this respect, the unambiguious observation of the NAGARA event was epoch-making. Analysis of some

more emulsion data is still in progress. Furthermore, it is planned to produce many more double Λ hypernuclei at J-PARC, GSI and BNL.

Here, the important issues are: (1) Does the ΛΛ interaction which is designed to reproduce the binding energy of ${}^{6}_{\Lambda\Lambda}$He also consistently reproduce the *Demachi-Yanagi* event explained later? (2) Using this ΛΛ interaction, what is the level structure of other double Λ hypernuclei? In order to answer these questions, we studied the structure of double Λ hypernuclei ${}^{6}_{\Lambda\Lambda}$He within the $\alpha+\Lambda+\Lambda$ model, and ${}^{7}_{\Lambda\Lambda}$He, ${}^{7}_{\Lambda\Lambda}$Li, ${}^{8}_{\Lambda\Lambda}$Li, ${}^{9}_{\Lambda\Lambda}$Li, ${}^{9}_{\Lambda\Lambda}$Be and ${}^{10}_{\Lambda\Lambda}$Be within $\alpha+x+\Lambda+\Lambda$ four-body model, where $x = n, p, d, t, {}^3$He and α, respectively. It is known that the nuclear core parts are very well represented by $\alpha + x$ cluster models. We emphasize that these extensive calculations were presented for the first time for $A = 7 \sim 9$ double-Λ hypernuclei and that our old predictions on ${}^{6}_{\Lambda\Lambda}$He and ${}^{10}_{\Lambda\Lambda}$Be was updated using the same model but with the new information on the ΛΛ interaction.

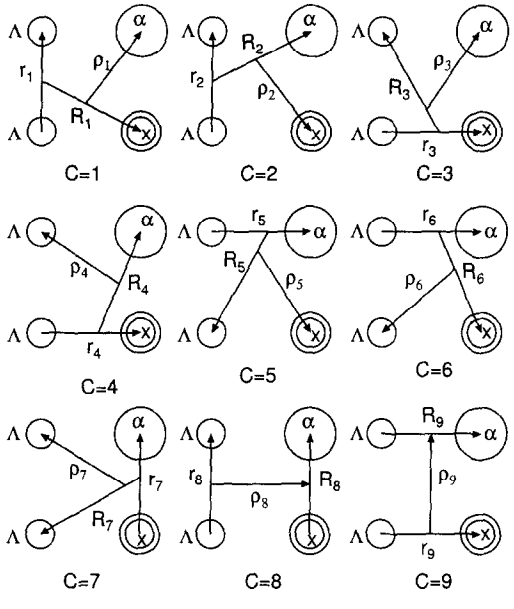

Figure 43: Jacobian coordinates for all the rearrangement channels ($c = 1 - 9$) of the $\alpha + x + \Lambda + \Lambda$ four-body system. Two Λ particles are to be antisymmetrized, and α and x are to be symmetrized when $x = \alpha$.

All nine sets of the Jacobian coordinates of the four-body system are illustrated in Fig. 43 in which we also take into account the antisymmetrization between two Λ particles and the symmetrization between two α clusters when $x = \alpha$. The total wave function is described as a sum of the components of rearrangement channels ($c = 1 - 9$) in the LS coupling scheme:

$$\Psi_{JM}({}^{A}_{\Lambda\Lambda}\mathrm{Z}) = \sum_{c=1}^{9} \sum_{n,N,\nu} \sum_{l,L,\lambda} \sum_{S,\Sigma,I,K} C^{(c)}_{nlNL\nu\lambda S\Sigma IK} \times \mathcal{A}_\Lambda \mathcal{S}_\alpha \Big[\Phi(\alpha)[\Phi_s(x)[\chi_{\frac{1}{2}}(\Lambda_1)\chi_{\frac{1}{2}}(\Lambda_2)]_S]_\Sigma [[\phi^{(c)}_{nl}(\mathbf{r}_c)\psi^{(c)}_{NL}(\mathbf{R}_c)]_I \xi^{(c)}_{\nu\lambda}(\boldsymbol{\rho}_c)]_K\Big]_{JM} . \quad (102)$$

Here the operator $\mathcal{A}_\Lambda$ stands for antisymmetrization between the two Λ particles, and $\mathcal{S}_\alpha$ is the symmetrization operator for exchange between α clusters when $x = \alpha$. $\chi_{\frac{1}{2}}(\Lambda_i)$ is the spin function of the i-th Λ particle. The eigenenergy E and the coefficients C in Eq. (102) are to be determined by the Rayleigh-Ritz variational method.

The angular-momentum space of the wave function with $l, L, \lambda \leq 2$ was found to be sufficient for getting good convergence of the binding energies of the states studied below (note that no truncation is done to the *interactions* in the angular-momentum space). As for the numbers of the Gaussian basis, $n_{\max}$, $N_{\max}$ and $\nu_{\max}$, $4 - 10$ are sufficient.

In the present four-body-model study, it is absolutely necessary to make it sure, before the four-body calculation, that the model and the interactions adopted are able to reproduce reasonably well the following observed quantities: (i) energies of the low-lying states and scattering phase shits of the $\alpha + x$ nuclear systems, (ii) B_Λ of hypernuclei composed of $x + \Lambda$, x being $d, t, {}^3\mathrm{He}, \alpha$, (iii) B_Λ of hypernuclei composed of $\alpha + x + \Lambda$, x being $n, p, d, t, {}^3\mathrm{He}, \alpha$ and (iv) $B_{\Lambda\Lambda}$ of ${}^{6}_{\Lambda\Lambda}\mathrm{He} = \alpha + \Lambda + \Lambda$. Then we perform the four-body calculations, with no adjustable parameters at this stage, expecting high reliability of the results. The parameters of the αx, Λx, ΛN and $\Lambda\Lambda$ interactions are listed in Ref.[16]. The Pauli principle between the nucleons in the α clusters are taken into account by the OCM.

It is of particular interest to compare the present result with another datum which is not used in the fitting procedure. There is an event found in the E373 experiment named the *Demachi-Yanagi* event [122, 123]. The most probable interpretation of this event is the production of a bound state of ${}^{10}_{\Lambda\Lambda}\mathrm{Be}$ having $B^{\mathrm{exp}}_{\Lambda\Lambda} = 12.33 \pm^{0.35}_{0.21}$ MeV. In the emulsion analysis there was no direct evidence for the production of ${}^{10}_{\Lambda\Lambda}\mathrm{Be}$ in an excited state. However, if the produced ${}^{10}_{\Lambda\Lambda}\mathrm{Be}$ were in the ground state, the resultant $\Lambda\Lambda$ bond energy would be repulsive, in contradiction to what was found in the NAGARA event.

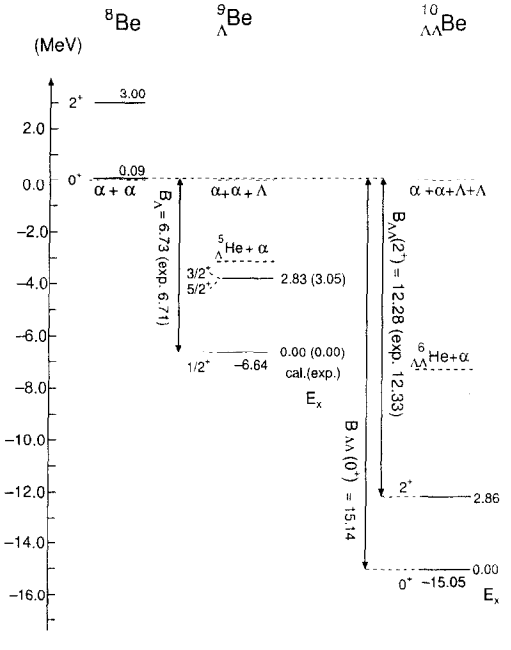

Figure 44: Calculated energy levels of ${}^{8}\mathrm{Be}$, ${}^{9}_{\Lambda}\mathrm{Be}$ and ${}^{10}_{\Lambda\Lambda}\mathrm{Be}$ on the basis of the $\alpha + \alpha, \alpha + \alpha + \Lambda$, and $\alpha+\alpha+\Lambda+\Lambda$ models, respectively. The level energies are measured from the particle breakup thresholds or are given by excitation energies E_{x}. This figure is taken from [16].

It is striking that our calculated value of $B_{\Lambda\Lambda}({}^{10}_{\Lambda\Lambda}\mathrm{Be}(2^+))$ is 12.28 MeV that agrees with the above experimental value as shown in Fig. 44. Therefore, the *Demachi-Yanagi* event can be interpreted as most probably the observation of the 2^+ excited state in ${}^{10}_{\Lambda\Lambda}\mathrm{Be}$. This good agreement suggests that our systematically calculated level structures are predictive and useful for interpreting upcoming events

expected to be found in the further analysis of the E373 data. Thus, we have understood the consistency between the experimental data and our theoretical results for ${}^{10}_{\Lambda\Lambda}$Be. Therefore, in some reality, we can predict energy spectra of double-Λ hypernuclei with $A = 6 \sim 10$ as shown in Fig.35. We expect they will be examined by the future double Λ hypernucleus experiments.

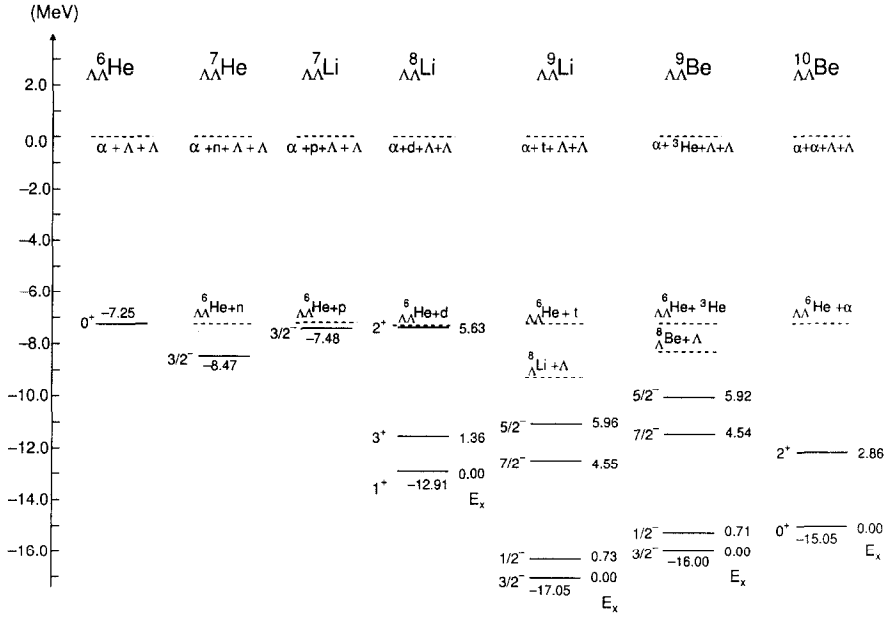

Figure 45: Energy levels of double-Λ hypernuclei, ${}^{6}_{\Lambda\Lambda}$He, ${}^{7}_{\Lambda\Lambda}$He, ${}^{7}_{\Lambda\Lambda}$Li, ${}^{8}_{\Lambda\Lambda}$Li, ${}^{9}_{\Lambda\Lambda}$Li, ${}^{9}_{\Lambda\Lambda}$be and ${}^{10}_{\Lambda\Lambda}$Be calculated using the $\alpha + x + \Lambda + \Lambda$ model with $x = 0, n, p, d, t, {}^{3}$He and α, respectively. This figure is taken from [16].

In conclusion, these extensive four-body cluster-model calculations should serve to motivate extensive spectroscopic studies of double-Λ hypernuclei.

8 Coulomb Three-Body Reactions

The GEM method is applicable to three-body reactions. So far, it has mostly been applied to Coulomb three-body reactions which appear in the cycle of muon catalyzed fusion (μCF) [25, 26, 27, 28]. In this section, we review our work [41, 42] on two types of important Coulomb three-body reactions which have been stimulating the development of three-body reaction theory.

i) Muon transfer reaction:

$$(d\mu)_{1s} + t \rightarrow d + (t\mu)_{1s} + 48\,\mathrm{eV} \tag{103}$$

is a doorway to the muon catalyzed $d - t$ fusion as mentioned in Section 5. Calculation of the cross section of this reaction at $E_{\mathrm{cm}} = 0.001 - 100$ eV has been a stringent benchmark test to calculational methods of Coulomb three-body reactions. Since the muon mass is 207 times the electron mass, fully non-adiabatic treatment is necessary. GEM gave [41] one of the most precise results reported so far.

ii) Decay branching ratio of three-body Feshbach resonance $(d\mathrm{He}\mu)_{J=1}$:

$$\begin{aligned}(d\mu)_{1s} + \mathrm{He} \rightarrow (d\mathrm{He}\mu)_{J=1} &\rightarrow (\mathrm{He}\mu)_{1s} + d + h\nu\,(\approx 6.7\,\mathrm{keV}) \\ &\rightarrow (\mathrm{He}\mu)_{1s} + d + 8.2\,\mathrm{keV}\,. \end{aligned} \tag{104}$$

Muon transfer to helium nucleus is a poison reaction in μCF as much as muon sticking to helium nucleus after fusion; both processes cause muon loss to the deeply bound $(\mathrm{He}\mu)_{1s}$ state. Since muon transfer from $(d\mu)$ to $(\mathrm{He}\mu)$ occurs dominantly via the $(d\mathrm{He}\mu)_{J=1}$ molecule, study of the property of the molecule is of importance in μCF. Using GEM, Kino and Kamimura [42] predicted presence of the strong second branch (particle decay without emitting photons). The branching ratio was found to be sensitive to the reduced mass of the d–He system (namely, the nuclear kinetic energy in the molecule), and hence generates a strong isotope effect i.e. dependence on the mass number of the He nucleus , 3 or 4. The molecular state is a Feshbach resonance embedded in the continuum of $(\mathrm{He}\mu)_{1s} - d$ channel at $E_{\mathrm{cm}} = 8.2$ keV. This prediction was later confirmed experimentally [124, 125]. This fact motivated many calculations to examine it in the literature.

The subjects i) and ii) give good tests to three-body reaction theories for elastic and transfer processes in the presence of strong three-body distortions (correlations) in the intermediate stage.

8.1 Muon transfer reaction

We consider the reaction (103) at incident c.m. energies 0.001 – 100 eV which are much less than the excitation energy of the $n = 2$ state of $(t\mu)$ and $(d\mu)$, 2 keV. The total Hamiltonian of the $d + t + \mu$

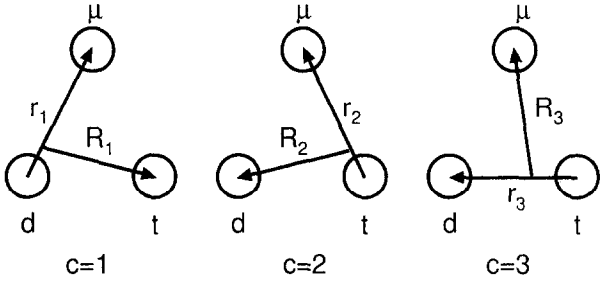

Figure 46: Three Jacobian coordinates of the $d + t + \mu$ system.

system (Fig. 46) is given by

$$H = -\frac{\hbar^2}{2m_c}\nabla^2_{\mathbf{r}_c} - \frac{\hbar^2}{2M_c}\nabla^2_{\mathbf{R}_c} - \frac{e^2}{r_1} - \frac{e^2}{r_2} + \frac{e^2}{r_3} \qquad (c = 1, 2 \text{ or } 3), \tag{105}$$

where m_c and M_c are the reduced masses associated with the coordinates $\mathbf{r}_c$ and $\mathbf{R}_c$, respectively. The wave function which describes the reaction (103) and the elastic $(t\mu)_{1s} - d$ scattering simultaneously may be written as

$$\Psi_{JM} = \phi^{(d\mu)}_{1s}(\mathbf{r}_1)\,\chi^{(d\mu-t)}_{JM}(\mathbf{R}_1) + \phi^{(t\mu)}_{1s}(\mathbf{r}_2)\,\chi^{(t\mu-d)}_{JM}(\mathbf{R}_2) + \Psi^{(\mathrm{closed})}_{JM}\,. \tag{106}$$

The first and the second terms describe the open $(d\mu)_{1s} - t$ and the $(t\mu)_{1s} - d$ channels, respectively. The third term, $\Psi^{(\mathrm{closed})}_{JM}$, describes all closed-channels. This term vanishes asymptotically, and can properly be described in the following way.

In Section 5, the three-body Hamiltonian is diagonalized for each J in a space spanned by a finite number, say N_{total}, of the three-body Gaussian basis functions written in Jacobian coordinates $\mathbf{r}_c$ and $\mathbf{R}_c$ as

$$\left[\phi^{\mathrm{G}}_{n_c l_c}(\mathbf{r}_c)\,\psi^{\mathrm{G}}_{N_c L_c}(\mathbf{R}_c)\right]_{JM} \qquad (c = 1 - 3) \tag{107}$$

with a parameter set, for example, listed in Table 10 for $J = 1$ ($N_{\rm total} = 2748$). The resultant eigenstates and eigenenergies $\{\Psi_{JM,v}\,, E_{Jv}\,;\, v = 0 - N_{\rm total}\}$ satisfy

$$\langle \Psi_{JM,v}|H|\Psi_{JM,v'}\rangle = E_{Jv}\delta_{vv'} \qquad (v, v' = 0 - N_{\rm total})\ . \tag{108}$$

The eigenstates $\Psi_{JM,v}$ with the eigenenergies E_{Jv} below and above the $(t\mu)_{1s} - d$ threshold are respectively bound states and pseudo-states which approximately describe three-body continuum in a discretized form. We assume that the pseudo-states to form a complete set in a finite space in good aapproximation where the three particles interact each other; in Section 2, we presented this property of pseudo-states in the case of two-body systems. We then consider that the closed-channel component $\Psi_{JM}^{(\rm closed)}$ can be well expanded in terms of this approximate complete set:

$$\Psi_{JM}^{(\rm closed)} = \sum_{v=0}^{N_{\rm total}} b_{Jv}\Psi_{JM,v}\ . \tag{109}$$

We next introduce radial wave functions $\chi_J^{(c)}(R_c)$ of $\chi_{JM}^{(c)}(\mathbf{R}_c)$ as

$$\chi_{JM}^{(c)}(\mathbf{R_c}) = \frac{\chi_J^{(c)}(R_c)}{R_c}Y_{JM}(\hat{\mathbf{R}}_c) \qquad (c = 1, 2)\ . \tag{110}$$

Equations for $\chi_J^{(1)}(R_1)$, $\chi_J^{(2)}(R_2)$ and the coefficient b_{Jv} are given by the Kohn-type variational method [59] as

$$\langle \phi_{1s}^{(c)}(\mathbf{r}_c)Y_{JM}(\hat{\mathbf{R}}_c)\,|H - E|\,\Psi_{JM}\rangle_{\mathbf{r}_c\hat{\mathbf{R}}_c} = 0 \qquad (c = 1, 2)\ , \tag{111}$$

and

$$\langle \Psi_{JM,v}\,|H - E|\,\Psi_{JM}\rangle = 0 \qquad (v = 0 - N_{\rm total})\ . \tag{112}$$

Here, $\langle\ \ \rangle_{\mathbf{r}_c\hat{\mathbf{R}}_c}$ denotes the integration over the $\mathbf{r}_c$ and $\hat{\mathbf{R}}_c$.

Scattering-state boundary condition for the total wave function is

$$\lim_{R_c\to\infty}\chi_J^{(c)}(R_c) = u_J^{(-)}(k_cR_c)\delta_{cc_0} - \sqrt{\frac{v_{c_0}}{v_c}}S_{cc_0}^J u_J^{(+)}(k_cR_c) \qquad (c = 1, 2), \tag{113}$$

where $c_0 = 1$ denotes the incident channel and $u_J^{(\pm)}$ is the Ricatti-Hankel function of the order J, k_c being the wave number of the channel c given by $\frac{\hbar^2}{2M_c}k_c^2 = E_{\rm c.m.}^{(c)} = E - \varepsilon_{1s}^{(c)}$. Cross sections are given by

$$\sigma_{cc_0} = \frac{\pi}{k_{c_0}^2}\sum_J(2J+1)|\delta_{cc_0} - S_{cc_0}^J|^2 \qquad (c = 1, 2). \tag{114}$$

The simultaneous Eqs. (111) and (112) are solved in the following manner. Firstly, from Eqs. (108) and (112), b_{Jv} in Eq.(109) is given by

$$b_{Jv} = \frac{-1}{E_{Jv} - E}\langle\Psi_{JM,v}|H - E|\phi_{1s}^{(1)}(\mathbf{r}_1)\chi_{JM}^{(1)}(\mathbf{R}_1) + \phi_{1s}^{(2)}(\mathbf{r}_2)\chi_{JM}^{(2)}(\mathbf{R}_2)\rangle\ . \tag{115}$$

Inserting Eq.(115) into Eqs.(111), and performing the integration, we reach the following coupled integro-differential equations for $\chi_J^{(1)}(R_1)$ and $\chi_J^{(2)}(R_2)$:

$$\begin{aligned}&\Big[-\frac{\hbar^2}{2M_c}\frac{d^2}{dR_c{}^2} + \frac{\hbar^2}{2M_c}\frac{J(J+1)}{R_c^2} + U^{(c)}(R_c) - E_{\rm c.m.}^{(c)}\Big]\chi_J^{(c)}(R_c) + \int_0^\infty V_J^{(cc)}(R_c, R_c')\chi_J^{(c)}(R_c')dR_c' \\ &= -\int_0^\infty V_J^{(cc')}(R_c, R_{c'})\chi_J^{(c')}(R_{c'})dR_{c'}\ , \qquad \text{for } (c, c') = (1,2) \text{ and } (2,1)\ ,\end{aligned} \tag{116}$$

where

$$U^{(c)}(R_c) = \langle\phi_{1s}^{(c)}(\mathbf{r}_c)Y_{JM}(\hat{\mathbf{R}}_c)\,|\,-\frac{e^2}{r_c} + \frac{e^2}{r_3}\,|\,\phi_{1s}^{(c)}(\mathbf{r}_c)Y_{JM}(\hat{\mathbf{R}}_c)\rangle_{\mathbf{r}_c\hat{\mathbf{R}}_c}, \tag{117}$$

$$V_J^{(cc)}(R_c, R'_c) = \sum_{v=0}^{N_{\rm total}} R_c R'_c \langle \phi_{1s}^{(c)}(\mathbf{r}_c) Y_{JM}(\hat{\mathbf{R}}_c) \, |H - E| \, \Phi_{JM,v} \rangle_{\mathbf{r}_c \hat{\mathbf{R}}_c} \times \frac{-1}{E_{Jv} - E} \langle \Phi_{JM,v} \, |H - E| \, \phi_{1s}^{(c)}(\mathbf{r}'_c) Y_{JM}(\hat{\mathbf{R}}'_c) \rangle_{\mathbf{r}'_c \hat{\mathbf{R}}'_c}, \quad (118)$$

$$V_J^{(cc')}(R_c, R_{c'}) = R_c R_{c'} \langle \phi_{1s}^{(c)}(\mathbf{r}_c) Y_{JM}(\hat{\mathbf{R}}_c) | H - E | \phi_{1s}^{(c')}(\mathbf{r}_{c'}) Y_{JM}(\hat{\mathbf{R}}_{c'}) \rangle_{\hat{\mathbf{R}}_c \hat{\mathbf{R}}_{c'}} + \sum_{v=0}^{N_{\rm total}} R_c R_{c'} \langle \phi_{1s}^{(c)}(\mathbf{r}_c) Y_{JM}(\hat{\mathbf{R}}_c) \, |H - E| \, \Phi_{JM,v} \rangle_{\mathbf{r}_c \hat{\mathbf{R}}_c} \times \frac{-1}{E_{Jv} - E} \langle \Phi_{JM,v} \, |H - E| \, \phi_{1s}^{(c')}(\mathbf{r}_{c'}) Y_{JM}(\hat{\mathbf{R}}_{c'}) \rangle_{\mathbf{r}_{c'} \hat{\mathbf{R}}_{c'}}. \quad (119)$$

Calculation of the non-local potentials can be performed analytically. We then solve the integro-differential equations (116) using the direct numerical method (almost the same result was obtained using the Kohn-type variational method of Section 2.5 with the Gaussian basis functions as trial functions [5]).

Calculated cross sections converged quickly as increasing number of the pseudo-states $\Psi_{JM,v}$, summation up to $v \approx 50$ ($E_{Jv} - E < 3$ keV) is sufficient for the accuracy needed in the present calculations. The form of b_{Jv} in Eq. (115), looks singular at E=$E_{J,v}$. However, b_{Jv} changes smoothly except for an extremely small vicinity of E=$E_{J,v}$ since the numerator of Eq. (115) is nearly proportional to $E - E_{J,v}$ around E=$E_{J,v}$; in actual calculations with 15-decimal-digits arithmetics, b_{Jv} is found to be a smooth function of E except for the region $|E_{J,v} - E| < 10^{-10}$ eV which can be neglected. As seen in Fig.47, we have smooth functions of the cross section as a function the scattering energy.

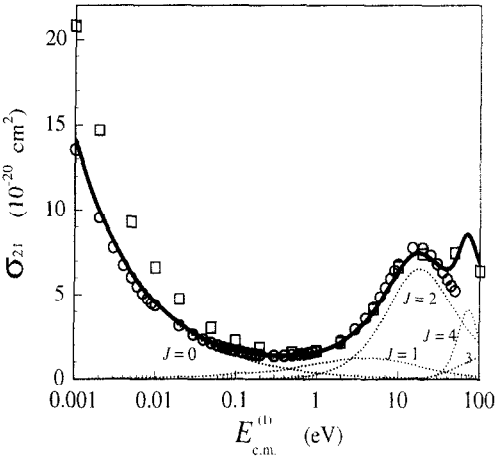

Figure 47: Calculated transfer cross sections σ_{21} of $(d\mu)_{1s} + t \rightarrow d + (t\mu)_{1s} + 48$ eV by GEM [41, 126] (solid line), by Cohen and Struensee [127] (open boxes) and by Chiccori *et al.*[128] (open circles). Dotted lines are partial-wave cross sections for each J by GEM. $E_{\rm c.m.}^{(1)} = E - \varepsilon_{1s}^{(1)}$ is the collision energy in the incident channel.

Calculated cross section σ_{21} for the transfer reaction (103) at $E_{\rm c.m.}^{(1)} = 0.001 - 100$ eV were given in Ref.[41] and afterwards revised slightly [126]. The result was compared with that reported by Cohen and Struensee [127] obtained with the improved adiavatic calculation and by Chiccoli *et al.* [128]

Table 18: Calculated $J = 0$ cross section of the transfer reaction $(d\mu)_{1s} + t \rightarrow d + (t\mu)_{1s} + 48\,\mathrm{eV}$ by Kino and Kamimura [41, 126] and Tolstikhin *et al.*[129]. $E^{(1)}_{\mathrm{c.m.}}$ is the collision energy in the initial state, in eV. Cross section is in units of cm^2; $a[b] = a \times 10^b$. This may be used for a benchmark test calculation of any Coulomb three-body method.

$E^{(1)}_{\mathrm{c.m.}}$	Kino & Kamimura	Tolstikhin *et al.*
0.001	1.415 [-19]	1.436 [-19]
0.005	6.308 [-20]	6.405 [-20]
0.01	4.555 [-20]	4.514 [-20]
0.05	1.968 [-20]	1.979 [-20]
0.1	1.374 [-20]	1.373 [-20]
0.5	5.650 [-21]	5.637 [-21]
1	3.754 [-21]	3.749 [-21]
5	1.379 [-21]	1.377 [-21]
10	8.827 [-22]	8.808 [-22]
100	1.907 [-22]	1.905 [-22]
1000	3.411 [-23]	3.177 [-23]

with an adiabatic expansion in terms of the two-center Coulomb basis. Agreement among the three calculations was good except for the lowest and the highest energy regions. Since Chiccori *et al.* did not calculate the higher partial wave components ($J > 4$), they could not reproduce the second peak due to the $J = 4$ component. Recently, the cross section for the $J = 0$ component only was reported by Tolstikhin and Namba [129] calculated with hyperspherical coordinate method and by Kvitsinsky *et al.* [130] calculated with the Faddeev method. The former authors reviewed many calculations of the cross sections ($J = 0$) in the literature and concluded that their values agreed excellently with those of our GEM calculation. The values are listed in Table 18 for the sake of future benchmark test by any method for Coulomb three-body reaction calculation.

Computation time was very short; for a particular total angular momentum J, the time for all the local and non-local potentials was about 100 sec and that for solving the coupled-channel equations (116) was only 15 sec per one scattering energy on FACOM VP2600 in 1992. This high speed computation will be useful for systematic studies of various muonic atom-nucleus collisions at thermal and epithermal energies.

Finally, we remark that the equation (116) through (119) can be used for the calculation of $(d\mu)_{1s} + t$ elastic scattering just by taking $c_0 = 2$. Calculated result in this case was given in [41]

8.2 Decay branching ratio of three-body Feshbach resonance

Since energy of $(\mathrm{He}\mu)_{1s}$ is much lower than that of $(d\mu)_{1s}$, no molecular orbital associated with the $(\mathrm{He}\mu)_{1s}$ is formed and therefore $(d\mathrm{He}\mu)$ molecule has no bound states. However, there are two metastable states, $(d\mathrm{He}\mu)_{J=1}$ and $(d\mathrm{He}\mu)_{J=0}$, below the $(d\mu)_{1s}$ – He threshold both for He = ^{3}He and ^{4}He; they are Feshbach resonances embedded in the the $(\mathrm{He}\mu)_{1s} - d$ continuum. The $(d\mathrm{He}\mu)_{J=0}$ resonance is of little interest since it is not generated in μCF; the Auger transition from the $(d\mathrm{He}\mu)_{J=1}$ state to the lower-lying $(d\mathrm{He}\mu)_{J=0}$ state is hindered because the energy difference between the two states is small. Spectrum of the *bound-to-free* X-ray in the first branch of (104) was beautifully observed, in the case of He=^{4} He, by Matsuzaki *et al.* [131], and this is regarded as the first observation of the direct signature of the existence of muonic molecule (recently, the X-rays were observed more precisely in [125]).

However, before another X-ray measurement on $(d^3\mathrm{He}\mu)_{J=1}$ was reported, Kino and Kamimura predicted that the X-rays from this molecule would be very much suppressed compared with those from $(d^4\mathrm{He}\mu)_{J=1}$, and those from $(p^4\mathrm{He}\mu)_{J=1}$ would not be observed at all since the suppression is even stronger. This prediction was corroborated by the experiment [124, 125], and the reason of this isotope dependence turned out to be interesting as we report below.

The Jacobian coordinates of the $d + \mathrm{He} + \mu$ system are given in Fig. 48.

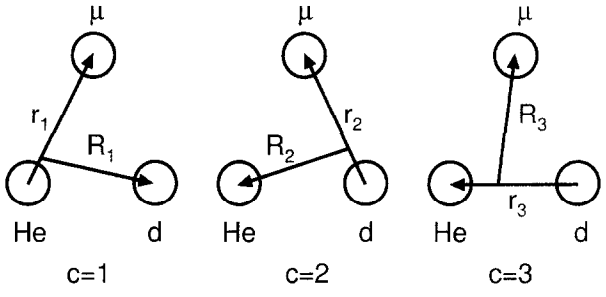

Figure 48: Three Jacobian coordinates of the $d + \mathrm{He} + \mu$ system.

The total three-body Hamiltonian is given by

$$H = -\frac{\hbar^2}{2m_c}\nabla^2_{\mathbf{r}_c} - \frac{\hbar^2}{2M_c}\nabla^2_{\mathbf{R}_c} - \frac{2e^2}{r_1} - \frac{e^2}{r_2} + \frac{2e^2}{r_3} \qquad (c = 1, 2 \text{ or } 3). \tag{120}$$

Kino and Kamimura [42] made similar calculation as in the previous subsection introducing the total wave function

$$\Psi_{JM} = \phi^{(\mathrm{He}\mu)}_{1s}(\mathbf{r}_1)\,\chi^{(\mathrm{He}\mu-d)}_{JM}(\mathbf{R}_1) + \Psi^{(\mathrm{closed})}_{JM} \,. \tag{121}$$

The first term describes the open $(\mathrm{He}\mu)_{1s}-d$ channel ($c = 1$). The $(d\mu)_{1s}-\mathrm{He}$ channel ($c = 2$) is closed at the energy of the relevant Feshbach resonance, $(d\mathrm{He}\mu)_{J=1}$. The second term, $\Psi^{(\mathrm{closed})}_{JM}$, stands for all the closed channels and is expanded in the three-body eigenstates (pseudo-states) $\{\Psi_{JM,v};\, v = 0 - N_{\mathrm{total}}\}$:

$$\Psi^{(\mathrm{closed})}_{JM} = \sum_{v=0}^{N_{\mathrm{total}}} b_{Jv}\Psi_{JM,v} \,. \tag{122}$$

The three-body pseudo-states $\{\Psi_{JM,v}\}$ are obtained by diagonalizing the Hamiltonian using the Gaussian basis functions

$$\left[\phi^{\mathrm{G}}_{n_c l_c}(\mathbf{r}_c)\,\psi^{\mathrm{G}}_{N_c L_c}(\mathbf{R}_c)\right]_{JM} \qquad (c = 1 - 3). \tag{123}$$

The Gaussian parameter set is listed in Table 19.

The partial cross section for each J of the elastic d–$(\mathrm{He}\mu)_{1s}$ scattering is defined by

$$\sigma_J(E) = \frac{\pi}{k_1^2}(2J+1)|S^J_{11} - 1|^2. \tag{124}$$

Calculated partial cross sections for $J = 1$ at energies in the vicinity of the resonances $(d^3\mathrm{He}\mu)_{J=1}$ and $(d^4\mathrm{He}\mu)_{J=1}$ are illustrated in Fig. 49 with the closed circles. The solid lines are the best fit to them by the single-level resonance formula

$$\sigma_J(E) = \frac{\pi}{k_1^2}(2J+1)\left|e^{-2i\delta_{\mathrm{b.g.}}} - 1 + \frac{i\Gamma}{E - E_{\mathrm{res.}} + i\Gamma/2}\right|^2 , \tag{125}$$

Table 19: Parameters of the Gaussian basis functions for $(d\mathrm{He}\mu)_{J=1}$.

c	l	$n_{\max}$	$r_1 \sim r_{N_{\max}}$ (fm)	L	$N_{\max}$	$R_1 \sim R_{N_{\max}}$ (fm)
1,2	0	20	$2 \sim 4000$	1	20	$50 \sim 8000$
	1	17	$35 \sim 4400$	0	18	$60 \sim 6600$
	1	14	$60 \sim 1500$	2	14	$100 \sim 3500$
	2	15	$70 \sim 3700$	1	15	$100 \sim 4500$
	2	9	$70 \sim 1500$	3	9	$200 \sim 3500$
	3	9	$70 \sim 2500$	2	9	$200 \sim 3500$
3	0	13	$50 \sim 3000$	1	13	$100 \sim 2000$
	1	10	$100 \sim 1500$	0	10	$100 \sim 1500$
	1	8	$100 \sim 2000$	2	8	$100 \sim 2000$
	2	8	$100 \sim 2000$	1	8	$100 \sim 2000$
	2	7	$100 \sim 1500$	3	6	$100 \sim 1500$
	3	7	$100 \sim 2500$	2	6	$100 \sim 1500$

where Γ is the width of the resonance and $\delta_{b.g.}$ is the background-scattering phase shift calculated at off-resonant energies. Closed circles are precisely fitted by the solid curves whose parameters are listed in Table 20; the values of the resonance energies are shown for $E_{\mathrm{res.}} - \varepsilon_{1s}^{d\mu}$.

It was found that the widths of the resonances are affected only by a few parts of 10^{-6} eV by reasonable change of the parameters of the basis functions. The numbers in the parentheses in Table 20 are for the limited case in which we employ those only pseudo-states $J = 1, v = 0$ which are located in the vicinity of the resonances; the effect of the non-resonant pseudo-states could not be neglected in the calculation of the resonant widths. Stimulated by the interest of the problems, several other calculations were performed later on the energies and widths of those two resonances, but the results were significantly different from that of GEM. Finally, Korobov [132] showed, on the basis of a precise calculation using the complex-coordinate-rotation method, that his result agreed very well with that of GEM as shown in Table 20.

Successful prediction by GEM

It is striking that Table 20 shows that the probability (width) of particle decay is three times higher for $(d^3\mathrm{He}\mu)_{J=1}$ than for $(d^4\mathrm{He}\mu)_{J=1}$. The reason for this is that the probability of the particle decay into d–$(\mathrm{He}\mu)_{1s}$ scattering states is very sensitive to the tail of the wave function of the $(d\mathrm{He}\mu)_{J=1}$ state, and the tail of $(d^3\mathrm{He}\mu)_{J=1}$ is longer than that of $(d^4\mathrm{He}\mu)_{J=1}$ due to the small binding energy with respect to the d–$(\mathrm{He}\mu)_{n=2}$ breakup threshold; this comes from the fact that the kinetic energy of relative motion is larger in $d - {}^3\mathrm{He}$ than in $d - {}^4\mathrm{He}$ due to the mass effect.

The X-ray decay rate of $(d^4\mathrm{He}\mu)_{J=1}$ was estimated [133] to be $\lambda_{\mathrm{X}} = 1.69 \times 10^{11}\ \mathrm{s}^{-1}$ which is the same as the particle decay rate $\lambda_{\mathrm{p}} = \Gamma/\hbar = 1.67 \times 10^{11}\ \mathrm{s}^{-1}$. On the other hand, that of $(d^3\mathrm{He}\mu)_{J=1}$, $\lambda_{\mathrm{X}} = 1.55 \times 10^{11}\ \mathrm{s}^{-1}$ is three times as small as $\lambda_{\mathrm{p}} = 5.06 \times 10^{11}\ \mathrm{s}^{-1}$. This is the main reason for the isotope dependence of the X-ray yields from the two kinds of molecules (branching ratio is summarized in Table 21). In the observation of the X-ray in the reaction (104), the formation rate of the muonic molecule $(d\mathrm{He}\mu)_{J=1}$ also affects the X-ray yields. Taking this into account, Ishida *et al.* [124] compared the observed and predicted values together with the case of $(p^4\mathrm{He}\mu)_{J=1}$; this is summarized in the lower part of Table 21. One sees that the observed isotope effect is well understood by the theoretical finding mentioned above.

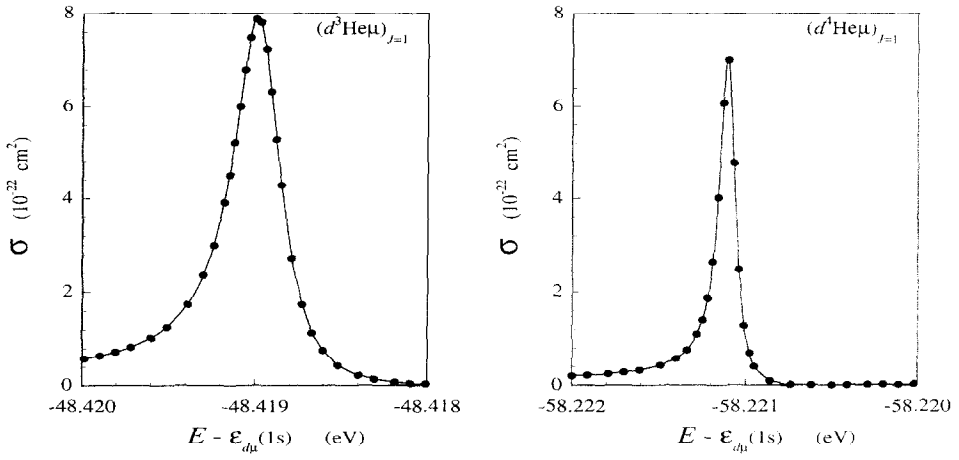

Figure 49: Energy dependence of elastic $(\mathrm{He}\mu)_{1s} - d$ scattering cross sections in the visinity of the molecular resonances of $(d^3\mathrm{He}\mu)_{J=1}$ and $(d^4\mathrm{He}\mu)_{J=1}$. Closed circles represent calculated results and the solid lines the fit by formula (125). Energy of the horizontal axis is measured from the $(d\mu)_{1s} - \mathrm{He}$ threshold; scattering c.m. energy of $(\mathrm{He}\mu)_{1s} - d$ is ~8.1 keV at the resonances. This figure is taken from [42].

Table 20: Calculated resonance parameters of $(d\mathrm{He}\mu)_{J=1}$ by Kino and Kamimura [42] with GEM and by Korobov [132] with the complex-coordinate-rotation method. The numbers in the parentheses are for a limited case where we employ, in the calculation of the coupling potentials, the only pseudo-state $J = 1, v = 0$ at which the Feshbach resonance is located.

	$E_{\mathrm{res}} - \varepsilon_{1s}^{d\mu}$	Γ (eV)	$\delta_{\mathrm{b.g.}}$ (deg)
Kino & Kamimura [42]			
$(d^3\mathrm{He}\mu)_{J=1}$	−48.419 (−48.419)	3.33×10^{-4} (3.9×10^{-4})	6.55 (3.7)
$(d^4\mathrm{He}\mu)_{J=1}$	−58.221 (−58.221)	1.10×10^{-4} (1.4×10^{-4})	6.25 (1.3)
Korobov [132]			
$(d^3\mathrm{He}\mu)_{J=1}$	−48.421	3.48×10^{-4}	
$(d^4\mathrm{He}\mu)_{J=1}$	−58.225	1.18×10^{-4}	

9 CDCC Method for Four-body Breakup Reactions

The method of Continuum-Discretized Coupled Channels (CDCC) which was developed by the Kyushu Group [43] has been successful in describing nuclear reactions involving breakup processes of weakly bound projectiles [44, 45, 46, 47, 48, 49, 50, 51, 52] and of unstable nuclei [53, 54]. CDCC is a fully quantum-mechanical way of treating three-body breakup processes. It solves the three-body dynamics by discretizing continuous intrinsic states of the projectile into a finite number of discrete ones.

CDCC is attracting a great deal of attention due to the advent of many experiments using radioactive beams since projectile breakup processes are in general essential to such reactions. CDCC is thus

Table 21: Calculated branching ratio of X-ray decay to (X-ray decay + particle decay) in $(d^{3,4}\mathrm{He}\mu)_{J=1}$ and $(p^4\mathrm{He}\mu)_{J=1}$ (upper part), and relative X-ray yields with the formation rate of the molecule is taken into account (lower part).

	$(d^4\mathrm{He}\mu)_{J=1}$	$(d^3\mathrm{He}\mu)_{J=1}$	$(p^4\mathrm{He}\mu)_{J=1}$
$\lambda_X/(\lambda_X+\lambda_p)$ [42]	0.503	0.234	0.095
X-ray relative yield			
EXP [124]	1	0.123(19)	0.002 (19)
CAL [124, 42]	1	0.096	0.007

important in the spectroscopy of unstable nuclei by scattering experiments. So far, the projectile has been assumed to be composed of two particles in CDCC calculations. However, reactions induced by some important unstable nuclei such as $^6\mathrm{He}(=\alpha+n+n)$, $^8\mathrm{B}(=\alpha+{}^3\mathrm{He}+p)$,^{11} Li$(=\,^9\mathrm{Li}+n+n)$ are typical examples of projectiles composed of three particles (clusters).

It is possible to extend CDCC, in combination with GEM, to projectile breakup processes in which the projectile is formed by three particles. From the studies in the previous sections, we consider that eigenstates of three-body systems obtained by GEM form an approximate complete set in a finite space sensitive to the projectile breakup processes.

This idea is supported by a recent CDCC work by Matsumoto *et al.* including two of the authors (E.H. and M.K.) [134]; breakup continuum states of two-body projectiles were found to be well approximated by discrete eigenstates (pseudo-states) obtained by diagonalizing the intrinsic two-body Hamiltonian with the complex-range Gaussian basis functions proposed in Section 2.3.

In this section, we briefly introduce the work of Matsumoto *et al.* and suggest an extension to four-body breakup processes induced by (unstable) projectiles composed of three particles.

9.1 Pseudo-state CDCC

CDCC treats a three-body system shown in Fig. 50 in which the projectile (B) is composed of two particles (b and c) and the target nucleus (A) which is assumed to be an inert core. Assuming a model Hamiltonian

$$H = H_{\mathrm{bc}} + T_R + U_{\mathrm{bA}}(\mathbf{r}_{bA}) + U_{\mathrm{cA}}(\mathbf{r}_{cA}) + U_{\mathrm{c}}(R), \qquad H_{\mathrm{bc}} = T_r + V_{\mathrm{bc}}(\mathbf{r}). \tag{126}$$

V_{bc} is the interaction between b and c, while U_{bA} (U_{cA}) is the optical potential between b (c) and A. For simplicity, the spin part of each potential is neglected. Furthermore, the sum of the Coulomb parts of the optical potentials are treated approximately as the Coulomb potential acting on the center of mass of the systems b + c and A, $U_{\mathrm{c}}(R)$. We neglect the Coulomb breakup process and focus on nuclear breakup.

In CDCC, the three-body wave function Ψ_{JM} is expanded in terms of a discretized orthonormal set of eigenstates $\{\psi_l^{(i)}(r)\,;\, i=0-i_{\max}\}$ of H_{bc}:

$$\Psi_{JM} = \left[\psi_{l_0}^{(0)}(\mathbf{r})\,\chi_{l_0L_0}^{(0)}(\mathbf{R})\right]_{JM} + \sum_{l=0}^{l_{\max}}\sum_{L}\sum_{i=1}^{i_{\max}}\left[\psi_l^{(i)}(\mathbf{r})\,\chi_{lL}^{(i)}(\mathbf{R})\right]_{JM} \tag{127}$$

where $\chi_{lL}^{(i)}$ describes the center-of-mass motion of the b-c pair in the state $\psi_l^{(i)}$. The state $i=0$ denotes

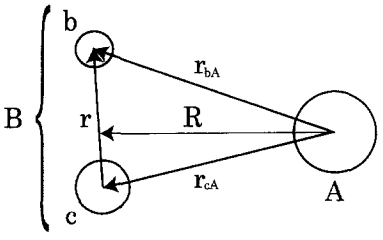

Figure 50: Illustration of a three-body (A+b+c) system in CDCC.

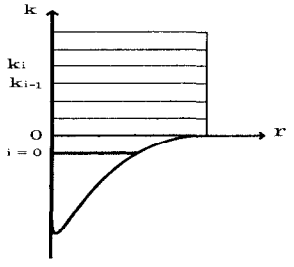

Figure 51: Discretization of two-body continuum states using the momentum bin method.

the ground state of the projectile (we assume here $l_0 = 0$). We introduce the radial functions $\psi_l^{(i)}(r)$ and $\chi_{lL}^{(i)}(R)$ by $\psi_{lm}^{(i)}(\mathbf{r}) = \psi_l^{(i)}(r)Y_{lm}(\hat{\mathbf{r}})$ and $\chi_{lLM}^{(i)}(\mathbf{R}) = \chi_{lL}^{(i)}(R)Y_{LM}(\widehat{\mathbf{R}})$.

The method of momentum bins

In usual CDCC calculations, the discretized eigenstates $\psi_l^{(i)}(r)$ are constructed by dividing the momentum (k) continuum states $\{\phi_l(k,r); 0 < k < k_{\max}\}$ of the b-c system into a finite number ($i_{\max}$) of bins and then averaging the continuum wave function in each bin (Fig. 51):

$$\psi_l^{(i)}(r) = \frac{1}{\sqrt{\Delta_i}} \int_{k_{i-1}}^{k_i} \phi_l(k,r)\, dk, \qquad \Delta_i = k_i - k_{i-1}, \qquad (i = 1 - i_{\max}). \tag{128}$$

Since the orthonormal relation $\langle \psi_{lm}^{(i)} \,|\, \psi_{lm}^{(i')} \rangle = \delta_{i,i'}$ is satisfied, each $\psi_{lm}^{(i)}$ is regarded as if it were an inelastic-channel wave function whose energy is given by $\epsilon_i = \langle \psi_{lm}^{(i)} \,|\, H_{\rm bc} \,|\, \psi_{lm}^{(i')} \rangle = \hbar^2 \hat{k}_i^{\,2}/2\mu_{\rm bc}$ with $\hat{k}_i^{\,2} = (k_i + k_{i-1})^2/4 + \Delta_i^2/12$.

Inserting Eq. (127) into the three-body Schrödinger equation, $(H - E)\Psi_{JM} = 0$, leads to a set of coupled differential equations for $\chi_{l_0L_0}^{(0)}(R)$ and $\chi_{lL}^{(i)}(R)$ [134] though explicit form of them is not written down here. The equations are solved by the direct numerical method under the asymptotic boundary condition

$$\chi_{lL}^{(i)}(\hat{P}_i, R) \sim u_L^{(-)}(\hat{P}_i, R)\delta_{i,0}\delta_{l,l_0}\delta_{L,L_0} - \sqrt{\hat{P}_i/\hat{P}_0}\, \hat{S}_{lL,l_0L_0}^{(i)}\, u_L^{(+)}(\hat{P}_i, R)\,. \tag{129}$$

Here $u_L^{(-)}(\hat{P}_i, R)$ and $u_L^{(+)}(\hat{P}_i, R)$ are incoming and outgoing Coulomb wave functions with $\hat{P}_i$, and $\hat{S}_{lL,l_0L_0}^{(i)}$ is the S-matrix element for the transition from the initial channel $\{l_0, L_0, i = 0\}$ to $\{l, L, i\}$. Each of momentum pairs, (k_0, P_0) and $(\hat{k}_i, \hat{P}_i)$, satisfies the total energy conservation: $\hbar^2\hat{P}_i^{\,2}/2\mu_{\rm AB} + \epsilon_i = E$. Continuous S-matrix element $S_{lL}(k)$ for the excited states $\{\phi_l(k,r); 0 < k < k_{\max}\}$ of the b-c system is assumed to be given by

$$S_{lL}(k) = \hat{S}_{lL,L_0l_0}^{(i)}/\Delta_i \qquad (k_i < k < k_{i-1}) \tag{130}$$

which is constant within each momentum bin. Convergence of the S-matrix element with respect to incleasing $l_{\max}$ and $k_{\max}$ as well as decreasing Δ_i has been confirmed in [52].

Pseudo-state method for three-body breakup

Recently, Matsumoto *et al.* [134] proposed a new treatment of breakup continuum in CDCC. The discrete orthonormal set $\{\psi_l^{(i)}; i = 0 - i_{\max}\}$ is obtained by diagonalizing the two-body Hamiltonian $H_{\rm bc}$ using (complex-range) Gaussian basis functions in the same manner as in Section 2.4 where the set of pseudo-states $\{\psi_l^{(i)}\}$ was found to form a complete set in a finite space. In this method, which is called pseudo-state method [134], the continuous S-matrix element, $S_{lL}(k)$, is calculated as follows.

Fitst, the continuous T-matrix element is defined by

$$T_{lL}(k) = \langle \psi_l(k,r)\, j_L(PR) \left[Y_l(\hat{\mathbf{r}})\, Y_L(\widehat{\mathbf{R}}) \right]_{JM} | U | \Psi^{\rm CDCC}_{JM} \rangle \,, \tag{131}$$

where $U = U_{\rm bA}(\mathbf{r}_{bA}) + U_{\rm cA}(\mathbf{r}_{cA})$. Using an approximate complete set $\{\psi_l^{(i)}\}$, $T_{lL}(k)$ may be rewritten as

$$T_{lL}(k) = \sum_{i=0}^{i_{\rm max}} \langle \psi_l(k,r') | \psi_l^{(i)}(r') \rangle \langle \psi_l^{(i)}(r)\, j_L(P_i R) \left[Y_l(\hat{\mathbf{r}})\, Y_L(\widehat{\mathbf{R}}) \right]_{JM} | U | \Psi^{\rm CDCC}_{JM} \rangle \,, \tag{132}$$

where P has been replaced by a P_i in the spherical Bessel function $j_L(PR)$. This replacement is valid, since the k-distribution of $\langle \psi_l(k,r') | \psi_l^{(i)}(r') \rangle$ is sharply localized at $k = \hat{k}_i$. We shall show below that the approximation (132) is very good. The second matrix element $\langle \ \ \rangle$ in (132) is nothing but the T-matrix element of CDCC. Since the breakup T-matrix element is propotional to the corresponding S-matrix element, the continuous S-matrix element $S_{lL}(k)$ is expressed as

$$S_{lL}(k) = \sum_{i=0}^{i_{\rm max}} \langle \psi_l(k,r) | \psi_l^{(i)}(r) \rangle\, S^{(i)}_{lL,i_0 L_0} \,. \tag{133}$$

The two expressions (130) and (133) is compared to each other below.

Test for ^{6}Li projectile breakup

Test of the pseudo-state CDCC method was done in [134] on the ^{6}Li ($= \alpha + d$) projectile breakup in ^{6}Li + ^{40}Ca at 156 MeV. This was a good example since ^{6}Li had d-wave resonance and s-wave non-resonant continuum states. For simplicity, the intrinsic spin of ^{6}Li was neglected. We took the same $\alpha - d$ potential as in Section 2.3; $V_{\alpha-d}(r) = V_0\, e^{-(r/b)^2}$ with $V_0 = -74.19$ MeV and $b = 2.236$ fm which generates an $l = 2$ resonace at $\epsilon_{\rm res} = 2.96$ MeV with width 0.62 MeV. $U_{\alpha-^{40}{\rm Ca}}$ and $U_{d-^{40}{\rm Ca}}$ are the optical potential of α+^{40}Ca scattering at 104 MeV [135] and that of d+^{40}Ca scattering at 56 MeV [136].

The model space sufficient to describe breakup processes in this scattering was $k_{\rm max} = 1.8$ fm^{-1} and $l = 0, 2$. In the momentum bin method, the d-wave k-continuum is further divided into the resonance part $[0 < k < 0.55]$ and the non-resonant part $[0.55 < k < 1.8]$. The k-continuum of $\psi_l(k,r)$ in the resonance part varies rapidly with k. In principle, the bin method can simulate the rapid change with a large number of dense bins. Such a CDCC calculation was done to obtain the accutrate breakup S-matrix elements. Clear convergence was found for both the elastic and the breakup S-matrix elements with 30 bins of a common width for the resonance part and with 20 bins for the entire region of the s-wave k-continuum and the non-resonance part of the d-wave k-continuum. The S-matrix elements so obtained were compared with the pseudo-state method. In the latter, convergence of the S-matrix elements was achieved with 21 pseudo-states for the s-wave k-continuum, 13 pseudo-states for the d-wave non-resonant k-continuum and 8 pseudo-states for the d-wave resonance part. The parameter set of the complex-range Gaussians were $\{r_1 = 1.0\,{\rm fm}, r_{20} = 20.0\,{\rm fm}, \alpha = \pi/2, 2n_{\rm max} = 40\ \}$.

The momentum bin method and the pseudo-state method gave the same differential cross section of the elastic scattering up to 180°. The squared modulus of the breakup S-matrix element $|S_{lLJ}(k)|^2$ at grazing angular momentum $J = 43$ is illustrated in Fig. 52. The pseudo-state method well reproduces the accurate solution calculated by the bin method with dense bins. The resonance peak is expressed by only 8 pseudo-state channels, while the corresponding number of breakup channels is 30 in the bin method. The pseudo-state method with the complex-range Gaussians is thus useful for describing both resonance and non-resonant states. In a sense, it is more convenient than the bin method, at least in dealing with the nuclear breakup; study of applicability to the Coulomb break up is in progress.

In conclusion, we have confirmed that the set of of pseudo-states $\{\psi_l^{(i)}(r)\,;\, i = 0 - i_{\rm max}\}$ can forms an approximate complete set in a finite (rather large) space that is important to the breakup reaction.

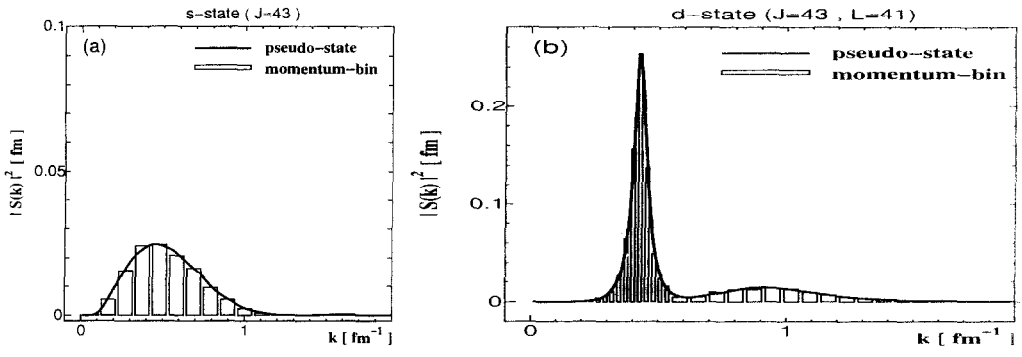

Figure 52: The squared modulus of the breakup S-matrix element as a function of k at the grazing total angular momentum $J = 43$ for ^{6}Li + ^{40}Ca scattering at 156 MeV. The solid line is by the pseudo-state method, while the bars by the momentum bin method with dense bins. (a) s-state breakup ($l = 0, L = 43$) and (b) d-state breakup ($l = 2, L = 41$); similar result is obtained for ($l = 2, L = 43, 45$). This figure is taken from [134].

9.2 Extention to four-body breakup processes

In this subsection, we discuss a feasibility of the pseudo-state CDCC for four-body breakup processes. Reactions induced by unstable nuclei composed of loosely bound three particles give important information on the structure of such nuclei. In principle, these reactions are to be treated as four-body breakup processes in theoretical studies. It is possible to extend the pseudo-state CDCC, in combination with GEM, to such processes.

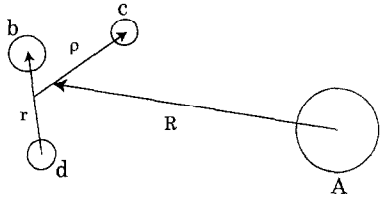

Figure 53: Illustration of a four-body (A+b+c+d) system in CDCC. Two other sets of Jacobian coordinates of the projectile (b+c+d) are omitted for simplicity.

The momentum bin method needs the exact (continuous) wave functions the three-body system which, in general, are quite hard to obtain. But, we can circumvent this problem with the pseudo-state method. In the method, it is possible to prepare the approximate three-body complete set of wave functions $\{\Phi_I^{(i)};\, i = 1 - i_{\max}\}$ by diagonalizing the Hamiltonian of the projectile in a space spanned by bases of L^2 type (see Section 3). Regarding $\{\Phi_I^{(i)}\}$ as the intrinsic wave functions of the breakup channels, we expand the total wave function $\Psi_{JM}^{\rm CDCC}$ in the same manner as Eq. (127) (Fig. 53):

$$\Psi_{JM}^{\rm CDCC} = \left[\Phi_{I_0}^{(0)}(\mathbf{r},\boldsymbol{\rho})\,\chi_{I_0L_0}^{(0)}(\mathbf{R})\right]_{JM} + \sum_{I=0}^{I_{\max}}\sum_{L}\sum_{i=1}^{i_{\max}}\left[\Phi_I^{(i)}(\mathbf{r},\boldsymbol{\rho})\,\chi_{IL}^{(i)}(\mathbf{R})\right]_{JM}. \tag{134}$$

Insertion of Eq. (134) into the four-body Schrödinger equation, $(H - E)\Psi_{JM} = 0$, leads to a set of coupled differential equations for $\chi_{I_0L_0}^{(0)}(R)$ and $\chi_{IL}^{(i)}(P_i, R)$. The diagonal and the coupling potentials

are given in the form

$$V_{iIL,i'I'L'}(R) = \langle \left[\Phi_I^{(i)}(\mathbf{r},\boldsymbol{\rho})Y_L(\widehat{\mathbf{R}})\right]_{JM} \mid U \mid \left[\Phi_{I'}^{(i')}(\mathbf{r},\boldsymbol{\rho})Y_{L'}(\widehat{\mathbf{R}})\right]_{JM} \rangle \,, \tag{135}$$

where U is the sum of the three optical potentials between the target nucleus and each of the particles in the three-body projectile. The asymptotic boundary condition for $\chi_{IL}^{(i)}(P_i, R)$ is the same as Eq. (129), generating the S-matrix elements $S_{IL,I_0L_0}^{(i)}$ to the pseudo-states $\Phi_I^{(i)}$.

From the S-matrix elements we can calculate the differential cross sections of the elastic scattering and projectile-inelastic scattering (projectile-breakup) to the pseudo-states $\Phi_I^{(i)}$. Experimental differential cross sections to breakup states is sometimes given as a sum of the cross sections for projectile continuum states within an energy interval. In such a case, the corresponding calculated cross section may be given as a sum of cross sections to pseudo-states in the same energy interval. Analysis of the effect of the virtual breakup of the projectile on the differential cross sections of the elastic scattering of ^{6}He$(=\alpha+n+n)$ and ^{11}Li$(=^9$Li$+n+n)$ projectiles is underway using the three-body GEM wave functions of the bound states and pseudo-states of those projectiles. Recent experimental data on ^{6}He scattering and ^{11}Li scattering are of particular interest. Very recently, Matsumoto *et al.* [137] reported a four-body CDCC analysis, for the first time. They analyzed elastic ^{6}He $+^{12}$ C scattering at $E_{\rm lab}$ = 38 MeV/nucleon; observed differential cross section was well reproduced by the calculation including the s-wave and d-wave three-body breakup pseudo-states of ^{6}He.

Explicit breakup T-matrix element can be calculated by inserting $\Psi^{\rm CDCC}$, in place of the exact total wave function, in the exact form of breakup T-matrix elements, which leads to an approximate form [134]

$$T_4 = \langle\, e^{i(\mathbf{P}\cdot\mathbf{R}+\mathbf{k}\cdot\mathbf{r}+\mathbf{q}\cdot\boldsymbol{\rho})} \mid U_4 \mid \Psi^{\rm CDCC} \,\rangle \,, \tag{136}$$

where U_4 is sum of all interactions in the four-body (A+b+c+x) system and $\mathbf{k}$ and $\mathbf{q}$ are momenta conjugate to $\mathbf{r}$ and $\boldsymbol{\rho}$, respectively. Accuracy of Eq. (136) depends on how precise the approximate complete set is within a finte region sensitive to T_4. Analyses based on this formulation are of much interest as a future work on breakup reactions induced by three-body unstable nuclei.

10 Summary

We have reviewed our method of calculation, Gaussian expansion method (GEM), for bound and scattering states of few-body systems and its applications to various subjects. Major points to be emphasized are as follows:

i) We introduced three types of basis functions for GEM: Gaussians, infinitesimally-shifted Gaussians and complex-range Gaussians in which range parameters are chosen to form geometric progression. As for two-body systems, we demonstrated that the former two types (mathematically equivalent to each other) were quite suitable for describing short-range correlations and long-range asymptotic behaviour simultaneously, while the third type was good at describing highly oscillatory wave functions of both bound and scattering states.

ii) Bound-state wave functions of three- and four-body systems are expanded in terms of a set of (complex-range) Gaussian basis functions of a set of Jacobian coordinates in each of all the rearrangement channels. This multi-channel representation makes the functional space much wider than that spanned by single-channel basis functions. Therefore, the multi-channel basis functions are particularly suitable for describing both the short-range correlations and the loose (halo-like) binding of any pair of particles in the system.

iii) With the use of the (complex-range) Gaussian basis functions, calculation of three- and four-body matrix elements between rearrangement channels can easily be performed for potentials with arbitrary shape. A technique of using the infinitesimally-shifted Gaussian basis functions in place of the Gaussian

basis functions is very powerful ! !and is used in all the four-body calculations described in this paper. Accuracy of the results has been demonstrated in a stringent benchmark test calculation for the four-nucleon bound state using a realistic NN interaction.

iv) An advantage of GEM is that the diagonalization of a Hamiltonian using the Gaussian basis functions generates not only the lowest eigenstate but also excited eigenstates with the same J^π simultaneously. For two-body systems, we found that the eigenstates (bound and discretized continuum states) form an approximate complete set in a finite but sufficiently large region of the coordinate space. The same is also true for the four nucleon system: a GEM calculation well explained the ground and the second 0^+ states of ^{4}He and demonstarted that the 0^+ eigenstates obtained by diagonalizing the four-body Hamiltonian exhausts 99.99 % of the energy-weighted monopole sum rule.

v) We took full advantage of GEM mentioned in ii) and iv) when we performed high-precision Coulomb three-body calculation of exotic atoms/molecules: (a) the very weakly bound $J = v = 1$ state of the $dt\mu$ molecule which is a key to the muon catalyzed d–t fusion, and (b) the metastable, vibrationally-excited states ($J \approx 35, v \lesssim 5$) in antiprotonic helium atoms ($\mathrm{He}^{2+} + e^- + \bar{p}$) observed by laser experiments. In the latter, the GEM calculation was so accurate as to become the first recommended value of antiproton mass cited in Particle Listings 2000 and the latest value in the 2002 edition.

vi) The advantage of iv) of GEM has been taken in a new treatment of breakup continuum in the method of CDCC (continuum-discretized coupled channels) for three-body nuclear reactions involving breakup proceses of weakly-bound projectiles (ejectiles) such as unstable nuclei. Continuum states of the projectile (ejectile) can properly be treated by the discretized eigenstates (pseudo states) obtained by GEM. Smoothing of discrete breakup S-matrix of CDCC into accurate continuous breakup S-matrix becomes possible by the treatment. The CDCC calculation of elastic scattering of ^{6}He ($= \alpha + n + n$), a typical three-body halo nucleus, with its virtual three-body breakup states taken into account, is now feasible using the techniques of this paper; differential cross section of ^{6}He+^{12}C at $E_{\mathrm{lab}}/A = 38$ MeV is found to be well reproduced by this 'four-body' CDCC.

vii) Application of GEM is possible to low-energy Coulomb three-body reactions based on the same idea as in vi). Examples were presented for muon transfer reactions and the decay of Feshbach-type muon molecular resonances. The three-body scattering wave function was given by a sum of two components; one for (rearrangement) open channels and the other for closed channels. The latter L^2 integrable component was presented as a superposition of three-body eigenstates which were obtained by diagonalizing the total Hamiltonian using the three-body Gaussian basis functions of all the rearrangement Jacobian coordinates. The eigenfunctions constituted an approximate complete set in a finite coordinate space. The calculated results agreed with those obtained by completely different methods, which showed that GEM is valid at least in some cases of Coulomb three-body reactions .

viii) Studies of light hypernuclei based on three- and four-body (cluster) models have been quite useful in constraining ambiguities of hyperon(Y)-nucleon(N) and hypron(Y)-hyperon(Y) interactions for which information from scattering experiments is scarce (YN) and none (YY). Good examples are as follows. The spin-orbit splitting energies in ${}^{9}_{\Lambda}\mathrm{Be}(= 2\alpha+\Lambda)$ and ${}^{13}_{\Lambda}\mathrm{C}(= 3\alpha+\Lambda)$ predicted with a quark-model-based YN spin-orbit force agreed with the energies given by later γ spectroscopy experiments, whereas those predicted with the meson-theory-based YN spin-orbit force was several times larger than the observed values. Regarding the YY interactions, a $\Lambda\Lambda$ potential designed to fit the 2Λ separation energy, $B_{\Lambda\Lambda}$, of ${}^{6}_{\Lambda\Lambda}\mathrm{He}$ (NAGARA event) was found to reproduce $B_{\Lambda\Lambda}$ of the 2^+ excited state of ${}^{10}_{\Lambda\Lambda}\mathrm{Be}$ (*Demachi-Yanagi* event) consistently. With the same $\Lambda\Lambda$ potential, energy levels of double Λ hypernuclei with $A = 7 - 10$ were prectited to be compared with future experiments for further studies of the YY interaction. A definitely important role of $\Lambda - \Sigma$ conversion in ${}^{4}_{\Lambda}\mathrm{H}$ (${}^{4}_{\Lambda}\mathrm{He}$) were made clear using a $(3N + \Lambda) + (3N + \Sigma)$ four-body model with realistic NN and YN interactions.

ix) Some of light hypernuclei were found to show significant dynamical change by addition of Λ particle(s) to them. This phenomena is well described by three- and four-body (cluster) model of single and

double Λ hypernuclei. A significant shrinkage (22 %) of the core nucleus of ${}^{7}_{\Lambda}$Li was predicted, together with a suggestion of how to determine it. The prediction was afterwards verified experimentally (19 ± 4 %). Addition of Λ particle(s) makes the core nucleus more stable and extends the neutron drip line in the nuclear chart and gives rise to many 'neutron-lich' hypernuclei. Level structure of some of such neutron-lich hyper nuclei was predicted.

Acknowledgements

The authors would like to thank M. Kawai for valuable discussions and careful reading of the manuscript. They are grateful to K. Ikeda, T. Motoba, Y. Yamamoto, T. Yamada, H. Kudo, M. Yahiro and R.C. Johnson for helpful discussions and encouragement. One of the authors (E.H.) is thankful to B.F. Gibson for warm hospitality during her stay at LANL to prepare this manuscript and for careful reading of it. Thanks are also due to K. Ogata, S. Otsubo, T. Matsumoto and Y. Toya for their help in preparation of this manuscript. This work was supported by the Grant-in-Aid for Scientific Reseach of Monbukagakushou of Japan. One of the authors (E.H.) would like to acknowledge a support from the Yamada Science Foundation.

Appendix

In Appendix, we shall describe some technical details of Gaussian and infinitesimally-shifted Gaussian basis functions. In Appendix A.1, the calculational method for three-body matrix elements is presented. Appendix A.2 explains how to construct the infinitesimally-shefted Gaussian basis functions. Calculational methods for three-body and four-body matrix elements with the infinitesimally-shifted Gaussian basis functions are provided in Appendix A.3 and A.4, respectively.

A.1 Three-body matrix elements using the Gaussian basis functions

We outline the calculation of matrix elements using three-body Gaussian basis functions which appear in Section 3. Spin and isospin parts are omitted for simplicity of expressions.

Interaction potentials

As an example, we consider how to calculate a central-potential matrix element of the following type:

$$\left\langle \left[\phi^{\rm G}_{n_a l_a}(\mathbf{r}_a)\, \psi^{\rm G}_{N_a L_a}(\mathbf{R}_a) \right]_{JM} \middle| V(r_c) \middle| \left[\phi^{\rm G}_{n_b l_b}(\mathbf{r}_b)\, \psi^{\rm G}_{N_b L_b}(\mathbf{R}_b) \right]_{JM} \right\rangle \tag{137}$$

in which the ket- and bra-vectors are from different channels a and $b\,(a \neq b)$ and the potential is a function of r_c, $(c \neq a, c \neq b)$. We transform both the a-channel and b-channel functions into c-channel functions and to perform the integration over $\mathbf{r}_c$ and $\mathbf{R}_c$.

Assuming the coordinate transformation $(\mathbf{r}_a, \mathbf{R}_a), (\mathbf{r}_b, \mathbf{R}_b) \rightarrow (\mathbf{r}_c, \mathbf{R}_c)$ in the form

$$\begin{aligned} \mathbf{r}_a &= \alpha_{ac}\mathbf{r}_c + \beta_{ac}\mathbf{R}_c\,, \qquad \mathbf{R}_a = \gamma_{ac}\mathbf{r}_c + \delta_{ac}\mathbf{R}_c\,, \\ \mathbf{r}_b &= \alpha_{bc}\mathbf{r}_c + \beta_{bc}\mathbf{R}_c\,, \qquad \mathbf{R}_b = \gamma_{bc}\mathbf{r}_c + \delta_{bc}\mathbf{R}_c \end{aligned} \tag{138}$$

and using the formula

$$r_a^l\, Y_{lm}(\hat{\mathbf{r}}_a) = \sum_{\lambda=0}^{l} \left[\frac{4\pi(2l+1)!}{(2\lambda+1)!(2(l-\lambda)+1)!} \right]^{\frac{1}{2}} (\alpha_{ac} r_c)^{l-\lambda} (\beta_{ac} R_c)^{\lambda} \left[Y_\lambda(\hat{\mathbf{r}}_c) Y_{l-\lambda}(\widehat{\mathbf{R}}_c) \right]_{lm} \tag{139}$$

we can rewrite the a-channel three-body basis function as a function of $\mathbf{r}_c$ and $\mathbf{R}_c$:

$$r_a^{l_a} R_a^{L_a} \left[Y_{l_a}(\hat{\mathbf{r}}_a) Y_{L_a}(\widehat{\mathbf{R}}_a) \right]_{JM}$$

$$= (2l_a+1)(2L_a+1)\sum_{\lambda=0}^{l_a}\sum_{\Lambda=0}^{L_a}\left[\binom{2l_a}{2\lambda}\binom{2L_a}{2\Lambda}\right]^{\frac{1}{2}} \alpha_{ac}^{l_a-\lambda}\,\beta_{ac}^{\lambda}\,\gamma_{ac}^{L_a-\Lambda}\,\delta_{ac}^{\Lambda}\,r_c^{l_a+L_a-(\lambda+\Lambda)}\,R_c^{\lambda+\Lambda}$$
$$\times \sum_{l_c,L_c}\begin{Bmatrix} l_a-\lambda & L_a-\Lambda & l_c \\ \lambda & \Lambda & L_c \\ l_a & L_a & J \end{Bmatrix}(l_a-\lambda\, L_a-\Lambda\, 0\,0\,|\,l_c\,0)(\lambda\,\Lambda\,0\,0\,|\,L_c\,0)\left[Y_{l_c}(\hat{\mathbf{r}}_c)Y_{L_c}(\widehat{\mathbf{R}}_c)\right]_{JM} \quad (140)$$

This expression can be summarized in the form (denoting $\lambda+\Lambda$ as K)

$$r_a^{l_a}R_a^{L_a}\left[Y_{l_a}(\hat{\mathbf{r}}_a)Y_{L_a}(\widehat{\mathbf{R}}_a)\right]_{JM} = \sum_{l_c,L_c}\sum_{K=0}^{l_a+L_a}\langle l_a\,L_a\,J\,|\,l_c\,L_c\,K\,J\rangle_{a\to c}\,r_c^{l_a+L_a-K}\,R_c^{K}\,\left[Y_{l_c}(\hat{\mathbf{r}}_c)Y_{L_c}(\widehat{\mathbf{R}}_c)\right]_{JM} \quad (141)$$

and the transformation coefficients $\langle l_a\,L_a\,J\,|\,l_c\,L_c\,K\,J\rangle_{a\to c}$ can be calculated and stored prior to the computation. The same transformation can be made for the b-channel basis function as

$$r_b^{l_b}R_b^{L_b}\left[Y_{l_b}(\hat{\mathbf{r}}_b)Y_{L_b}(\widehat{\mathbf{R}}_b)\right]_{JM} = \sum_{l_c,L_c}\sum_{K=0}^{l_b+L_b}\langle l_b\,L_b\,J\,|\,l_c\,L_c\,K\,J\rangle_{b\to c}\,r_c^{l_b+L_b-K}\,R_c^{K}\,\left[Y_{l_c}(\hat{\mathbf{r}}_c)Y_{L_c}(\widehat{\mathbf{R}}_c)\right]_{JM} \quad (142)$$

Using the coordinate relations in Eq.(138), the remaining Gaussian part can be transformed as

$$e^{-\nu_a r_a^2-\lambda_a R_a^2}\,e^{-\nu_b r_b^2-\lambda_b R_b^2} = e^{-\eta r_c^2-2\xi\,\mathbf{r}_c\cdot\mathbf{R}_c-\zeta R_c^2} = e^{-\eta r_c^2-\zeta R_c^2}\sum_{l=0}^{\infty}4\pi\sqrt{2l+1}\,\mathcal{I}_l(2\xi r_c R_c)\left[Y_l(\hat{\mathbf{r}}_c)Y_l(\widehat{\mathbf{R}}_c)\right]_0 \quad (143)$$

where $\mathcal{I}_l(z)$ is the modified Bessel function, $\mathcal{I}_l(z) = (-i)^l j_l(iz)$.

Combining Eqs. (141),(142) and (143), we are ready to perform the integration in Eq.(137) over $\mathbf{r}_c$ and $\mathbf{R}_c$. The integrations over $\mathbf{R}_c$ and then over $\hat{\mathbf{r}}_c$ can be performed analytically after some angular-momentum algebra though the result is not written here explicitly.

Numerical integration of an arbitray $V(r_c)$

We are finally left with a one-dimensional radial integration in the form

$$V_m = \int_0^\infty r_c^{2m}\,e^{-\alpha r_c^2}\,V(r_c)\,r_c^2\,dr \qquad (0 \le m \le (l_a+L_a+l_b+L_b)/2,\ \alpha>0)\,, \quad (144)$$

where α depends on the Gaussian sizes (ν_{n_a}, λ_{N_a}, ν_{n_b}, λ_{N_b}) and the coordinate transformation coefficients (α_{ac}, β_{ac}, γ_{ac}, δ_{ac}, α_{bc}, β_{bc}, γ_{bc}, δ_{bc}). $(l_a+L_a+l_b+L_b)/2$ is an integer because of the parities $(-)^{l_a+L_a} = (-)^{l_b+L_b}$. When numerical integration of Eq.(144) is necessary for a specific $V(r_c)$, it is time consuming to perform for each combination of basis functions, especially in the case of a large dimensional matrix.

For an arbitrary shape of $V(r_c)$, the authors recommend the following interpolation technique which requires only a short computation time but keeps a high accuracy (this is an advantage of taking the Gaussian basis functions): Since V_m is a smooth function of $\log\alpha$ for any m, third-order (cubic) interpolation with respect to $\log\alpha$ is satisfactory. First, estimate the possible minimum and maximum of $\log\alpha$ using the shortest and longest ranges of Gaussians and calculate the integral Eq.(144) for $\{(\log\alpha)_n; n=1-N\}$, N being the number of equidistant grid points. High accuracy, say 10^{-10}, in the interpolation is accomplished with a few thousand points for which the computation time in preparing the integration is negligible; the radial integrand can be accurately done with the Gauss quadrature.

Other matrix elements

Three-body matrix elements of the norm-overlap and those of the kinetic-energy operator are much easier by simply transforming the a-channel basis functions into the b-channel functions by Eq.(141) (or from the b-channel to the c-channel).

Matrix elements of non-central forces are more tedious but straightforward, though explicit results are not shown in this paper. In the study of three-nucleon bound states (^{3}H and ^{3}He) based on the present method using realistic NN forces [63], the non-central forces employed are the spin-orbit, tensor, l^2, quadratic spin-orbit and momentum-dependent forces as well as the Tuson-Melbourne three-body force [64] (See Section 3).

A.2 Construction of the infinitesimally shifted Gaussian basis functions

The infinitesimally-shifted Gaussian (ISG) basis functions are generated in the following way. As an example, we give the ISG function which is equivalent to the p-wave ($l = 1, m = 0$) one-body Gaussian function

$$ze^{-\nu r^2} = \lim_{\varepsilon\to 0} \frac{1}{4\varepsilon\nu} e^{-\nu(x^2+y^2)}[e^{-\nu(z-\varepsilon)^2} - e^{-\nu(z+\varepsilon)^2}], \tag{145}$$

where ε is the shifted distance of the Gaussian. The term in [ ] can be written as

$$e^{-\nu(z-\varepsilon)^2} - e^{-\nu(z+\varepsilon)^2} = e^{\nu(z^2+\varepsilon^2)}\left[e^{2\nu\varepsilon z} - e^{-2\nu\varepsilon z}\right] = e^{\nu(z^2+\varepsilon^2)}\left[4\varepsilon\nu z + \frac{2}{3}(2\varepsilon\nu z)^3 + \cdots\cdots\right]. \tag{146}$$

and the RHS of Eq. (145) converges to the LHS for $\varepsilon \to 0$. The procedure $\varepsilon \to 0$ in actual calculations is to be performed after the analytical calculation of the matrix elements, as was emphasized in Sections 2.6.

More generally, we have the following expression:

$$(\mathbf{a}\cdot\mathbf{r})^n\, e^{-\nu r^2} = \lim_{\varepsilon\to 0} \left(\frac{n}{4\varepsilon\nu}\right)^n \left[e^{-\frac{\nu}{n}(\mathbf{r}-\varepsilon\mathbf{a})^2} - e^{-\frac{\nu}{n}(\mathbf{r}+\varepsilon\mathbf{a})^2}\right]^n, \tag{147}$$

where, $\mathbf{a}$ is a dimensionless vector to indicate the shift direction (ε has the dimension of length). With respect to ε, the leading-order term of the quantity [ ]^n is $(4\nu\varepsilon/n)^n(\mathbf{a}\cdot\mathbf{r})^n e^{-\nu r^2}$ and all the lower-order terms vanish. We define three shift vectors $\mathbf{a}_z$, $\mathbf{a}_{xy}$ and $\mathbf{a}^*_{xy}$ as

$$\mathbf{a}\cdot\mathbf{r} = \begin{cases} z & \text{for} \quad \mathbf{a} = \mathbf{a}_z \equiv (0,0,1) \\ x+iy & \text{for} \quad \mathbf{a} = \mathbf{a}_{xy} \equiv (1,i,0) \\ x-iy & \text{for} \quad \mathbf{a} = \mathbf{a}^*_{xy} \equiv (1,-i,0) \end{cases} \tag{148}$$

and use them below in the definition of the ISG basis functions. The spherical harmonics $Y_{lm}(\theta\phi)$ multiplied by r^l are described in term of cartesian coordinates as follows (for $m > 0$):

$$\begin{aligned} r^l Y_{lm}(\theta,\phi) &= \left[\frac{(2l+1)(l-m)!}{4\pi(l+m)!}\right]^{\frac{1}{2}} r^l P_l^m(\cos\theta) e^{im\phi} \\ &= \left[\frac{(2l+1)(l-m)!}{4\pi(l+m)!}\right]^{\frac{1}{2}} \frac{(l+m)!}{2^m} r^l (\sin\theta\, e^{i\phi})^m \sum_{j=0}^{[\frac{l-m}{2}]} \frac{(-)^j \cos^{l-m-2j}\theta \sin^{2j}\theta}{4^j\, j!(m+j)!(l-m-2j)!} \\ &= (x+iy)^m \sum_{j=0}^{[\frac{l-m}{2}]} A_{lm,j}\, z^{l-m-2j}\, (x^2+y^2)^j \\ &= \sum_{j=0}^{[\frac{l-m}{2}]} A_{lm,j}\, z^{l-m-2j}\, (x+iy)^{m+j}\, (x-iy)^j \end{aligned} \tag{149}$$

with

$$A_{lm,j} = \left[\frac{(2l+1)(l-m)!}{4\pi(l+m)!}\right]^{\frac{1}{2}} \frac{(l+m)!}{2^m} \frac{(-)^j}{4^j\, j!(m+j)!(l-m-2j)!}\,. \tag{150}$$

Using the trivial relation ($l \neq 0$)

$$z^{l-m-2j}\, (x+iy)^{m+j}\, (x-iy)^j\, e^{-\nu r^2} = [(\mathbf{a_z}\cdot\mathbf{r})\, e^{-\frac{\nu}{l}r^2}]^{l-m-2j}\, [(\mathbf{a_{xy}}\cdot\mathbf{r})\, e^{-\frac{\nu}{l}r^2}]^{m+j}\, [(\mathbf{a^*_{xy}}\cdot\mathbf{r})\, e^{-\frac{\nu}{l}r^2}]^j. \tag{151}$$

and replacing ν with $\nu n/l$ in Eq. (147), we have an alternative expression for the normalized Gaussian basis function Eq. (7) in the following form:

$$\begin{aligned}\phi^{\rm G}_{lm}(\mathbf{r}) &= N_{\nu l}\, r^l e^{-\nu r^2} Y_{lm}(\hat{\mathbf{r}}) \\ &= N_{\nu l} \lim_{\varepsilon\to 0} \left(\frac{l}{4\nu\varepsilon}\right)^l \sum_{j=0}^{[\frac{l-m}{2}]} A_{lm,j} \left[e^{-\frac{\nu}{l}(\mathbf{r}-\varepsilon\mathbf{a}_z)^2} - e^{-\frac{\nu}{l}(\mathbf{r}+\varepsilon\mathbf{a}_z)^2}\right]^{l-m-2j} \\ &\times \left[e^{-\frac{\nu}{l}(\mathbf{r}-\varepsilon\mathbf{a}_{xy})^2} - e^{-\frac{\nu}{l}(\mathbf{r}+\varepsilon\mathbf{a}_{xy})^2}\right]^{m+j} \left[e^{-\frac{\nu}{l}(\mathbf{r}-\varepsilon\mathbf{a}^*_{xy})^2} - e^{-\frac{\nu}{l}(\mathbf{r}+\varepsilon\mathbf{a}^*_{xy})^2}\right]^j . \end{aligned} \tag{152}$$

Expanding the [ ] terms we can rewrite the above equation (introducing $p = l-m-2j$ and $q = m+j$) as

$$N_{\nu l}\, r^l e^{-\nu r^2} Y_{lm}(\hat{\mathbf{r}}) = N_{\nu l} \lim_{\varepsilon\to 0} \left(\frac{l}{4\nu\varepsilon}\right)^l \sum_{j=0}^{[\frac{l-m}{2}]} A_{lm,j}\, r^{-\nu r^2} \sum_{s=0}^{p} \binom{p}{s} e^{2(2s-p)\,\varepsilon\,\nu\,\mathbf{a}_z\cdot\mathbf{r}/l} \tag{153}$$

$$\times \sum_{t=0}^{q} \binom{q}{t} e^{2(2t-q)\,\varepsilon\,\nu\,\mathbf{a}_{xy}\cdot\mathbf{r}/l} \sum_{u=0}^{j} \binom{j}{u} e^{2(2u-j)\,\varepsilon\,\nu\,\mathbf{a}^*_{xy}\cdot\mathbf{r}/l} \tag{154}$$

$$= N_{\nu l} \lim_{\varepsilon\to 0} \left(\frac{l}{4\nu\varepsilon}\right)^l \sum_{j=0}^{[\frac{l-m}{2}]} A_{lm,j} \sum_{s=0}^{p}\sum_{t=0}^{q}\sum_{u=0}^{j} \binom{p}{s}\binom{q}{t}\binom{j}{u} e^{-\nu(\mathbf{r}-\varepsilon\mathbf{D})^2} \tag{155}$$

with

$$p = l-m-2j\,, \qquad q = l+m \tag{156}$$

$$\mathbf{D} = (2/l)\,[\,(2s-p)\,\mathbf{a_z} + (2t-q)\,\mathbf{a_{xy}} + (2u-j)\,\mathbf{a^*_{xy}}\,] \tag{157}$$

Here, we have neglected the effect of the $\mathcal{O}(\varepsilon^2)$ terms in the argument of the exponential functions.

Equation (155) gives connecting with the Gaussian basis functions $\phi^{\rm G}_{nl}(r)$ defined by Eqs.(7), (8) and (9) in the form

$$\begin{aligned}\phi^{\rm G}_{nlm}(\mathbf{r}) &= N_{nl}\, r^l e^{-\nu_n r^2} Y_{lm}(\hat{\mathbf{r}}) \\ &= N_{nl} \lim_{\varepsilon\to 0} \frac{1}{(\nu\varepsilon)^l} \sum_{k=1}^{k_{\max}} C_{lm,k}\, e^{-\nu_n(\mathbf{r}-\varepsilon\mathbf{D}_{lm,k})^2} \end{aligned} \tag{158}$$

with

$$C_{l-m,k} = (-)^m C_{lm,k}\,, \qquad \mathbf{D}_{l-m,k} = \mathbf{D}^*_{lm,k}\,. \tag{159}$$

The coefficients $C_{lm,k}$ and the shift-direction vector $\mathbf{D}_{lm,k}$ are dimensionless numbers ndependent of ν and ε. $C_{lm,k}$ and the x- and z-components of $\mathbf{D}_{lm,k}$ are real numbers. The y-component of $\mathbf{D}_{lm,k}$ is purely imaginary. With this in mind, one can treat the $\mathbf{D}_{lm,k}$ with no explicit use of complex variables in the computation. It is to be noted that the choice of the shift-direction vectors is not unique, though the final result of the matrix element calculation is the same. For example, we can take $\mathbf{a}_x \equiv (1,0,0)$, $\mathbf{a}_y \equiv (0,1,0)$ and $\mathbf{a}_z \equiv (0,0,1)$ and make a similar calculation as above resulting in another set of $\{C_{lm,k}, \mathbf{D}_{lm,k}\,;\ k = 1-k_{\max}\}$ with $k_{\max}$ becoming slightly larger and $C_{lm,k}$ being complex, but use of this set is mathematically equivalent to Eq. (158).

Here again, $(\nu\varepsilon r)^l$ is the leading order of the summed quantity in Eq. (158) and is canceled by $1/(\nu\varepsilon)^l$ leaving r^l; the lower-order terms vanish through the summation and the terms of higher order than $(\nu\varepsilon r)^l$ disappear after $\varepsilon \to 0$. This property is the key advantage of the present method and is often used in the calculations below.

A.3 Three-body matrix elements using infinitesimally-shifted Gaussian basis functions

We outlined in Appendix A.1 how to calculate the energy matrix elements using three-body Gaussian basis functions Eq.(137). The angular-momentum algebra (Racah algebra) to perform the integration

over all anglular coordinates is straightforward but rather tedious, especially in the case of complicated interactions. Also, the algebra will be much more laborious for four-body systems. Use of the infinitesimally-shifted Gaussian (ISG) basis functions makes such a calculation very easy with no tedious angular-momentum algebra required. An outline of this calculation is given in this section. We note that Suzuki and Varga utilized [72] another method for matrix calculations using Gaussian functions.

In the calculation of the matrix element Eq.(137), Gaussian basis functions $\phi^{\rm G}_{nlm}(\mathbf{r})$ and $\psi^{\rm G}_{NLM}(\mathbf{R})$ are replaced by the mathematically equivalent ISG functions, Eq.(158):

$$\phi^{\rm G}_{nlm}(\mathbf{r}) = N_{nl} \lim_{\varepsilon\to 0} \frac{1}{(\nu\varepsilon)^l} \sum_{k=1}^{k_{\max}} C_{lm,k}\, e^{-\nu_n(\mathbf{r}-\varepsilon\mathbf{D}_{lm,k})^2}, \tag{160}$$

$$\phi^{\rm G}_{NLM}(\mathbf{R}) = N_{NL} \lim_{\varepsilon\to 0} \frac{1}{(\lambda\varepsilon)^L} \sum_{K=1}^{K_{\max}} C_{LM,K}\, e^{-\lambda_N(\mathbf{R}-\varepsilon\mathbf{D}_{LM,K})^2}. \tag{161}$$

The matrix element in Eq.(137) can then be written down explicitly in the form

$$\begin{aligned}
&\left\langle \left[\phi^{\rm G}_{n_a l_a}(\mathbf{r}_a)\,\psi^{\rm G}_{N_a L_a}(\mathbf{R}_a)\right]_{JM} | V(r_c) | \left[\phi^{\rm G}_{n_b l_b}(\mathbf{r}_b)\,\psi^{\rm G}_{N_b L_b}(\mathbf{R}_b)\right]_{JM} \right\rangle \\
&= N_{n_a l_a} N_{N_a L_a} N_{n_b l_b} N_{N_b L_b} \sum_{m_a M_a} (l_a m_a L_a M_a | JM) \sum_{m_b M_b} (l_b m_b L_b M_b | JM) \\
&\times \lim_{\varepsilon_a\to 0} \frac{1}{(\nu_{n_a}\varepsilon_a)^{l_a}} \lim_{\varepsilon_A\to 0} \frac{1}{(\lambda_{N_a}\varepsilon_A)^{L_a}} \lim_{\varepsilon_b\to 0} \frac{1}{(\nu_{n_b}\varepsilon_b)^{l_b}} \lim_{\varepsilon_B\to 0} \frac{1}{(\lambda_{N_b}\varepsilon_B)^{L_b}} \\
&\times \sum_{k_a}\sum_{K_a}\sum_{k_b}\sum_{K_b} C_{l_a m_a,k_a}\, C_{L_a M_a,K_a}\, C_{l_b m_b,k_b}\, C_{L_b M_b,K_b} \langle\, V(r_c)\,\rangle_{\mathbf{r}_c,\mathbf{R}_c}
\end{aligned} \tag{162}$$

$$\begin{aligned}
&\langle\, V(r_c)\,\rangle_{\mathbf{r}_c,\mathbf{R}_c} \\
&\equiv \left\langle e^{-\nu_{n_a}(\mathbf{r}_a-\varepsilon_a\mathbf{D}_{l_a m_a,k_a})^2} e^{-\lambda_{N_a}(\mathbf{R}_a-\varepsilon_A\mathbf{D}_{L_a M_a,K_a})^2} | V(r_c) | e^{-\nu_{n_b}(\mathbf{r}_b-\varepsilon_b\mathbf{D}_{l_b m_b,k_b})^2} e^{-\lambda_{N_b}(\mathbf{R}_b-\varepsilon_B\mathbf{D}_{L_b M_b,K_b})^2} \right\rangle_{\mathbf{r}_c,\mathbf{R}_c}.
\end{aligned} \tag{163}$$

The coordinate transformation $(\mathbf{r}_a,\mathbf{R}_a),(\mathbf{r}_b,\mathbf{R}_b)\to(\mathbf{r}_c,\mathbf{R}_c)$ in Eq.(138) is simply performed within the arguments of the Gaussians of Eq.(163); this is an advantage of the ISG basis functions.

For simplicity in the expressions below, the following definitions are introduced.

$$\varepsilon_1=\varepsilon_a,\quad \varepsilon_2=\varepsilon_A,\quad \varepsilon_3=\varepsilon_b,\quad \varepsilon_4=\varepsilon_B, \tag{164}$$

$$\mathbf{D}_1=\mathbf{D}^*_{l_a m_a,k_a},\quad \mathbf{D}_2=\mathbf{D}^*_{L_a M_a,K_a},\quad \mathbf{D}_3=\mathbf{D}_{l_b m_b,k_b},\quad \mathbf{D}_4=\mathbf{D}_{L_b M_b,K_b}, \tag{165}$$

$$L^{(\rm sum)}=(l_a+L_a+l_b+L_b)/2. \tag{166}$$

where $(l_a+L_a+l_b+L_b)/2$ is an integer because of the pary relation $(-)^{l_a+L_a}=(-)^{l_b+L_b}$.

Gaussian potential

In the case of a Gaussian potential, $V(r_c)=v_0\,e^{-\mu r_c^2}$, Eq. (163) is easily evaluated and can be represented in the form

$$\langle\, V(r_c)\,\rangle_{\mathbf{r}_c,\mathbf{R}_c} = G_{ab}\exp\Big(\sum_{1=i<j}^{4} g_{ij}\varepsilon_i\varepsilon_j\mathbf{D}_i\cdot\mathbf{D}_j\Big) \tag{167}$$

where the terms of $\{\mathcal{O}(\varepsilon_i^2); i=1-4\}$ are already dropped in the argument of the Gaussian since they are of no use. Though not explicitly given, the factors G_{ab} and g_{ij} depend on the Gaussian sizes $(\nu_{n_a},\lambda_{N_a},\nu_{n_b},\lambda_{N_b})$, the coordinate transformation coefficients $(\alpha_{ac},\beta_{ac},\gamma_{ac},\delta_{ac},\alpha_{bc},\beta_{bc},\gamma_{bc},\delta_{bc})$ and the potential parameters (v_0,μ), but not on the shift parameters.

In the same manner as in Section 2.6, we expand Eq. (167) in terms of ε's and retain only the terms proportional to $\varepsilon_1^{l_a}\varepsilon_2^{L_a}\varepsilon_3^{l_b}\varepsilon_4^{L_b}$. This is accomplished by the following three steps: Firstly, in the expansion of the exponential function, we take only the term

$$G_{ab}\Big(\sum_{1=i<j}^{4} g_{ij}\varepsilon_i\varepsilon_j\mathbf{D}_i\cdot\mathbf{D}_j\Big)^{L^{(\rm sum)}}/L^{(\rm sum)}! \tag{168}$$

since only this term includes the order of $\varepsilon_1^{l_a}\,\varepsilon_2^{L_a}\,\varepsilon_3^{l_b}\,\varepsilon_4^{L_b}$. Secondly, we expand Eq.(168) as

$$G_{ab}\prod_{1=i<j}^{4}\sum_{m_{ij}=0}^{L^{(\mathrm{sum})}}\frac{1}{m_{ij}!}\,(g_{ij}\varepsilon_i\,\varepsilon_j\mathbf{D}_i\cdot\mathbf{D}_j)^{m_{ij}} \tag{169}$$

imposing the constraint

$$\sum_{1=i<j}^{4} m_{ij}=L^{(\mathrm{sum})}\,. \tag{170}$$

Thirdly, in the summation in Eq. (169), we pick up only the terms which satisfy the relation about the powers of ε's:

$$\varepsilon_1^{m_{12}+m_{13}+m_{14}}=\varepsilon_1^{l_a},\quad \varepsilon_2^{m_{12}+m_{23}+m_{24}}=\varepsilon_2^{L_a},\quad \varepsilon_3^{m_{13}+m_{23}+m_{34}}=\varepsilon_3^{l_b},\quad \varepsilon_4^{m_{13}+m_{23}+m_{34}}=\varepsilon_4^{L_b}\,. \tag{171}$$

As the result of these three steps, Eq. (162) can be represented in the form

$$\begin{aligned}
&\Big\langle\Big[\phi^{\mathrm{G}}_{n_al_a}(\mathbf{r}_a)\,\psi^{\mathrm{G}}_{N_aL_a}(\mathbf{R}_a)\Big]_{JM}\,|\,V(r_c)\,|\,\Big[\phi^{\mathrm{G}}_{n_bl_b}(\mathbf{r}_b)\,\psi^{\mathrm{G}}_{N_bL_b}(\mathbf{R}_b)\Big]_{JM}\Big\rangle\\
&=N_{n_al_a}\,N_{N_aL_a}\,N_{n_bl_b}\,N_{N_bL_b}\,G_{ab}\,/(\nu_{n_a}^{l_a}\lambda_{N_a}^{L_a}\nu_{n_b}^{l_b}\lambda_{N_b}^{L_b})\\
&\times\sum_{m_aM_a}(l_am_aL_aM_a|JM)\sum_{m_bM_b}(l_bm_bL_bM_b|JM)\\
&\times\sum_{k_a}\sum_{K_a}\sum_{k_b}\sum_{K_b}C_{l_am_a,k_a}\,C_{L_aM_a,K_a}\,C_{l_bm_b,k_b}\,C_{L_bM_b,K_b}\\
&\times\sum_{m_{12}}\sum_{m_{13}}\sum_{m_{14}}\sum_{m_{23}}\sum_{m_{24}}\sum_{m_{34}}\frac{1}{m_{12}!\,m_{13}!\,m_{14}!\,m_{23}!\,m_{24}!\,m_{34}!}\\
&\times(\mathbf{D}_1\cdot\mathbf{D}_2)^{m_{12}}(\mathbf{D}_1\cdot\mathbf{D}_3)^{m_{13}}(\mathbf{D}_1\cdot\mathbf{D}_4)^{m_{14}}(\mathbf{D}_2\cdot\mathbf{D}_3)^{m_{23}}(\mathbf{D}_2\cdot\mathbf{D}_4)^{m_{24}}(\mathbf{D}_3\cdot\mathbf{D}_4)^{m_{34}}\\
&\times\delta_{m_{12}+m_{13}+m_{14}\,,\,l_a}\,\delta_{m_{12}+m_{23}+m_{24}\,,\,L_a}\,\delta_{m_{13}+m_{23}+m_{34}\,,\,l_b}\,\delta_{m_{14}+m_{24}+m_{34}\,,\,L_b}\\
&\times g_{12}^{m_{12}}\,g_{13}^{m_{13}}\,g_{14}^{m_{14}}\,g_{23}^{m_{23}}\,g_{24}^{m_{24}}\,g_{34}^{m_{34}}\,.
\end{aligned} \tag{172}$$

We then sum up the coefficients that are associated with the same powers of g_{ij}'s:

$$g_{12}^{m_{12}}\,g_{13}^{m_{13}}\,g_{14}^{m_{14}}\,g_{23}^{m_{23}}\,g_{24}^{m_{24}}\,g_{34}^{m_{34}}\,. \tag{173}$$

The result can be summarized in the following form, which is much more useful for rapid computation:

$$\begin{aligned}
&\Big\langle\Big[\phi^{\mathrm{G}}_{n_al_a}(\mathbf{r}_a)\,\psi^{\mathrm{G}}_{N_aL_a}(\mathbf{R}_a)\Big]_{JM}\,|\,V(r_c)\,|\,\Big[\phi^{\mathrm{G}}_{n_bl_b}(\mathbf{r}_b)\,\psi^{\mathrm{G}}_{N_bL_b}(\mathbf{R}_b)\Big]_{JM}\Big\rangle\\
&=N_{n_al_a}\,N_{N_aL_a}\,N_{n_bl_b}\,N_{N_bL_b}\,G_{ab}\,/(\nu_{n_a}^{l_a}\lambda_{N_a}^{L_a}\nu_{n_b}^{l_b}\lambda_{N_b}^{L_b})\\
&\times\sum_{i=1}^{i_{\max}}S^J_{l_a,L_a,l_b,L_b}(\,m_{12}^{(i)},m_{13}^{(i)},m_{14}^{(i)},m_{23}^{(i)},m_{24}^{(i)},m_{34}^{(i)}\,)\\
&\times g_{12}^{m_{12}^{(i)}}\,g_{13}^{m_{13}^{(i)}}\,g_{14}^{m_{14}^{(i)}}\,g_{23}^{m_{23}^{(i)}}\,g_{24}^{m_{24}^{(i)}}\,g_{34}^{m_{34}^{(i)}}\,,
\end{aligned} \tag{174}$$

with

$$\begin{aligned}
&S^J_{l_a,L_a,l_b,L_b}(\,m_{12}^{(i)},m_{13}^{(i)},m_{14}^{(i)},m_{23}^{(i)},m_{24}^{(i)},m_{34}^{(i)}\,)\\
&=\sum_{m_aM_a}(l_am_aL_aM_a|JM)\sum_{m_bM_b}(l_bm_bL_bM_b|JM)\\
&\times\sum_{k_a}\sum_{K_a}\sum_{k_b}\sum_{K_b}C_{l_am_a,k_a}\,C_{L_aM_a,K_a}\,C_{l_bm_b,k_b}\,C_{L_bM_b,K_b}\\
&\times\sum_{m_{12}}\sum_{m_{13}}\sum_{m_{14}}\sum_{m_{23}}\sum_{m_{24}}\sum_{m_{34}}\frac{1}{m_{12}!\,m_{13}!\,m_{14}!\,m_{23}!\,m_{24}!\,m_{34}!}\\
&\times(\mathbf{D}_1\cdot\mathbf{D}_2)^{m_{12}}(\mathbf{D}_1\cdot\mathbf{D}_3)^{m_{13}}(\mathbf{D}_1\cdot\mathbf{D}_4)^{m_{14}}(\mathbf{D}_2\cdot\mathbf{D}_3)^{m_{23}}(\mathbf{D}_2\cdot\mathbf{D}_4)^{m_{24}}(\mathbf{D}_3\cdot\mathbf{D}_4)^{m_{34}}\,.\\
&\times\delta_{m_{12}+m_{13}+m_{14}\,,\,l_a}\,\delta_{m_{12}+m_{23}+m_{24}\,,\,L_a}\,\delta_{m_{13}+m_{23}+m_{34}\,,\,l_b}\,\delta_{m_{14}+m_{24}+m_{34}\,,\,L_b}\\
&\times\delta_{m_{12},m_{12}^{(i)}}\,\delta_{m_{13},m_{13}^{(i)}}\,\delta_{m_{14},m_{14}^{(i)}}\,\delta_{m_{23},m_{23}^{(i)}}\,\delta_{m_{24},m_{24}^{(i)}}\,\delta_{m_{34},m_{34}^{(i)}}\,.
\end{aligned} \tag{175}$$

No complicated angular-momentum algebra is needed. The computer algorithm for calculating the coefficients S and $m^{(i)}$ and $i_{\max}$ is simple. A good test of the calculation is to verify that S is independent of M.

It is to be emphasized that the coefficients S depend neither on specific three-body systems nor on the Gaussian range parameters, and therefore they can be stored in a data file and universally used for any three-body calculation. This is an advantage of the ISG basis functions.

Needless to say, the authors examined numerically that the matrix elements calculated with Eq.(174) are exactly the same as those calculated with the expression obtained in Appendix A.1 for the original Gaussian basis functions.

The structure of the final expression of the matrix elements in Eq.(174) is very suitable for vector-processor computation. The 'do loop' to sweep the matrix elements (by changing n_a, N_a, n_b, N_B in a one-dimensional manner for a given set of l_a, L_a, l_b, L_b) should be placed *inside* the 'do loop' for the summation over i. This makes the computation time shorter by a factor of $10 - 20$. This is also an advantage of the ISG basis functions.

Central potential $V(r_c)$ of arbitrary shape

For any arbitrary functional form of $V(r_c)$, it is possible to calculate the three-body matrix element in Eq.(162). Performing the integration over $\mathbf{R}_c$ first and then over $\hat{\mathbf{r}}_c$, we obtain the following type of expression for $\langle\, V(r_c)\,\rangle_{\mathbf{r}_c,\mathbf{R}_c}$:

$$\langle\, V(r_c)\,\rangle_{\mathbf{r}_c,\mathbf{R}_c} = G'_{ab}\, e^P \sum_{m=0}^{L^{(\mathrm{sum})}} \frac{1}{(2m+1)!}\, Q^m\, V_m\ , \tag{176}$$

where

$$P = \sum_{1=i<j}^{4} p_{ij}\, \varepsilon_i\, \varepsilon_j \mathbf{D}_i \cdot \mathbf{D}_j\ , \qquad Q = \sum_{1=i<j}^{4} q_{ij}\, \varepsilon_i\, \varepsilon_j \mathbf{D}_i \cdot \mathbf{D}_j \tag{177}$$

$$V_m = \int_0^\infty r_c^{2\,m}\, e^{-\alpha r_c^2}\, V(r_c)\, r_c^2\, dr\ . \tag{178}$$

Here, though not explicitly given, G'_{ab}, p_{ij} and q_{ij} and α are numbers which depend on the Gaussian range parameters (ν_{n_a}, λ_{N_a}, ν_{n_b}, λ_{N_b}) and the coordinate transformation coefficients (α_{ac}, β_{ac}, γ_{ac}, δ_{ac}, α_{bc}, β_{bc}, In the course of calculations, we have used the expansion of the modified Bessel function $\mathcal{I}_0(z) = \sum_{m=0}^{\infty} \frac{z^{2m}}{(2m+1)!}$, but the upper limit of the summation is $L^{(\mathrm{sum})}$ in Eq.(176) due to the consideration on the powers of ε's. V_m should be calculated by the interpolation with respect to α in the same manner as the integration Eq.(144).

In the same way as before, we expand $e^P Q^m$ with respect to the ε's and pick up the terms which have appropriate powers of the ε's, namely $\varepsilon_1^{l_a}\, \varepsilon_2^{L_a}\, \varepsilon_3^{l_b}\, \varepsilon_4^{L_b}$. The resulting expression is similar to Eqs.(174) and (175). The computer algorithm is still simple.

Other operators

Calculation of the matrix elements of norm-overlap and kinetic-energy operators is simpler than the above cases. The coordinate transformation $(\mathbf{r}_a, \mathbf{R}_a) \to (\mathbf{r}_b, \mathbf{R}_b)$ is recommended.

In the case of a momentum-dependent force such as

$$V_c = \nabla^2_{\mathbf{r}_c}\, V(r_c) + V(r_c)\, \nabla^2_{\mathbf{r}_c}\ , \tag{179}$$

the operation of $\nabla^2_{\mathbf{r}_c}$ on the bra and ket functions is easily performed since they are simple functions of $\mathbf{r}_c$. The structure of the final expression of $\langle\, V_c\,\rangle_{\mathbf{r}_c,\mathbf{R}_c}$ is similar in style to Eq.(176), but the part

associated with the radial integration appears in the form

$$\sum_{m=0}^{L^{(\mathrm{sum})}} \frac{1}{(2m+1)!}\, Q^m\, V_{m+2}. \tag{180}$$

As for the spin-orbit force and the tensor force, with some spin angular-momentum algebra, the final expression is given in a similar style to the above but slightly more complicated. The part associated with the radial integration appears in the form

$$\sum_{m=0}^{L^{(\mathrm{sum})}} \frac{(m+1)!}{m!\,(2(m+1)+1)!}\, Q^m\, V_{m+1} \qquad \text{for spin-orbit force,} \tag{181}$$

$$\sum_{m=0}^{L^{(\mathrm{sum})}} \frac{(m+2)!}{m!\,(2(m+2)+1)!}\, Q^m\, V_{m+2} \qquad \text{for tensor force.} \tag{182}$$

In our test calculation of the three-nucleon bound state, we verified that the method used in this Appendix with realistic NN forces with central, spin-orbit, tensor, l^2, quadratic spin-orbit, momentum-dependent forces gave the same result as does the method of Gaussian basis functions in Appendix A.1.

A.4 Four-body matrix elements using infinitesimally-shifted Gaussian basis functions

Calculation of the matrix elements between the four-body basis functions is quite analogous to the three-body case. Using the four-body Gaussian basis functions in Eq. (69), the matrix elements of a central potential $V(r_c)$ are represented apparently as

$$\begin{aligned}
&\left\langle \left[\left[\phi^{\mathrm{G}}_{n_a l_a}(\mathbf{r}_a)\,\psi^{\mathrm{G}}_{N_a L_a}(\mathbf{R}_a)\right]_{I_a} \chi^{\mathrm{G}}_{\nu_a\lambda_a}(\boldsymbol{\rho}_a)\right]_{JM} \Big| V(r_c) \Big| \left[\left[\phi^{\mathrm{G}}_{n_b l_b}(\mathbf{r}_b)\,\psi^{\mathrm{G}}_{N_b L_b}(\mathbf{R}_b)\right]_{I_b} \chi^{\mathrm{G}}_{\nu_b\lambda_b}(\boldsymbol{\rho}_b)\right]_{JM} \right\rangle \\
&= N_{n_a l_a}\, N_{N_a L_a}\, N_{\nu_a\lambda_a}\, N_{n_b l_b}\, N_{N_b L_b}\, N_{\nu_b\lambda_b} \\
&\times \sum_{M_{I_a}\mu_a} (\lambda_a\mu_a I_a M_{I_a}|JM) \sum_{M_{I_b}\mu_b} (\lambda_b\mu_b I_b M_{I_b}|JM) \sum_{m_a M_a} (l_a m_a L_a M_a|I_a M_{I_a}) \sum_{m_b M_b} (l_b m_b L_b M_b|I_b M_{I_b}) \\
&\times \lim_{\varepsilon_a\to 0} \frac{1}{(\nu_{n_a}\varepsilon_a)^{l_a}} \lim_{\varepsilon_A\to 0} \frac{1}{(\lambda_{N_a}\varepsilon_A)^{L_a}} \lim_{\varepsilon_\alpha\to 0} \frac{1}{(\omega_{\nu_a}\varepsilon_\alpha)^{\lambda_a}} \lim_{\varepsilon_b\to 0} \frac{1}{(\nu_{n_b}\varepsilon_b)^{l_b}} \lim_{\varepsilon_B\to 0} \frac{1}{(\lambda_{N_b}\varepsilon_B)^{L_b}} \lim_{\varepsilon_\beta\to 0} \frac{1}{(\omega_{\nu_b}\varepsilon_\beta)^{\lambda_b}} \\
&\times \sum_{k_a}\sum_{K_a}\sum_{\kappa_a}\sum_{k_b}\sum_{K_b}\sum_{\kappa_b} C_{l_a m_a,k_a}\, C_{L_a M_a,K_a}\, C_{\lambda_a\mu_a,\kappa_a}\, C_{l_b m_b,k_b}\, C_{L_b M_b,K_b}\, C_{\lambda_b\mu_b,\kappa_b}\, \langle\, V(r_c)\,\rangle_{\mathbf{r}_c,\mathbf{R}_c,\boldsymbol{\rho}_c}
\end{aligned} \tag{183}$$

with

$$\begin{aligned}
\langle\, V(r_c)\,\rangle_{\mathbf{r}_c,\mathbf{R}_c,\boldsymbol{\rho}_c} \;\equiv\; &\langle\, e^{-\nu_{n_a}(\mathbf{r}_a-\varepsilon_a \mathbf{D}_{l_a m_a,k_a})^2}\, e^{-\lambda_{N_a}(\mathbf{R}_a-\varepsilon_A \mathbf{D}_{L_a M_a,K_a})^2}\, e^{-\omega_{\nu_a}(\boldsymbol{\rho}_a-\varepsilon_\alpha \mathbf{D}_{\lambda_a\mu_a,\kappa_a})^2} \,| \\
\times\; &V(r_c)\,|\, e^{-\nu_{n_b}(\mathbf{r}_b-\varepsilon_b \mathbf{D}_{l_b m_b,k_b})^2}\, e^{-\lambda_{N_b}(\mathbf{R}_b-\varepsilon_B \mathbf{D}_{L_b M_b,K_b})^2}\, e^{-\omega_{\nu_b}(\boldsymbol{\rho}_b-\varepsilon_\beta \mathbf{D}_{\lambda_b\mu_b,\kappa_b})^2} \,\rangle_{\mathbf{r}_c,\mathbf{R}_c,\boldsymbol{\rho}_c}.
\end{aligned} \tag{184}$$

The coordinate transformation $(\mathbf{r}_a,\mathbf{R}_a,\boldsymbol{\rho}_a),(\mathbf{r}_b,\mathbf{R}_b,\boldsymbol{\rho}_b) \to (\mathbf{r}_c,\mathbf{R}_c,\boldsymbol{\rho}_c)$ of the form

$$\begin{aligned}
\mathbf{r}_a &= \alpha_{ac}\mathbf{r}_c + \beta_{ac}\mathbf{R}_c + \gamma_{ac}\boldsymbol{\rho}_c\,, \qquad \mathbf{R}_a = \alpha'_{ac}\mathbf{r}_c + \beta'_{ac}\mathbf{R}_c + \gamma'_{ac}\boldsymbol{\rho}_c\,, \\
\mathbf{r}_b &= \alpha_{bc}\mathbf{r}_c + \beta_{bc}\mathbf{R}_c + \gamma_{bc}\boldsymbol{\rho}_c\,, \qquad \mathbf{R}_b = \alpha'_{bc}\mathbf{r}_c + \beta'_{bc}\mathbf{R}_c + \gamma'_{bc}\boldsymbol{\rho}_c\,,
\end{aligned} \tag{185}$$

is then done in the arguments of the Gaussians.

For clarity in expression below, the following definition is introduced:

$$\begin{aligned}
&\varepsilon_1 = \varepsilon_a,\quad \varepsilon_2 = \varepsilon_A,\quad \varepsilon_3 = \varepsilon_\alpha,\quad \varepsilon_4 = \varepsilon_b,\quad \varepsilon_5 = \varepsilon_B,\quad \varepsilon_6 = \varepsilon_\beta, \\
&\mathbf{D}_1 = \mathbf{D}^*_{l_a m_a,k_a},\ \mathbf{D}_2 = \mathbf{D}^*_{L_a M_a,K_a},\ \mathbf{D}_3 = \mathbf{D}^*_{\lambda_a\mu_a,\kappa_a},\ \mathbf{D}_4 = \mathbf{D}_{l_b m_b,k_b},\ \mathbf{D}_5 = \mathbf{D}_{L_b M_b,K_b},\ \mathbf{D}_6 = \mathbf{D}^*_{\lambda_b\mu_b,\kappa_b}, \\
&L^{(\mathrm{sum})} = (l_a + L_a + \lambda_a + l_b + L_b + \lambda_b)/2.
\end{aligned} \tag{186}$$

where $(l_a + L_a + \lambda_a + l_b + L_b + \lambda_b)/2$ is an integer because of the parities $(-)^{l_a+L_a+\lambda_a} = (-)^{l_b+L_b+\lambda_b}$.

Gaussian potential

In the case of a Gaussian potential, $V(r_c) = v_0\, e^{-\mu r_c^2}$, following the prescription in the three-body case, we calculate Eq. (184) to get the result in the form

$$
\begin{aligned}
&\left\langle \left[\left[\phi^{\mathrm{G}}_{n_a l_a}(\mathbf{r}_a)\, \psi^{\mathrm{G}}_{N_a L_a}(\mathbf{R}_a) \right]_{I_a} \chi^{\mathrm{G}}_{\nu_a \lambda_a}(\boldsymbol{\rho}_a) \right]_{JM} \Big| \, V(r_c) \, \Big| \left[\left[\phi^{\mathrm{G}}_{n_b l_b}(\mathbf{r}_b)\, \psi^{\mathrm{G}}_{N_b L_b}(\mathbf{R}_b) \right]_{I_b} \chi^{\mathrm{G}}_{\nu_b \lambda_b}(\boldsymbol{\rho}_b) \right]_{JM} \right\rangle \\
&= N_{n_a l_a}\, N_{N_a L_a}\, N_{\nu_a \lambda_a}\, N_{n_b l_b}\, N_{N_b L_b}\, N_{\nu_b \lambda_b}\, G_{ab} / (\nu_{n_a}^{l_a}\, \lambda_{N_a}^{L_a}\, \omega_{\nu_a}^{\lambda_a}\, \nu_{n_b}^{l_b}\, \lambda_{N_b}^{L_b}\, \omega_{\nu_b}^{\lambda_b}) \\
&\times \sum_{M_{I_a} \mu_a} (\lambda_a \mu_a I_a M_{I_a} | JM) \sum_{M_{I_b} \mu_b} (\lambda_b \mu_b I_b M_{I_b} | JM) \sum_{m_a M_a} (l_a m_a L_a M_a | I_a M_{I_a}) \sum_{m_b M_b} (l_b m_b L_b M_b | I_b M_{I_b}) \\
&\times \sum_{k_a} \sum_{K_a} \sum_{\kappa_a} \sum_{k_b} \sum_{K_b} \sum_{\kappa_b} C_{l_a m_a, k_a}\, C_{L_a M_a, K_a}\, C_{\lambda_a \mu_a, \kappa_a}\, C_{l_b m_b, k_b}\, C_{L_b M_b, K_b}\, C_{\lambda_b \mu_b, \kappa_b} \qquad (187) \\
&\times \left[\prod_{1=i<j}^{6} \sum_{m_{ij}=0}^{L^{(\mathrm{sum})}} \frac{1}{m_{ij}!} (g_{ij}\, \mathbf{D}_i \cdot \mathbf{D}_j)^{m_{ij}} \right] \delta_{m_{12}+m_{13}+m_{14}+m_{15}+m_{16},\, l_a}\, \delta_{m_{12}+m_{23}+m_{24}+m_{25}+m_{26},\, L_a} \\
&\times \delta_{m_{13}+m_{23}+m_{34}+m_{35}+m_{36},\, \lambda_a}\, \delta_{m_{14}+m_{24}+m_{34}+m_{45}+m_{46},\, l_b}\, \delta_{m_{15}+m_{25}+m_{35}+m_{45}+m_{56},\, L_b}\, \delta_{m_{16}+m_{26}+m_{36}+m_{46}+m_{56},\, \lambda_b} .
\end{aligned}
$$

We then sum up those coefficients that are associated with the same powers of the g_{ij}'s, namely $\prod_{1=i<j}^{6} g_{ij}^{m_{ij}}$.
The result can be summarized in the following form which is much more useful for a rapid computation:

$$
\begin{aligned}
&\left\langle \left[\left[\phi^{\mathrm{G}}_{n_a l_a}(\mathbf{r}_a)\, \psi^{\mathrm{G}}_{N_a L_a}(\mathbf{R}_a) \right]_{I_a} \chi^{\mathrm{G}}_{\nu_a \lambda_a}(\boldsymbol{\rho}_a) \right]_{JM} \Big| \, V(r_c) \, \Big| \left[\left[\phi^{\mathrm{G}}_{n_b l_b}(\mathbf{r}_b)\, \psi^{\mathrm{G}}_{N_b L_b}(\mathbf{R}_b) \right]_{I_b} \chi^{\mathrm{G}}_{\nu_b \lambda_b}(\boldsymbol{\rho}_b) \right]_{JM} \right\rangle \\
&= N_{n_a l_a}\, N_{N_a L_a}\, N_{\nu_a \lambda_a}\, N_{n_b l_b}\, N_{N_b L_b}\, N_{\nu_b \lambda_b}\, G_{ab} / (\nu_{n_a}^{l_a}\, \lambda_{N_a}^{L_a}\, \omega_{\nu_a}^{\lambda_a}\, \nu_{n_b}^{l_b}\, \lambda_{N_b}^{L_b}\, \omega_{\nu_b}^{\lambda_b}) \\
&\times \sum_{i=1}^{i_{\max}} S^{J}_{l_a, L_a, \lambda_a, l_b, L_b, \lambda_b}(m_{12}^{(i)}, m_{13}^{(i)}, \ldots\ldots, m_{56}^{(i)})\, g_{12}^{m_{12}^{(i)}}\, g_{13}^{m_{13}^{(i)}} \cdots\cdots g_{56}^{m_{56}^{(i)}} \qquad (188)
\end{aligned}
$$

with

$$
\begin{aligned}
&S^{J}_{l_a, L_a, \lambda_a, l_b, L_b, \lambda_b}(m_{12}^{(i)}, m_{12}^{(i)}, \ldots\ldots, m_{56}^{(i)}) \\
&= \sum_{M_{I_a} \mu_a} (\lambda_a \mu_a I_a M_{I_a} | JM) \sum_{M_{I_b} \mu_b} (\lambda_b \mu_b I_b M_{I_b} | JM) \sum_{m_a M_a} (l_a m_a L_a M_a | I_a M_{I_a}) \sum_{m_b M_b} (l_b m_b L_b M_b | I_b M_{I_b}) \\
&\times \sum_{k_a} \sum_{K_a} \sum_{\kappa_a} \sum_{k_b} \sum_{K_b} \sum_{\kappa_b} C_{l_a m_a, k_a}\, C_{L_a M_a, K_a}\, C_{\lambda_a \mu_a, \kappa_a}\, C_{l_b m_b, k_b}\, C_{L_b M_b, K_b}\, C_{\lambda_b \mu_b, \kappa_b} \\
&\times \sum_{m_{12}} \sum_{m_{13}} \cdots\cdots \sum_{m_{56}} \frac{1}{m_{12}!\, m_{13}!\, \cdots\cdots\, m_{56}!} (\mathbf{D}_1 \cdot \mathbf{D}_2)^{m_{12}} (\mathbf{D}_1 \cdot \mathbf{D}_3)^{m_{13}} \cdots\cdots (\mathbf{D}_5 \cdot \mathbf{D}_6)^{m_{56}} \\
&\times \delta_{m_{12}+m_{13}+m_{14}+m_{15}+m_{16},\, l_a}\, \delta_{m_{12}+m_{23}+m_{24}+m_{25}+m_{26},\, L_a}\, \delta_{m_{13}+m_{23}+m_{34}+m_{35}+m_{36},\, \lambda_a} \\
&\times \delta_{m_{14}+m_{24}+m_{34}+m_{45}+m_{46},\, l_b}\, \delta_{m_{15}+m_{25}+m_{35}+m_{45}+m_{56},\, L_b}\, \delta_{m_{16}+m_{26}+m_{36}+m_{46}+m_{56},\, \lambda_b} \\
&\times \delta_{m_{12}, m_{12}^{(i)}}\, \delta_{m_{13}, m_{13}^{(i)}} \cdots\cdots \delta_{m_{56}, m_{56}^{(i)}} \qquad (189)
\end{aligned}
$$

This expression is quite analogous to Eq. (175) in the three-body case. Algorithm for the calculation of four body systems is only a slight extension of that for the three-body case. This is an advantage of the ISGL basis functions.

It is to be emphasized that the coefficients S depend neither on specific four-body systems nor on the Gaussian range parameters, and therefore can be stored in a data file and be used universally for any four-body calculation. This is an advantage of the ISGL basis functions. We can make the same comment as in Appendix A.3 on the advantageous use of vector processors.

Central potential $V(r_c)$ of arbitrary shape

As in the calculation of the three-body matrix elements, it is easy to calculate the four-body matrix elements of the central force $V(r_c)$ of any functional form. Performing the integration over $\boldsymbol{\rho}_c$ and $\mathbf{R}_c$

first and then over $\hat{\mathbf{r}}_c$, we obtain the following type of expression for $\langle V(r_c) \rangle_{\mathbf{r}_c, \mathbf{R}_c, \boldsymbol{\rho}_c}$:

$$\langle V(r_c) \rangle_{\mathbf{r}_c, \mathbf{R}_c} = G'_{ab} e^P \sum_{m=0}^{L(\mathrm{sum})} \frac{1}{(2m+1)!} Q^m V_m \tag{190}$$

with

$$P = \sum_{1=i<j}^{6} p_{ij} \varepsilon_i \varepsilon_j \mathbf{D}_i \cdot \mathbf{D}_j , \qquad Q = \sum_{1=i<j}^{6} q_{ij} \varepsilon_i \varepsilon_j \mathbf{D}_i \cdot \mathbf{D}_j \tag{191}$$

$$V_m = \int_0^\infty r_c^{2m} e^{-\alpha r_c^2} V(r_c) r_c^2 \, dr . \tag{192}$$

Here, though not explicitly given, G'_{ab}, p_{ij} and q_{ij} and α are numbers which depend on the Gaussian sizes (ν_{n_a}, λ_{N_a}, ω_{ν_a}, ν_{n_b}, λ_{N_b}, ω_{ν_a}) and the coordinate transformation coefficients (α_{ac}, β_{ac}, γ_{ac}, α'_{ac}, β'_{ac}, γ'_{ac}, α_{bc}, β_{bc}, γ_{bc}, α'_{bc}, β'_{bc}, γ'_{bc},). V_m should be calculated by the interpolation with respect to α in the same manner as the integration Eq.(144).

In the same manner as before, we expand $e^P Q^m$ in powers of the ε's and pick up the terms which have appropriate powers of the ε's, namely $\varepsilon_1^{l_a} \varepsilon_2^{L_a} \varepsilon_3^{\lambda_a} \varepsilon_4^{l_b} \varepsilon_5^{L_b} \varepsilon_6^{\lambda_b}$. The resulting expression is similar to Eqs.(188) and (189). The computer algorithm is quite similar to that in the three-body case.

As for other interactions such as momentum-dependent forces and non-central forces, the same comments as Eqs.(180) – (182) are applicable.

References

[1] Particle Data Group, D. E. Groom *et al.*, Eur. Phys. J. C **15** (2000) 1.

[2] H. A. Torii *et al.*, Phys. Rev. A **59** (1999) 223.

[3] Y. Kino, M. Kamimura and H. Kudo, Hyp. Interact. **119** (1999) 201.

[4] M. Kamimura, Phys. Rev. A **38** (1988) 621.

[5] M. Kamimura, Muon Catalyzed Fusion **3** (1988) 335.

[6] H. Kameyama, M. Kamimura and Y. Fukushima, Phys. Rev. C **40** (1989) 974.

[7] M. Kamimura and H. Kameyama, Nucl. Phys. A **508** (1990) 17c.

[8] Particle Data Group, K. Hagiwara *et al.*, Phys. Rev. D **66** (2002) 010001.

[9] M. Hori *et al.*, Phys. Rev. Lett. **87** (2001) 093401.

[10] Y. Kino, N.Yamanaka, M. Kamimura, P. Froelich and H. Kudo, Hyp. Interact. **139** (2001) 179.

[11] E. Hiyama, M. Kamimura, T. Motoba, T. Yamada and Y. Yamamoto, Phys. Rev. C **53** (1996) 2075.

[12] E. Hiyama, M. Kamimura, T. Motoba, T. Yamada and Y. Yamamoto, Prog. Theor. Phys. **97** (1997) 881.

[13] E. Hiyama, M. Kamimura, K. Miyazaki and T. Motoba, Phys. Rev. C **59** (1999) 2351.

[14] E. Hiyama, M. Kamimura, T. Motoba, T. Yamada and Y. Yamamoto, Phys. Rev. Lett. **85** (2000) 270.

[15] E. Hiyama, M. Kamimura, T. Motoba, T. Yamada and Y. Yamamoto, Phys. Rev. C **65** (2001) 011301.

[16] E. Hiyama, M. Kamimura, T. Motoba, T. Yamada and Y. Yamamoto, Phys. Rev. C **66** (2002) 024007.

[17] M. M. Nagels, T. A. Rijken and J. J. de Swart, Phys. Rev. D **12** (1975) 744; **15** (1977) 2547; **20** (1979) 1633.

[18] T. A. Rijken, V. G. J. Stoks, and Y. Yamamoto, Phys. Rev. C **59** (1999) 21.

[19] Y. Fujiwara, C. Nakamoto and Y. Suzuki, Phys. Rev. Lett. **76** (1996) 2242.

[20] S. Ajimura *et al.*, Phys. Rev. Lett. **86** (2001) 4225.

[21] H. Akikawa *et al.*, Phys. Rev. Lett. **88** (2002) 82501.

[22] B. F. Gibson, A. Goldberg and M. S. Weiss, Phys. Rev. C **6** (1972) 741.

[23] B. F. Gibson and D. R. Lehman, Phys. Rev. C **37** (1988) 679.

[24] Y. Akaishi, T. Harada, S. Shinmura, and Khin Swe Myint, Phys. Rev. Lett. **84** (2000) 3539.

[25] K. Nagamine and M. Kamimura, Adv. in Nucl. Phys. **24** (1998) 151.

[26] P. Froelich, Adv. Phys. **41** (1992) 405.

[27] H.W. Breunlich, Nucl. Phys. A **508** (1990) 1c.

[28] W. H. Breunlich, P. Kammel, J. S. Cohen and M. Leon, Ann. Rev. Nucl. Part. Sci. **39** (1989) 311.

[29] S. Funada, H. Kameyama, and Y. Sakuragi, Nucl. Phys. A **575** (1994) 93.

[30] E. Hiyama and M. Kamimura, Nucl. Physics A **588** (1995) 35c.

[31] Y. Kino, M. Kamimura and H. Kudo, Nucl. Phys. A **31** (1998) 649.

[32] Y. Kino, M. Kamimura and H. Kudo, Few-Body Syst. Suppl. **12** (2000) 40.

[33] V. I. Korobov, Phys. Rev. A **54** (1996) R1749.

[34] V. I. Korobov and D. D. Bakarov, Phys. Rev. Lett. **79** (1997) 3379.

[35] V. I. Korobov *et al.*, Phys. Rev. A **59** R919 (1999).

[36] V. I. Korobov, Nucl. Phys. A **689** (2001) 75c.

[37] E. Hiyama, RCNP Physics Report (Research Center for Nuclear Physics, Osaka Univ.), RCNP-P-132 (1994) 35.

[38] E. Hiyama, Proceedings of International Workshop on the 4-Body Problems, Uppsala, 1995 (Uppsala Univ., 1996) 28.

[39] H. Kamada, A. Nogga, W. Glockle, E. Hiyama, M. Kamimura, K. Varga, Y. Suzuki, M. Viviani, A. Kievsky, S. Rosati, J. Carlson, S. C. Pieper, R. B. Wiringa, P. Navratil, B. R. Barrett, N. Barnea, W. Leidemann and G. Orlandini, Phys. Rev. C **64** (2001) 044001.

[40] E. Hiyama, B. Gibson and M. Kamimura, a contribution to the 17th International IUPAP Conference on Few-Body Problems in Physics, Durham, June 5-10, 2003; and a preprint to be submitted.

[41] Y. Kino and M. Kamimura, Hyp. Interact. **82** (1993) 45.

[42] Y. Kino and M. Kamimura, Hyp. Interact. **82** (1993) 195.

[43] M. Kamimura, M. Yahiro, Y. Iseri, Y. Sakuragi, H. Kameyama and M. Kawai, Prog. Theor. Phys. Suppl. **89** (1986) 1.

[44] N. Austern, Y. Iseri, M. Kamimura, M. Kawai, G. Rawitscher and M. Yahiro, Phys. Rep. **154** (1987) 125.

[45] M. Yahiro, N. Nakano, Y. Iseri and M. Kamimura Prog. Theor. Phys. **67** (1982) 1464.

[46] M. Yahiro, Y. Iseri, M. Kamimura and M. Nakano, Phys. Lett. **141B** (1984) 19.

[47] Y. Sakuragi and M. Kamimura, Phys. Lett. **149B** (1984) 307.

[48] Y. Sakuragi, Phys. Rev. C **35** (1987) 2161.

[49] Y. Sakuragi, M. Yahiro, M. Kamimura and M. Tanifuji, Nucl. Phys. A **480** (1988) 361.

[50] Y. Iseri, H. Kameyama, M. Kamimura, M. Yahiro and M. Tanifuji, Nucl. Phys. A **490** (1988) 383.

[51] Y. Hirabayashi and Y. Sakuragi, Phys. Rev. Lett. **69** (1992) 1892.

[52] R. A. D. Piyadasa, M. Kawai, M. Kamimura and M. Yahiro, Phys. Rev. C **60** (1999) 044611.

[53] J. A. Tostevin, D. Bazin, B. A. Brown, T. Glasmacher, P. G. Hansen, V. Maddalena, A. Navin and B. M. Sherrill, Phys. Rev. C **66** (2002) 024607; A. M. Moro, R. Crespo, F. Nunes and I. J. Thompson, Phys. Rev. C **66** (2002) 024612, and references therein.

[54] K. Ogata, M. Yahiro, Y. Iseri and M. Kamimura, Phys. Rev. C **67** (2003) R011602.

[55] R. A. Aziz, V. P. S. Nain, J. S. Carley, W. L. Taylor and G. T. McConville, J. Chem. Phys. **70** (1979) 4330.

[56] Th. Cornelius and W. Gloeckle, J. Chem. Phys. **85** (1986) 3906.

[57] J. L. Friar *et al.*, Phys. Rev. C **42** (1990) 1838.

[58] T. Matsumoto, M. Yahiro, E. Hiyama and M. Kamimura, private communications (2002).

[59] M. Kamimura, Prog. Theor. Phys. Suppl. **62** (1977) 236.

[60] P. Froelich, S. Jonsell, A. Saenz, B. Zygelman and A. Dalgarno, Phys. Rev. Lett. **84** (2000) 4577.

[61] M. Amoretti *et al.*, Nature **419** (2002) 456.

[62] G. Gabrielse *et al.*, Phys. Rev. Lett. **89** (2002) 213401.

[63] R.B. Wiringa, R. A. Smith and T. A. Ainsworth, Phys. Rev. C **29** (1984) 1207.

[64] S. A. Coon, M. D. Scardon, P. C. McName, B. R. Barrett, D. W. E. Blatt and B. H. J. McKeller, Nucl. Phys. A **318** (1979) 242.

[65] C. R. Chen, G. L. Payne, J. L. Frier and B. F. Gibson, Phys. Rev. C **31** (1985) 2266.

[66] S. Ishikawa and T. Sasakawa, Few-Body Syst. **1** (1986) 143.

[67] T. Sasakawa, in proceedings of the Workshop on Electron Nucleus Scattering, Elba International physics Center, Italy, 1988; Y. Wu, S. Ishikawa and T. Sasakawa, private communications (1989).

[68] O. Yakubovsky, Yad. Fiz. **5** (1967) 1312 [Sov. J. Nucl. Phys. **5** (1967) 937].

[69] W. Glöckle and H. Kamada, Phys. Rev. Lett. **71** (1993) 971; H. Kamada and W. Glöckle, Nucl. Phys. A **548** (1992) 205.

[70] A. Nogga, H. Kamada and W. Glöckle, Phys. Rev. Lett. **85** (2000) 944.

[71] W. Glöckle, *The Quantum Mechanical Few-Body Problem* (Springer-Verlag, Berlin, Heidelberg, 1983).

[72] Y. Suzuki and K. Varga, *Stochastic Variational Approach to Quantum Mechanical Few-Body Problems* (Springer-Verlag, Berlin, 1998).

[73] K. Varga and Y. Suzuki, Phys. Rev. C **52** (1995) 2885.

[74] K. Varga, Y. Ohbayashi and Y. Suzuki, Phys. Lett. B **396** (1997) 1.

[75] J. Usukura, K. Varga and Y. Suzuki, Phys. Rev. A **58** (1998) 1918; J. Usukura, K. Varga and Y. Suzuki, Phys. Rev. B **59** (1999) 5652.

[76] J. Avery, *Hyperspherical Harmonics* (Kluwer Academic, Dordrecht, 1989).

[77] M. Fabre de la Ripelle, Ann. Phys. (N. Y.) **147** (1983) 281.

[78] M. Viviani, A Kievsky, and S. Rosati, Few-Body Syst. **18** (1995) 25.

[79] A. Kievsky, L. E. Marcucci, S. Rosati and M. Viviani, Few-Body Syst. **22** (1997) 1.

[80] M. Viviani, Few-Body Syst. **25** (1988) 177.

[81] B. S. Pudliner, V. R. Pandharipande, J. Carlson, Steven C. Pieper and R. B. Wiringa, Phys. Rev. C **56** (1997) 1720.

[82] J. Carlson, Phys. Rev. C **36** (1987) 2026.

[83] J. Carlson, Phys. Rev. C **38** (1988) 1879.

[84] R. B. Wiringa, Steven C. Pieper, J. Carlson and V. R. Pandharipande, Phys. Rev. C **62** (2000) 014001.

[85] P. Navrátil and B. R. Barrett, Phys. Rev. C **59** (1999) 1906; P. Navrátil, G. P. Kamuntavičius and B. R. Barret, *ibid.* **61** (2000) 044001; P. Navrátil, J. P. Vary and B. R. Barrett, Phys. Rev. Lett. **84** (2000) 5728; Phys. Rev. C **62** (2000) 054311.

[86] K. Suzuki and S. Y. Lee, Prog. Theor. Phys. **64** (1980) 2091.

[87] P. Navrátil, H. B. Geyer and T. T. S. Kuo, Phys. Lett. B **315** (1993) 1.

[88] N. Barnea, W. Leidemann and G. Orlandini, Phys. Rev. C **61** (2000) 054001.

[89] R. B. Wiringa, V. G. J. Stoks and R. Schiavilla, Phys. Rev. C **51** (1995) 38.

[90] S. I. Vinitsky *et al.*, Sov. Phys. JETP **52** (1980) 353.

[91] A. D. Gocheva *et al.*, Phys. Lett. B **153** (1985) 349.

[92] S. I. Vinitsky, V. I. Korobov and I. V. Puzynin, Sov. Phys. JETP **64** (1986) 417.

[93] V. I. Korobov, S. I. Vinitsky and I. V. Puzynin, Phys. Lett. **B196** (1987) 272.

[94] K. Szalewitz, W. Koros, H. J. Monkhorst and A. Scrinzi, Phys. Rev. A **36** (1987) 5494.

[95] S. A. Alexander, H. J. Monkhorst, Phys. Rev. A **38** (1988) 26.

[96] K. Ikeda *et al.*, Prog. Theor. Phys. Suppl. **68** (1980) 1.

[97] Y. Kino, M. R. Harston, I. Shimamura, E. A. G. Armour and M. Kamimura, Phys. Rev. A **52** (1995) 870.

[98] G. Aissing, H.J. Monkhorst and Yu. V. Petrov, Phys. Rev. A **42** (1990) 6894.

[99] Y. Hamahata, E. Hiyama, and M. Kamimura, Hyp. Interact. **138** (2001) 187.

[100] M. Kamimura, AIP Conf. Proc. **181** (1989) 330.

[101] Particle Data Group, C. Caso *et al.*, Eur. Phys. J. C **3** (1998) 1.

[102] G. Gabrielse *et al.*, Phys. Rev. Lett. **89** (1999) 3198.

[103] M. Iwasaki *et al.*, Phys. Rev. Lett. **67** (1991) 1246.

[104] T. Yamazaki *et al.*, Nature, **361** (1993) 238.

[105] Y. K. Ho, Phys. Rep. **99** (1983) 1.

[106] Y. Kino, H. Kudo and M. Kamimura, Mod. Phys. Lett. A **18** (2003) 388.

[107] T. Yamazaki *et al.*, Phys. Rev. A **55** (1997) R3295.

[108] O. Morimatsu, S. Ohta, K. Shimizu and K. Yazaki, Nucl. Phys. A **420** (1984) 573.

[109] M. May *et al.*, Phys. Rev. Lett. **51** (1983) 2085.

[110] M. May *et al.*, Phys. Rev. Lett. **78** (1997) 4343.

[111] E. H. Auerbach *et al.*, Ann. Phys. (N.Y.) **148** (1983) 381.

[112] S. Saito, Prog. Theor. Phys. **41** (1969) 705.

[113] A. Hasegawa and S. Nagata, Prog. Theor. Phys. **45** (1971) 1786.

[114] R. H. Dalitz and B. W. Downs, Phys. Rev. **111** (1958) 967.

[115] J. Carlson, in LAMPF Workshop on (π, K) Physics, edited by B. F. Gibson, W. R. Gibbs and M. B. Johnson, AIP Conf. Proc. **224** (1991) 198.

[116] S. Shinmura (private communications).

[117] A. Nogga, H. Kamada and W. Glöckle, Phys. Rev. Lett. **88** (2002) 172501.

[118] T. Motoba, H. Bandō and K. Ikeda, Prog. Theor. Phys. **70** (1983) 189; T. Motoba, H. Bandō, K. Ikeda and T. Yamada, Prog. Theor. Phys. Suppl. **81** (1985) 42.

[119] K. Tanida *et al.*, Phys. Rev. Lett. **86** (2001) 1982.

[120] E. Hiyama, M. Kamimura, T. Motoba, T. Yamada and Y. Yamamoto, Nucl. Phys. A **684** (2001) 227c.

[121] H. Takahashi *et al.*, Phys. Rev. Lett. **87** (2002) 212502.

[122] K. Ahn *et al.*, In Hadrons and Nuclei, edited by II-Tong Chen *et al.*, AIP Conf. Proc. **594** (2001) 180.

[123] A. Ichikawa, Ph.D. thesis, Kyoto University, 2001.

[124] K. Ishida, S. Sakamoto, Y. Watanabe, T. Matsuzaki and K. Nagamine, Hyp. Interact. **82** (1993) 111.

[125] B. Gartner *et al.*, Phys. Rev. A **62** (2000) 012501.

[126] Y. Kino, private communications (calculated values are cited in Ref.[130]).

[127] J. S. Cohen and M. C. Struensee, Phys. A **43** (1991) 3460.

[128] C. Chiccoli, V. I. Korobov, V. S. Melezhik, P. Pasini, L. I. Ponomarev and J. Wozniak, Muon Catalized Fusion **7** (1992) 87.

[129] O. I. Tolstikhin and C. Namba, Phys. Rev. A **60** (1999) 5111.

[130] A. A. Kvitsinsky, C. Y. Hu and J. S. Cohen, Phys. Rev. A **53** (1996) 255.

[131] T. Matsuzaki *et al.*, Muon Catalyzed Fusion **2** (1988) 217.

[132] V. I. Korobov, Hyp. Interact. **101/102** (1996) 329.

[133] S. Hara and T. Ishihara, Phys. Rev. A **39** (1989) 3633.

[134] T. Matsumoto, T. Kamimzato, K. Ogata, Y. Iseri, E. Hiyama, M. Kamimura and M. Yahiro (2003) submitted to Phys. Rev. C.

[135] G. Hauser, R. Löhken and G. Nowicki, Nucl. Phys. A **182** (1972) 1.

[136] N. Matsuoka, H. Sakai, T. Saito, K. Hosono, M. Kondo and H. Ito, K. Hatanaka, T. Ichihara, A. Okihana, K. Imai, K. Nisimura, Nucl. Phys. A **455** (1986) 413.

[137] T. Matsumoto, E. Hiyama, M. Kamimura, K. Ogata, M. Yahiro and Y. Iseri, Meeting Abstract of the Physical Society of Japan, Vol. 58, Issue 1, part 1 (2003) 40.